Near Field Sensing and Antenna Design for Wireless Body Area Network

A thesis submitted to the School of Electrical and Electronic Engineering for the degree of Doctor of Philosophy

By Waleed Amer

Newcastle University

Newcastle upon Tyne, UK

March 2016

To my ...

... supervisors, for their patience;

... friends, for their support;

...and family, for their prayers.

Certificate of Originality

I declare that this thesis is my own work and it has not been previously submitted by me or by anyone else for a degree or diploma at any educational institute, school or university. To the best of my knowledge, this thesis does not contain any previously published work, except where the use of another person's work has been cited and included in the list of references.

……..

……..

Abstract

Wireless body area network (WBAN) has emerged in recent years as a special class of wireless sensor network; hence, WBAN inherits the wireless sensor network challenges of interference by passive objects in indoor environments. However, attaching wireless nodes to a person's body imposes a unique challenge, presented by continuous changes in the working environment, due to the normal activities of the monitored personnel. Basic activities, like sitting on a metallic chair or standing near a metallic door, drastically change the antenna behaviour when the metallic object is within the antenna near field. Although antenna coupling with the human body has been investigated by many recent studies, the coupling of the WBAN node antenna with other objects within the surrounding environment has not been thoroughly studied.

To address the problems above, the thesis investigates the state-of-the art of WBAN, eximanes the influence of metallic object near an antenna through experimental studies and proposes antenna design and their applications for near field environments. This thesis philosophy for the previously mentioned challenge is to examine and improve the WBAN interaction with its surrounding by enabling the WBAN node to detect nearby objects based solely on change in antenna measurements. The thesis studies the interference caused by passive objects on WBAN node antenna and extracts relevant features to sense the object presence within the near field, and proposes new design of WBAN antenna suitable for this purpose.

The major contributions of this study can be summarised as follows. First, it observes and defines the changes in the return loss of a narrow band antenna when a metallic object is introduced in its near field. Two methods were proposed to detect the object, based on the refelction coefficient and transmission coefficient of an antenna in free space. Then, the thesis introduces a new antenna design that conforms to the WBAN requirements of size, while achieving very low sensitivity to human body. This was achieved through combining two opposite Vivaldi shapes on one PCB and using a metallic sheet to act as a reflector, which minimised the antenna coupling with the human body and reduced the radiation pattern towards the body. Finally, the proposed antennas were tested on several human body parts with nearby metallic objects, to compare the change in antenna s-parameters due to presence of the human body and presence of the metallic object. Based on the measurements, basic statistical indicators and Principal Component Analysis were proposed to detect object presense and estimate its distance. In conclusion, the thesis successfully shows WBAN antenna's ability to detect nearby metallic objects through a set of proposed indicators and novel antenna design. The thesis is wrapped up by the suggestion to investigate time domain features and modulated signal for future work in WBAN near field sensing.

Contents

List of Figures

List of Tables

Nomenclature

BER	Bit Error Rate
CSMA/CA	Carrier Sense Multiple Access with Collision Avoidance
DSSS	Direct-Sequence Spread Spectrum
ECG	Electrocardiogram
HBC	Human Body Communications
IR-UWB	Impulse Response Ultra-Wide Band
ISM	Industrial, Scientific and Medical Radio Band
LOS	Line Of Sight
LQI	Link Quality Indicator
MAC	Medium Access Control
NLOS	Non-Line of Sight
OFDM	Orthogonal Frequency-Division Multiplexing
P2P	Pear to Peak
PCA	Principal Components Analysis
PEC	Perfect Electric Conductor
PHY	Physical layer
RF	Radio Frequency
RFID	Radio Frequency Identifier
RL	Return Loss
RMS	Root Mean Square
RSSI	Received Signal Strength Indicator
RTI	Radio Tomographic Imaging
SHM	Structure Health Monitoring
SNR	Signal to Noise Ratio
UWB	Ultra-Wide Band
VNA	Vector Network Analyser
WBAN	Wireless Body Area Network
WLAN	Wireless Local Area Network
WSN	Wireless Sensor Network

Chapter 1 INTRODUCTION

1.1 Chapter Outline

A significant step in the development of a Wireless Body Area Network (WBAN) is the implementation of the physical layer of the network, which requires a thorough characterisation of the electromagnetic wave propagation and antenna behaviour near the human body [1-4]. In this chapter, we explain the challenges that are facing current technology in this area and the thesis plan to provide a solution. The next section presents the challenges and motivation behind this work. Section 1.3 states the thesis aim and objectives, while Section 1.4 lists this work's contribution to knowledge. The publications that arose from this research are listed in Section 1.5. Finally, the overall outline of the thesis is presented in Section 1.6.

1.2 Challenges and Motivation: Near-Field Interference by Passive Objects in WBAN Application

In recent years, many researchers presents extensive studies regarding the antenna design for wearable application [5-8], antenna coupling with the human body [9-12] and the WBAN channel modelling for both on-body [13-15] and off-body communication [16, 17]. Like many types of wireless networks, the WBAN wireless channel suffers from interference by active and passive elements. Active interference is caused by other RF sources in the environment, such as microwave cooking, mobile phone networks or adjacent WBAN users [18-22]. Passive interference is caused by passive objects in the environment (ones that do not transmit an RF signal), e.g., furniture, walls, doors, etc. [23, 24]. Based on the object location from the LOS, the transmitted signal suffers from multipath distortion, due to a reflection and/or shadowing. The effects of passive objects on the signal propagation are covered by the channel modelling process, where these objects are usually considered to be placed within the far field of the wireless node antenna.

However, attaching wireless nodes to a human body imposes another challenge that is unique for the WBAN application, compared to other wireless networks. This challenge is presented by a continuous change in the work environment, due to the normal activities of the monitored personnel [25, 26]. As seen in Figure 1, basic activities, like sitting on a chair or standing near a door made with a metallic material, bring the antenna into direct contact with an electric conductor surface and drastically change the antenna behaviour, especially when the metallic object is within the antenna near field. The coupling between the antenna and an object is frequency dependent and directly related to the distance

between them. Unlike the objects in the far field, passive objects within the radius of a few wavelengths of the wireless node engage in near-field coupling with the node antenna, which severely affects the antenna radiation properties and, hence, the transmitted/received wireless signal. The existence of such passive objects within a nearby WBAN node can be frequent and last for a relatively long period of time in such a manner that it disturbs the basic mechanism of the network, such as the routing. More significantly, it alters the power level of the received signal, which is vital in some applications, such as localisation [27] and spectrum sensing [28], which depend on power-based measurements to estimate distance and channel availability, respectively. It is worth mentioning that, metallic proximity with a low profile antenna has been investigated in many other literatures regarding Radio Frequency Identifier (RFID) tags and near-field communications [29-31], however, the human body was not considered.

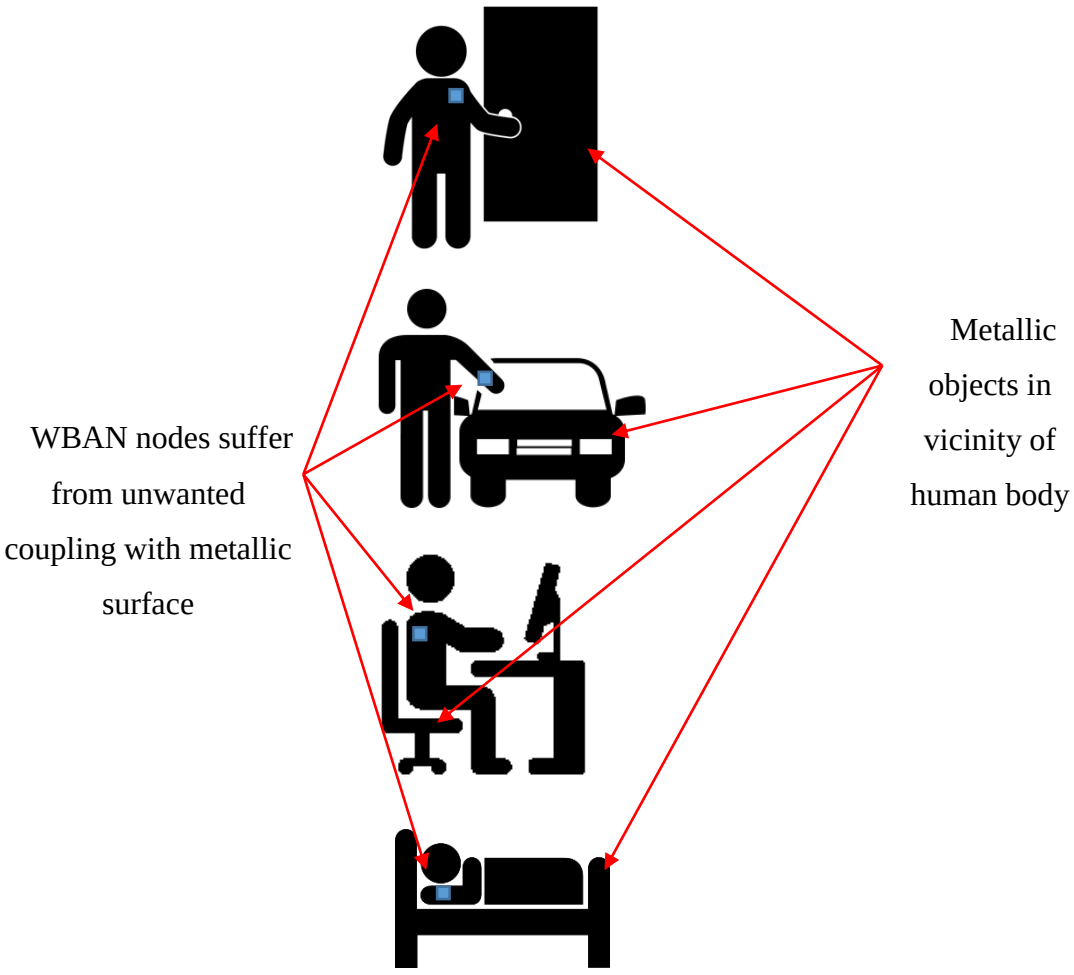

Figure 1: Illustration of interaction scenarios between the WBAN nodes and metallic object in the network environment

To overcome this challenge, antenna diversity [17, 32, 33], or multi-sensor fusion [3] can be employed. In [34], a steerable antenna was proposed for reliable transmissions in Wireless Sensor Network (WSN) but it is not practical for wearable technology. Antenna diversity can be applied to WBAN through a different allocation of the nodes around the human body; however, applying antenna diversity for a single node is not practical, due to size restrictions. Similarly, multi-sensor fusion require the addition of other types of sensors to the node, such as proximity sensors or visual sensors, which increased its cost. Also, when using a proximity sensor, the sensor itself disturb the node's antenna radiation if it was fixed too close to the antenna, and it doesn't sense the antenna problem if it is fixed too far. Both solutions complicate the node structure and fail to tackle the root of the problem.

A better solution is to make the node more 'context-aware' through comprehensive analysing of the antenna measurements. Despite the importance of context-awareness in WBAN applications, there are limited solutions available, particularly at the Medium Access Control (MAC) layer [35-37]. Measurements, such as the Received Signal Strength Indicator (RSSI), Link Quality Indicator (LQI) or Signal to Noise Ratio (SNR), are used in several applications [28, 38, 39] to assess the channel quality or the surrounding environment. However, these measurements are highly affected by near field, to the extent that they will give an incorrect assessment. The next sections explain the thesis aim and suggestions for facing challenges in this field of research.

1.3 Aim and Objectives

The aim of this thesis is to improve the interaction between WBAN and its surrounding by enabling the WBAN node to sense the presence of nearby passive object and estimate its distance to WBAN antenna based solely on change in antenna measurements. The main objectives of this thesis can be outlined thusly:

1. Undertake a thorough review of several related systems and applications, including near-field sensing, localisation of passive objects and context-aware antennas, as well as a review of the art of WBAN antenna design.
2. Understand the near field influence of passive objects on antenna measurements through experimental studies using a low profile dipole antenna widely used for indoor wireless applications and a metallic plate to be used as a passive object. Then, build a simulation model of a similar setup in CST Microwave Studio to validate the experimental results.

3. Analyse the antenna measurements at several object locations near the antenna to extract features that can be used to indicate the object presence and relate the change in antenna measurements to the distance to the metallic object within the near field.
4. Design and develop an Ultra-Wide Band (UWB) antenna that conforms to the WBAN requirements of size while achieving very low sensitivity when it comes in contact with the human body. Also, perform a parametric study and parameters optimisation of the proposed antenna to achieve the required antenna performance.
5. Conduct on-body tests to validate and identify the proposed antenna performance for on-body near field sensing through placing the antenna on several human body parts while placing the metallic objects at several distances from the antenna. The tests aim to compare the change in antenna measurements due to the human body presence and the metallic object presence; Also, the tests aim to assess the on-body antenna sensitivity to metallic object within the near field.

1.4 Contributions to Knowledge of the Thesis

In the achievement of the above research objectives, the following contributions have been made:

- After investigation of low profile antenna measurements nearby a metallic object the work manage to quantify the changes in antenna return loss and draw a relation between the changes in the antenna return loss and the distance to the object. The relation depend on both magnitude and resonant frequency of the return loss, obtained from experimental tests using a commercial 2.4GHz low profile antenna in free space.
- Based on the problems identifed, a novel UWB WBAN antenna has been designed and fabricated. The antenna consists of two Vivaldi shapes and a curved reflector. The antenna performance was tested off-body and on-body.
- The role of the antenna reflector in increasing the antenna's sensitivity to nearby metallic objects while decreasing its sensitivity to the human body, was studied and demonstrated through a set of on-body experimental setups.
- Two features to estimate the distance between the proposed antenna and the nearby metallic objects were proposed. These two features are extracted from the absolute change in the frequency response of the antenna reflection coefficient using root mean square and peak-to-peak values, respectively.
- The use of Principal Component Analysis classifier was proposed to detect the

passive object location relative to line of sight between two antennas. Frequency response of the reflection coefficient and the transmission coefficient of one antenna were fed to the classifier. The method showed promising results using the narrow band antenna as well as the proposed UWB antenna.

1.5 Publications Arising From This Research

Journal Papers

J1. **W. Amer**, A. Sabaawi, J. Zhang, and G. Y. Tian, "A Compact Dual-Vivaldi sensor-based UWB antenna for WBAN applications," submitted to *IEEE Transactions on Antennas & Propagation*.

Conference Papers

C1. **W. Amer**, G. Y. Tian, and C. Tsimenidis, "Sensing passive object existence within an antenna near field based on return loss," in *Antennas and Propagation Conference (LAPC)*, 2014 Loughborough, 2014, pp. 400–404.

C2. **W. Amer**, G. Y. Tian, and C. Tsimenidis, "A novel, low profile, directional UWB antenna for WBAN," in *Antennas and Propagation Conference (LAPC)*, 2014 Loughborough, 2014, pp. 708–710.

1.6 Thesis Outline

This thesis is organised as follows. Chapter 2 presents the background information on wireless body area network technology, protocols and applications. The chapter also discusses the related works and the state of context in the area of the context-aware sensor network and near-field sensing.

Chapter 3 presents a study of the effects of metallic objects on antenna measurements within the near field. This is presented through a set of experiments inside an anechoic chamber, using a low profile, narrow band antenna, and the results are validated through simulation, using CST Microwave Studio. The chapter also analyses the change in the antenna measurements and proposes several indicators to relate the changes in antenna return loss to the distance between the antenna and the nearby object within the near field.

Chapter 4 presents the design concept and performance analysis of a novel UWB WBAN antenna that is characterised by its low profile and low sensitivity to the human body. Also, a parametric study of the antenna parameters is presented, as well as an

investigation of the reflector effects on the antenna. Then the chapter presents an experimental setup to test the antenna performance.

Chapter 5 investigates the combined effects of the human body and metallic objects on the measurements of the proposed antenna. The chapter presents a set of on-body experimental setups that involve placing the antenna on several body parts with and without a metallic object, followed by a comparison of the changes in antenna s-parameters. Next, the chapter presents a detailed data analysis of the measurements, whereby two indicators for object distance from the antenna are proposed. Then, a methodology for using the Principal Component Analysis classifier to detect object existence is presented. Finally, conclusions and future work are outlined in Chapter 6.

Chapter 2 BACKGROUND AND RELATED WORK

2.1 Chapter Outline

This chapter presents theoretical background and state-of-the-art WBAN technology, as a foundation to the following chapters of this thesis. Section 2.2 lists basic definitions and theoretical background about antenna and wireless signal propagation, while Section 2.3 defines the WBAN technology and related communication protocols, with an emphasis on the physical layer issues. Finally, Section 2.4 presents a literature review of recent related works. The literature review involves several examples of far field and near-field sensing systems and their applications, as well as examples of studies about the interaction between the human body and nearby passive objects in WBAN.

2.2 Antenna Theory Fundamentals

The following subsections present a brief background about antenna measurements, antenna field regions and electromagnetic propagation models.

2.2.1 Antenna Measurements

There are several measurements to assess the performance of an antenna, depending on the field of application where the antenna will be used. However, a good starting point in the testing process of most antennas is to measure the antenna radiation pattern, antenna efficiency and antenna gain. The antenna radiation pattern is defined as a mathematical function or a graphical representation of the angular variation of radiation around the antenna, typically in the far field [40]. The radiation pattern can be referenced as a specific radiation component at a given polarisation or the absolute radiation of all the components. The antenna efficiency term can refer to the number of efficiencies related with the antenna, mainly, radiation efficiency (e_{cd}) and total efficiency (e_T). *Radiation efficiency* refers to the ratio of the radiated power to the accepted power fed to the antenna, whereby the difference between the two values of power comes from conduction loss and dielectric loss. On the other hand, *total efficiency* refers to the ratio of radiated power to the input power fed to the antenna. In other words, the total efficiency of an antenna is the radiation efficiency multiplied by the impedance mismatch loss (e_r) of the antenna, as given by [40]

$$e_T = e_r e_{cd} = e_{cd}(1 - \Gamma^2)\,, \tag{1}$$

where Γ is the voltage reflection coefficient at the input terminals of the antenna.

Another useful measure describing the performance of an antenna is the gain. The *gain* is defined as the ratio of the intensity, in a given direction, to the radiation intensity that would be obtained if the power accepted by the antenna were radiated isotopically. When the direction is not stated, the power gain is usually considered in the direction of maximum radiation [40].

2.2.2 Field Regions and the Friis Transmission Equation

The space around an antenna can be divided into two regions, based on the behaviour of the transmitted signal: the far field and the near field. In the far-field region, the fields exhibit local plane wave behaviour, and the transmission follows the Friis Equation, given by [41]

$$\frac{P_r}{P_t} = \left(\frac{\lambda}{4\pi R}\right)^2 G_t G_r \,, \tag{2}$$

where P_t is the transmitted power, P_r is the received power, G_t and G_r are the transmitting and receiving antenna gains, respectively, and *R* is the distance between the two antennas. The near-field region is closer to the antenna and is divided into a radiated near field, where the radiation (real-valued) fields dominate over the reactive fields, and a reactive near field, where the reactive fields dominate over the radiation fields near field. The boundaries of these regions depend on the transmitted signal wavelength (λ) and the antenna's largest dimension (D). However, the exact definitions of these boundaries change from one antenna type to another [42].

For an electrically small antenna (defined as D/2 ≪λ), the radius, *r*, for each region boundary is calculated as follows [42]:

$$r_{reactive\ near\ field} = \frac{\lambda}{2\pi}, \tag{3}$$

$$\frac{\lambda}{2\pi} < r_{radiated\ near\ field} \leq 5\,\lambda\,, \tag{4}$$

$$r_{far\ field} > 5\,\lambda. \tag{5}$$

And for larger antenna, such that D>2.5λ, these boundaries become

$$r_{reactive\ near\ field} = 0.62\sqrt{D^3/\lambda}\,, \tag{6}$$

$$0.62\sqrt{D^3/\lambda} < r_{radiated\ near\ field} \leq \frac{2D^2}{\lambda}, \tag{7}$$

$$r_{far\ field} > \frac{2D^2}{\lambda}. \tag{8}$$

In the case of using a 1/4-wave dipole antenna that works in 2.4GHz, the antenna's electrical length (approximately 3cm) is considered small compared to the wavelength, which is around 12cm; hence, the equation for an electrically small antenna should be applied.

2.2.3 Two Rays Model

Obstacles placed near two communicating antennas usually reflect the radio wave incident upon their surface and produce multipath components on the receiver's side. The received signal will be a combination of direct and reflected waves. In an indoor, multipath-rich environment, the received signal can be greatly degraded by this effect.

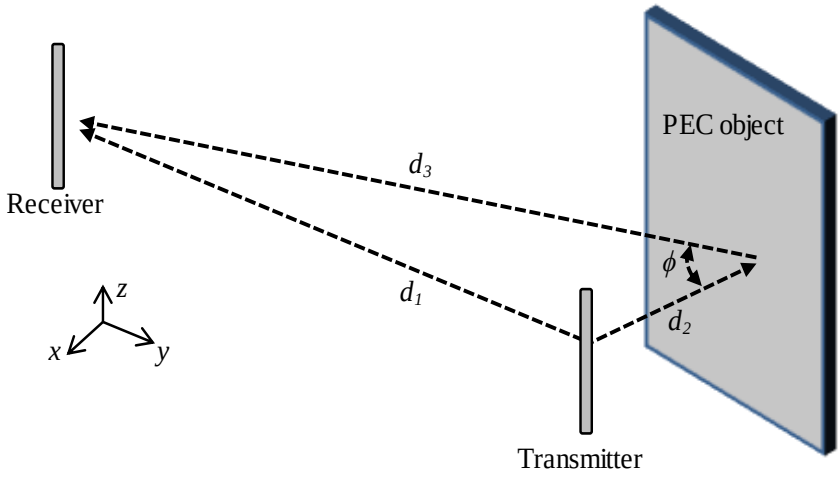

Figure 2: Two ray RF propagation model

Figure 2 shows the two-ray propagation model, where two antennas are fixed near a Perfect Electric Conductor (PEC) object or ground. The distance between the transmitting and receiving antennas is d_1, which also represents the Line OF Sight (LOS) component path. On the other hand, d_2 and d_3 represent the distances between the object and the transmitting and receiving antennas, respectively. The triangle d_1, d_2 and d_3 lies in the incidence wave plane. Then, the direct path d' and indirect path d'' can be defined as [41]:

$$d' = d_1 , \tag{9}$$

$$d'' = d_2 + d_3 . \tag{10}$$

Assuming the space around the antennas is free space and $\mu_1 = \mu_2$, the two ray model can be simplified, and the total received E-field , E_{TOT}, is then a result of the direct line-of-sight component, E_{LOS}, and the reflected component, $E_{REFLECT}$. If E_0 is the free space E-field at a reference distance d_0 from the transmitter, then for $d>d_0$, the free space propagating the E-field is given by $E(d,t)$. The E-field, due to the line-of-sight

component and reflection component at the fixed receiving antenna, can be expressed as [41]

$$E_{LOS}(d', t) = \frac{E_0 d_0}{d'} \cos\left(w_c\left(t - \frac{d'}{c}\right)\right), \tag{11}$$

$$E_{REFLECT}(d", t) = \Gamma \frac{E_0 d_0}{d"} \cos\left(w_c\left(t - \frac{d"}{c}\right)\right), \tag{12}$$

where Γ is the object reflection coefficient. For PEC at normal incidence, the reflection coefficient (Γ) = -1. Assuming both antennas are vertically polarised, we obtain

$$E_{TOT}(d, t) = \frac{E_0 d_0}{d'} \cos\left(w_c\left(t - \frac{d'}{c}\right)\right) + (-1)\frac{E_0 d_0}{d''} \cos\left(w_c\left(t - \frac{d''}{c}\right)\right). \tag{13}$$

If the object is very close to one antenna, then

$$\because\ d_1 \approx d_3 \gg d_2. \tag{14}$$

The amplitudes of $E_{d'}$ and $E_{d''}$ are virtually identical and differ only in phase:

$$\therefore \left|\frac{E_0 d_0}{d}\right| \approx \left|\frac{E_0 d_0}{d'}\right| \approx \left|\frac{E_0 d_0}{d''}\right|, \tag{15}$$

$$E_{TOT}(d, t) = \frac{E_0 d_0}{d}\left(\cos\left(w_c\left(t - \frac{d'}{c}\right)\right) - \cos\left(w_c\left(t - \frac{d''}{c}\right)\right) \right), \tag{16}$$

$$|E_{TOT}(d)| = \frac{E_0 d_0}{d}\sqrt{2 - 2\cos\theta}\ . \tag{17}$$

Therefore, the received E-field, evaluated over frequency, shows oscillation, as in Figure 3.

2.2.4 Skin Depth

The skin depth, δ_s, of the medium is the distance that characterizes how well an electromagnetic wave can penetrate into a conducting medium, and it is calculated as follow:

$$\delta_s = \sqrt{\frac{\rho}{\pi f \mu_0 \mu_r}} \quad (m), \tag{18}$$

where μ_0 is the free space permeability which equals $4\pi * 10^{-7}$, μ_r is the relative permeability of the medium, f is the frequency of the current in Hz, and ρ is the resistivity of the medium in Ω .m. In a perfect dielectric, $\rho = \infty$, therefore $\delta_s = \infty$.Thus, in free space, a plane wave can propagate with no loss in magnitude indefinitely. On the other extreme, if the medium is a perfect conductor with $\rho = 0$, hence $\delta_s = 0$. For example, the iron. The iron relative permeability is ranging from hundreds to hundreds of thousands based on its purity. For pure iron with relative permeability equals to 4000, and resistivity equals to $0.1*10^{-6}\ \Omega$. m, the iron skin depth at 2.4GHz is $\delta_s \approx 51.3*10^{-9}$ meter.

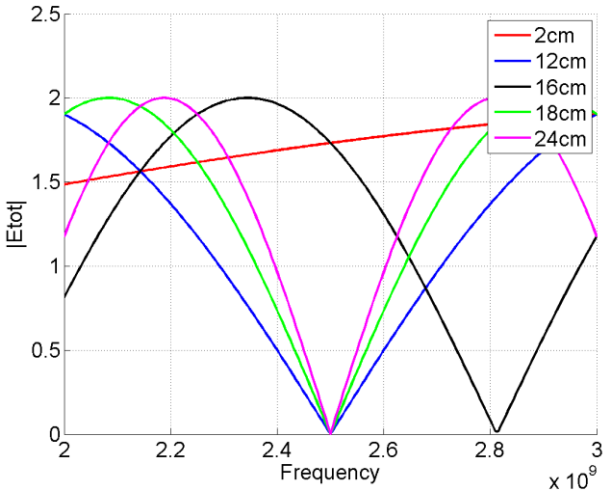

Figure 3: Normalised E-field at the receiver side

2.2.5 Radiation Pattern of an Antenna in Front of a PEC Surface

The current distribution for an omnidirectional dipole antenna placed vertically parallel to the z-axis is shown in Figure 4. The radiation pattern in the XY-plane is a unit circle, while the pattern in the XZ-plane is defined as [42]:

$$F(\theta) = \frac{\cos\left[\left(\frac{\pi}{2}\right)\cos\theta\right]}{\sin\theta} \ . \qquad (19)$$

To obtain the radiation pattern of the antenna in front of the PEC surface, image theory is used to create an equivalent problem, yielding the same fields for z>0, by removing the ground plane and introducing an image dipole of the same length, which is parallel to the source dipole and equidistant from the PEC surface; thus, $d=\lambda/2$. This is shown in Figure 5, where the image dipole will have an amplitude excitation equal to the source dipole and be 180^0 out of phase. This can be modelled as an array antenna of two elements of the same amplitude and opposite phase. Hence, the array factor is given by [42]:

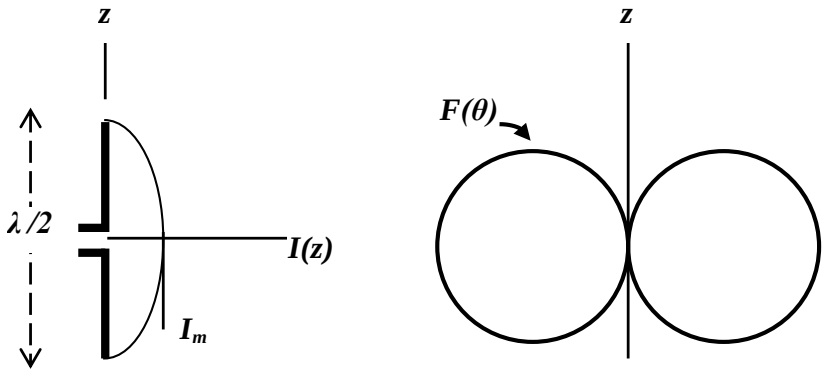

(a) (b)

Figure 4: The half-wave dipole: (a) Current distribution I(z); (b) Radiation pattern F(θ)

$$AF = 2j \sin\left(\beta \frac{d}{2} \cos\theta\right). \tag{20}$$

The element is a half-wave dipole, not oriented along the z-axis as usual, but along the X-axis, as shown in Figure 5. The element pattern is then given by

$$g_a(\theta, \varphi) = \frac{\cos[(\pi/2)\sin\theta\cos\varphi]}{\sqrt{1 - \sin^2\theta\cos^2\varphi}}. \tag{21}$$

The complete pattern is obtained by multiplying the array factor by the element pattern:

$$F(\theta, \varphi) = g_a(\theta, \varphi) * AF. \tag{22}$$

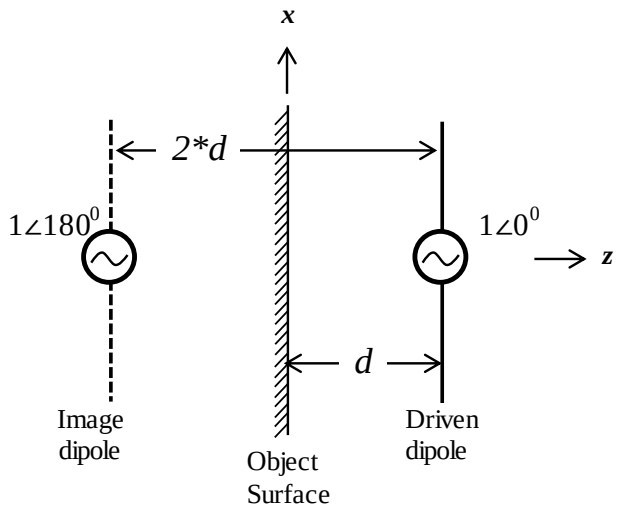

Figure 5: A half-wave dipole parallel to the PEC surface

The principal plane patterns using this function are plotted in Figure 6 for various distances *d*. The radiation in the back half plane (z<0) is not plotted, because the fields are zero there, due to the shorting effect of the object surface [42].

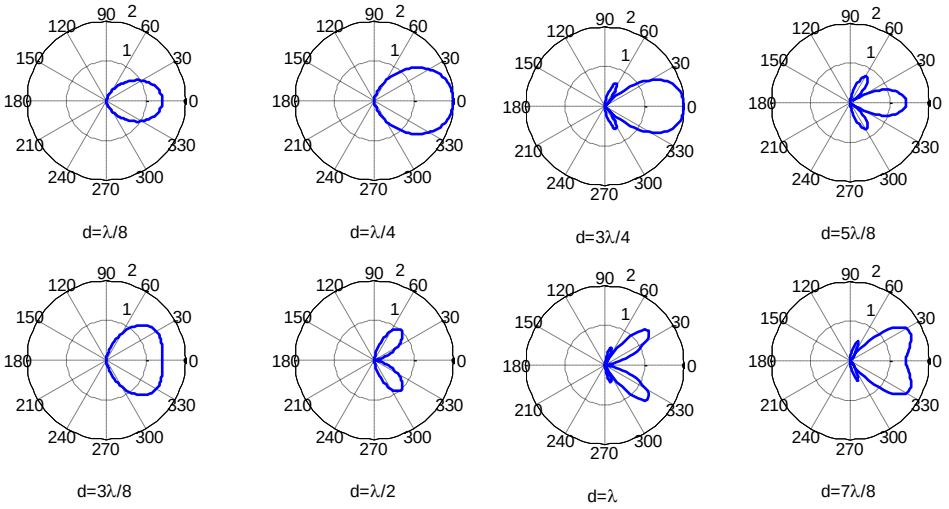

Figure 6: The E-plane pattern (xz pattern) for various distances *d*

2.2.6 Antenna Impedance

The input resistance R_A represents dissipation, which occurs in two ways. Power that leaves the antenna and never returns (i.e., radiation) is one part of the dissipation. There are also ohmic losses, just as in a lumped resistor. Electrically small antennas can have significant ohmic losses, but other antennas usually have ohmic losses that are small compared to their radiation dissipation. The input reactance X_A represents power stored in the near field of the antenna. The reactance of a short dipole is approximated by [42]:

$$X_A = -\frac{120}{\pi\frac{\Delta z}{\lambda}}\left[ln\left(\frac{\Delta z}{2a}\right) - 1\right] \ \Omega \ , \tag{23}$$

where a is the dipole diameter and Δz is the antenna's length.

Generally, antennas are designed with almost zero reactance, to match the transmitter/receiver circuit impedance; however, sometimes a matching circuit is needed. Nevertheless, the input impedance of the antenna will be affected by the other antennas or objects that are nearby [42].

2.2.7 S-parameter and Two Ports Network Model

Modelling an antenna as a two-port network is a common procedure in simulation and testing to acquire the antenna's specifications, such as return loss over a frequency range in terms of the S-parameters [43-45]. S-parameters have advantages over other parameters, such as impedance, admittance and h-parameters at microwave and high frequencies, where it is difficult to measure the equivalent voltages and currents [42].

The output voltage at each port is related to the input voltages through S-parameters, as follows:

$$b_1 = a_1 * S_{11} + a_2 * S_{12} , \quad (24)$$

$$b_2 = a_1 * S_{21} + a_2 * S_{22} , \quad (25)$$

where a_1 and a_2 are the input signals at antenna#1 and antenna#2, respectively, and b_1 and b_2 are the output signals for the antennas. The S-parameters are S_{11}, S_{21}, S_{12} and S_{22}. Using Vector Network Analyser (VNA), each of these measurements is represented by a complex value over the frequency range.

During communication, if only antenna#1 is transmitting, then:

$$a_2 = 0 , \quad (26)$$

therefore, (24) and (25) are reduced to

$$S_{11} = b_1/a_1 , \quad (27)$$

$$S_{21} = b_2/a_1 . \quad (28)$$

According to (4) and (5), S_{11} represents the antenna's reflection coefficient, while S_{12} represents the transmission coefficient. A similar conclusion can be drawn for S_{22} and S_{21}, when antenna#2 is the transmitter and antenna#1 is the receiver.

Assuming that both antennas have the same physical characteristics and are fed with the same power level, S_{22} is equivalent to S_{11}, with slight differences due to manufacturing imperfections. On the other hand, if the transmission medium between the two antennas is linear and isotropic, but not necessarily homogeneous, S_{21} and S_{12} are the same, due to the reciprocity theorem [42].

2.3 Wireless Body Area Network: Definitions and Challenges

WBAN is defined as a group of wireless nodes that are placed around, on and inside the human body and that aim to monitor human physiological information and track the human's activity. In general, WBAN has emerged in recent years as a special class of wireless sensor networks; hence, WBAN inherits many of the wireless sensor network characteristics and challenges. A detailed discussion about the challenges and requirement variances between WSN and WBAN is presented in [1]. On the other hand, a brief discussion of the differences between body area network and its predecessors i.e. wearable sensing and personal area network is presented in [46], as well as a review of the current challenge in RF modelling and hardware design of sensor nodes of body area network.

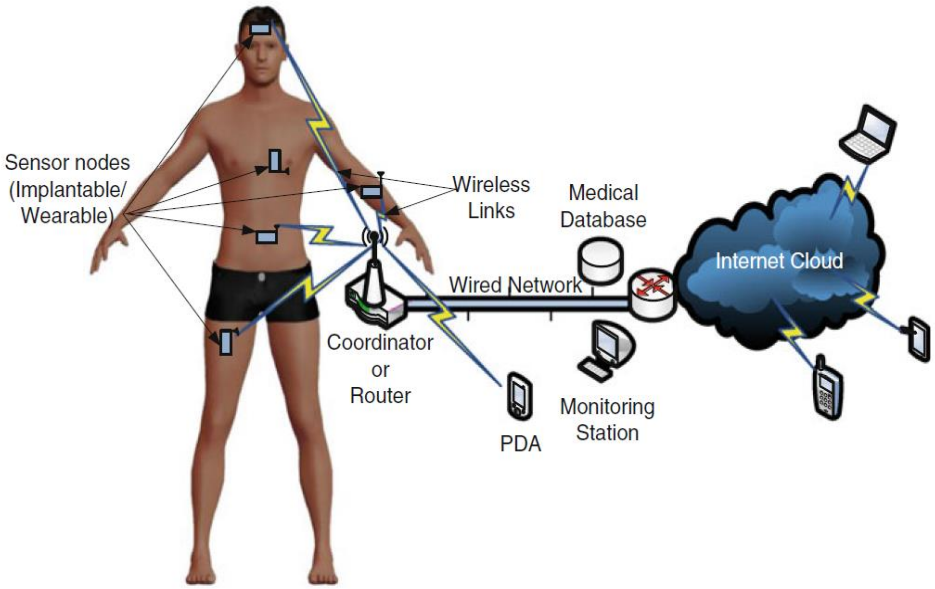

Figure 7: Key components of a WBAN (adapted from [1])

Figure 7 presents an example of a medical application of WBAN, which consists of a group of relatively small sensor nodes attached to the human body, in addition to a router node. The router node enables the body network to connect to the outside world: WPAN, Wireless Local Area Network (WLAN) and the Internet. Unlike sensor nodes, the router node is equipped with more powerful transmission and processing capabilities and a higher power supply.

Based on the nodes' distribution around the human body, the WBAN channel can be classified into three types [47]:

1. Off-Body channel: represents the communication between sensor node on the human body with an external wireless device, such as a router or mobile phone.
2. On-Body channel: represents the communication between two sensor nodes mounted on the human body's surface.
3. In-Body channel: represents the communication with a sensor node planted inside the human body. The other party involved in the transmission can be a sensor node mounted on the body's surface or an external device.

The next subsections present more details on the communication protocols used in WBAN and on the WBAN node requirements, with an emphasis on the challenges of the physical layer.

2.3.1 Physical Layer Protocols used in WBAN Applications

This section briefly discusses three wireless technologies that are widely used by the WBAN research field: IEEE 802.11, IEEE 802.15.4 and IEEE 802.15.6.

2.3.1.1 IEEE 802.11 Standard

IEEE 802.11 is a set of media access control (MAC) and physical layer (PHY) specifications for implementing wireless local area network (WLAN) computer communication. Several variations of the standard are available, based on the used frequency band. The standards 802.11b and 802.11g [48] work in the 2.4-GHz band, while IEEE 802.11a [49] works in the 5-GHz band. Also, these standards use different physical-layer communication mechanisms; for example, 802.11b and 802.11g control their interference and susceptibility to interference by using direct-sequence spread spectrum (DSSS) and orthogonal frequency-division multiplexing (OFDM) signalling methods, respectively. In general, this standard has been implemented successfully in many applications; however, it is rarely used for WBAN applications, due to its high power requirements.

2.3.1.2 IEEE 802.15.4 Standard

IEEE 802.15.4 [50] is a standard that defines the physical layer and media access control for low-rate, wireless personal area networks. It is maintained by the IEEE 802.15 working group, which defined the standard in 2003. The MAC layer of the IEEE 802.15.4 standard is based on Carrier Sense Multiple Access with Collision Avoidance (CSMA/CA) for media access. The physical layer of the IEEE 802.15.4 standard supports 16 channels of 250 kbps each in 2.4 GHz, in addition to 10 channels of 40 kbps each in 915 MHz and one channel of 20 kbps in the 868-MHz band.

The IEEE 802.15.4 standard is usually used in conjugate with other standards, such as ZigBee [51], which define the network, security and application layers. The ZigBee network topology defines three levels of nodes: coordinator nodes, router nodes and end devices. A ZigBee coordinator node initiates the network and manages network resources. ZigBee router nodes enable multi-hop communication between the devices in a network. Both coordinator and router nodes are supposed to have more reliable power source and more hardware capabilities compared to the end devices. ZigBee's end devices communicate with parent nodes (router nodes or coordinator nodes) and operate with

minimal functionality in order to reduce the power consumption. This standard is widely used by many WSN and WBAN applications and research groups. Since both IEEE802.11 and IEEE802.15.4 have been widely applied in many applications, several research groups focused on studying the coexistence between the two standards in WSN [52, 53] as well as WBAN [54, 55].

2.3.1.3 IEEE 802.15.6 Standard

Unlike the two standards explained earlier, the IEEE 802.15.6 [56] is proposed specifically for (but not limited to) the use of the human body network. It defines three physical layer specifications:

a. Narrow band communication, which consists of several channels available in unlicensed frequency bands, such as the Industrial, Scientific and Medical Radio (ISM) bands at 434MHz, 915 MHz and 2.45GHz, as well as the 403 MHz band, which are used for medical implant communication services.
b. Ultra-wideband communication, where the UWB spectrum in the range of 3.1–10 GHz is divided into eleven channels, with a channel bandwidth of 499.2 MHz for each channel.
c. Human Body Communications (HBC), whose signal carrier in the physical layer is the electric current through the human body, instead of a wireless electromagnetic transmission. It operates in the 21-MHz frequency band, characterised by a 5.25-MHz bandwidth. The supported data rate ranges from 164 kbps to 1.3125 Mbps.

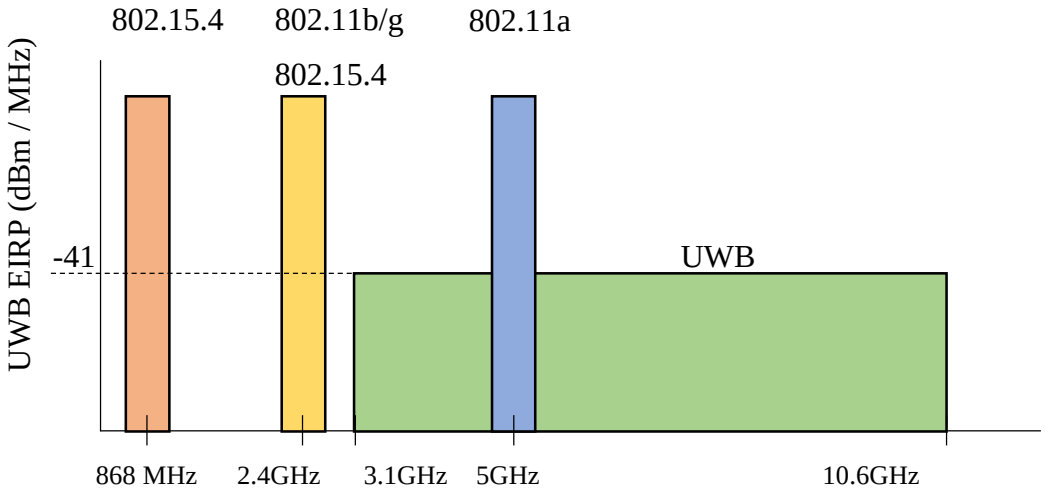

Figure 8: Transmit spectrums for the widespread protocols used by WBAN applications

Many aspects of IEEE 802.15.6 have been modified from its ancestor to fit the requirements of a wearable implant network. For example, the scheduled access provides guaranteed periodic access, allowing nodes to wake up at specific time intervals. Therefore, it is suitable for medical data streaming applications e.g., Electrocardiogram (ECG) waveform data streaming.

2.3.2 Antenna Requirements for WBAN

Antenna efficiency is typically the first requirement to consider with regard to selecting an antenna in any application, yet different applications require different antenna properties, such as directionality and power level. For WBAN, the human body's composition and the nature of the collected information impose some restrictions on the antenna design, which are uniquely applied to this type of network.

These restrictions are:

- Directional radiation pattern: Antennas mounted on the human body's surface are required to be omnidirectional and yet have minimum radiation towards the human body [6, 57, 58].
- Small size: small antenna dimensions are typically required for all WBAN applications; however, the small size of the design affects the antenna radiation efficiency for low frequencies and the antenna directionality [6, 58].
- Vertically polarised: To maintain the minimum absorption of the signal by the body tissues, the E-field of the transmitted signal is preferred to be perpendicular to the human body's surface [6, 7].
- High fidelity factor: fidelity factor is a requirement for the communications and measurements quality of the UWB impulse response [59-61].
- In addition to the quantitative requirements listed above, most WBAN antennas are required to meet some qualitative requirements, e.g., that they be flexible, washable and durable. The antennas are also required to be unobtrusive, i.e., weaved into the user's clothes or integrated with his/her accessories. This makes the WBAN products more socially acceptable to wear, since in many medical applications, a flashy distinctive design can cause feelings of stigma in the user [57].

2.3.3 Designs and types of WBAN antenna

Micro strip and loop designs are generally applied for on-body antennas because of their conformability and light weight. However, for several on-body links (i.e., links formed between on-body antennas placed on the user's body), and for many body postures, quarter-wavelength (λ/4) monopole antennas fixed on a small ground plane have been shown to perform even better [2, 62]. The main reason is that the monopole antenna exhibits an omnidirectional radiation pattern, which is highly preferable in cases where the geometry and the characteristics of the wireless link are unknown [2]. Many recent designs have been reported for WBAN applications and were showed to meet WBAN requirements with regards to impedance and radiation pattern, e.g. PIFA antenna [63], textile PIFA antenna [64], Loop antenna [65], embroidered and woven patch antennas [66], and 3D antennas [6, 7]. On the other hand, some antenna design are specific for application regarding its place on the human body such as user's ear [14, 67], mouth [68], and foot [69]. These antenna proposed generally for WBAN use and were tested using model for skin or human torso. Figure 9 shows examples of designs for WBAN antennas in recent literature.

2.4 Related Work in Antenna-Based Sensor Techniques and Applications

The use of radio wave to sense passive object presence is as old as the invention of Radar systems [70-72] as well as the microwave imaging [73-75], and currently, several researches proposed the use of antennas as sensors beside their typical function in the communication process. This section review some of these researches and focus on the works that employ low profile antenna. Based on the sensing range and the antenna type, the next subsections discuss and classify recent works in the field of passive object sensing into three categories. The first and second categories handle works that use low profile antennas as sensors in the far field and the near field respectively. The third category discusses recent works that use antennas specifically designed to serve as sensors but not for communication process.

2.4.1 Related Work in Far Field Sensing

The acquisition of information about a passive object or phenomenon without making physical contact with the object is a well-defined topic in the fields of radar systems and remote sensing. However, the rise of WSN technology in the last decade and the availability of miniaturised wireless nodes at low cost open the door to implementing RF-based sensing and monitoring at a smaller level that fits in an indoor environment.

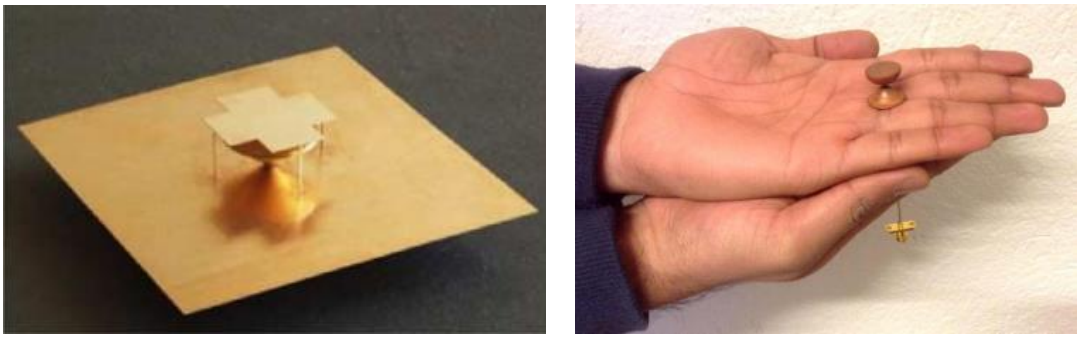

(a)

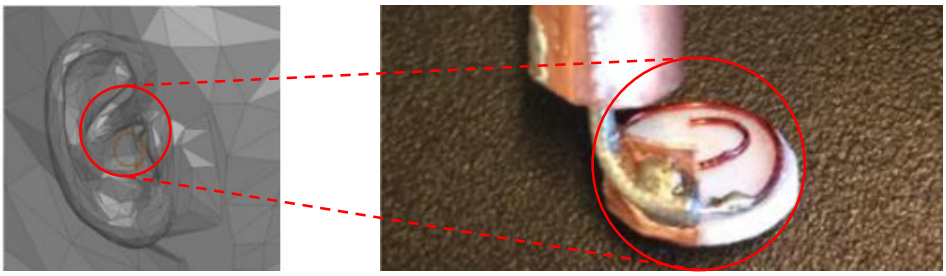

(b)

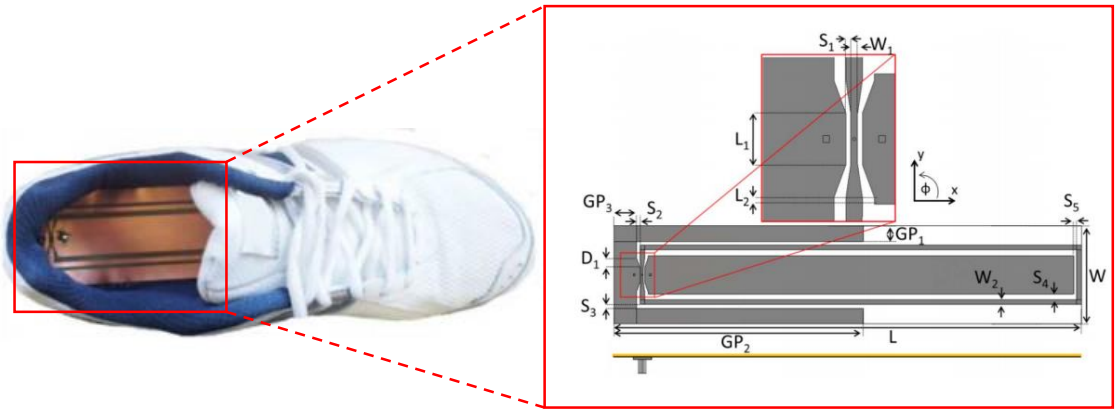

(c)

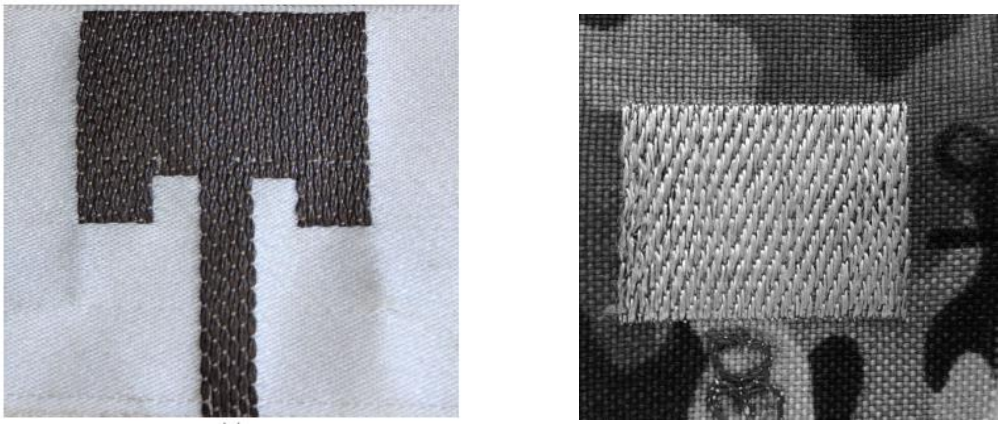

(d)

Figure 9: Examples of recent designs for WBAN antennas (a) 3D antenna (adapted from [6]), (b) in-the-ear spiral monopole antenna (adapted from [67]), (c) insole antenna (adapted from [69]), (d) embroidered and woven antennas (adapted from [66])

Such technology has many applications, ranging from touchless gaming controls to pervasive indoor monitoring. It makes use of the abundance of nodes in a typical sensor network to compensate for the low capabilities of each individual node. The details of two recent cases that implement far field sensing in indoor environments are discussed below.

2.4.1.1 Radio Tomographic Imaging

J. Wilson and N. Patwari proposed and designed a Radio Tomographic Imaging (RTI) system [76, 77] for passive object monitoring, using commercially available WSN nodes. Compared to other methods of monitoring, such as cameras, the RTI system provides a better alternative, since the RF signals can travel through walls. RTI does not need a light source; hence, it also can function in a dark environment. Moreover, the RTI system has been useful for applications in which the location has been important, but the monitored person has preferred for his or her identity to be unknown. Their suggested applications for such systems included helping the correctional and law enforcement officers by showing the location of people during indoor emergencies, such as hostage situations or building fires. Also, they suggested that the system is convenient to control and monitor 'smart homes', where the operation cycles of heating and lighting systems are adapted to human existence inside the building.

Their initial setup of the system consists of 28 wireless nodes distributed evenly along the perimeter of a 6.4 × 6.4 m^2, surrounding a total area of 41 m^2. Each node is fixed on a wooden stand, 1.5 m above the ground. Each node sends and receives signals from all of the other nodes over the 2.4-GHz frequency band. Then, each pair of nodes sends the value of the Received Signal Strength (RSS) of the link between them to a base station to have the dada analysed. The RSS value is averaged over a 30-second period, which results in approximately 100 RSS samples from each link. The presence of a human causes shadowing to some of the links between the nodes. By solving the inverse problem for all of the links, the human's location can be determined. The results showed the ability of the system to detect a human's location within a 0.15-m accuracy. Figure 10 shows an illustration of the RTI system and the final reconstructed image that displays the object's location. Later, the authors presented a modified version of the system to track a moving object in an indoor environment, using a network fixed outside the building [78]. Also, they presented a non-invasive respiration monitoring technique, which uses the same technique to monitor the breathing of an otherwise stationary person [79]. The results

showed that the breathing rate can be estimated within an error of 0.1 to 0.4 bpm, using 30 seconds of measurements.

It is worth to mention that the first attempt to use a low profile antenna as sensor in the far field was presented by [80]. Similar systems that use the concept of wireless tomography in WSN were independently presented in [81-83]. Moreover, a brief survey of the wireless tomographic imaging can be found in [84-86]. Also, RF localization for passive object was presented in [87] to achieve safe interaction scheme between human and robot in industrial environment.

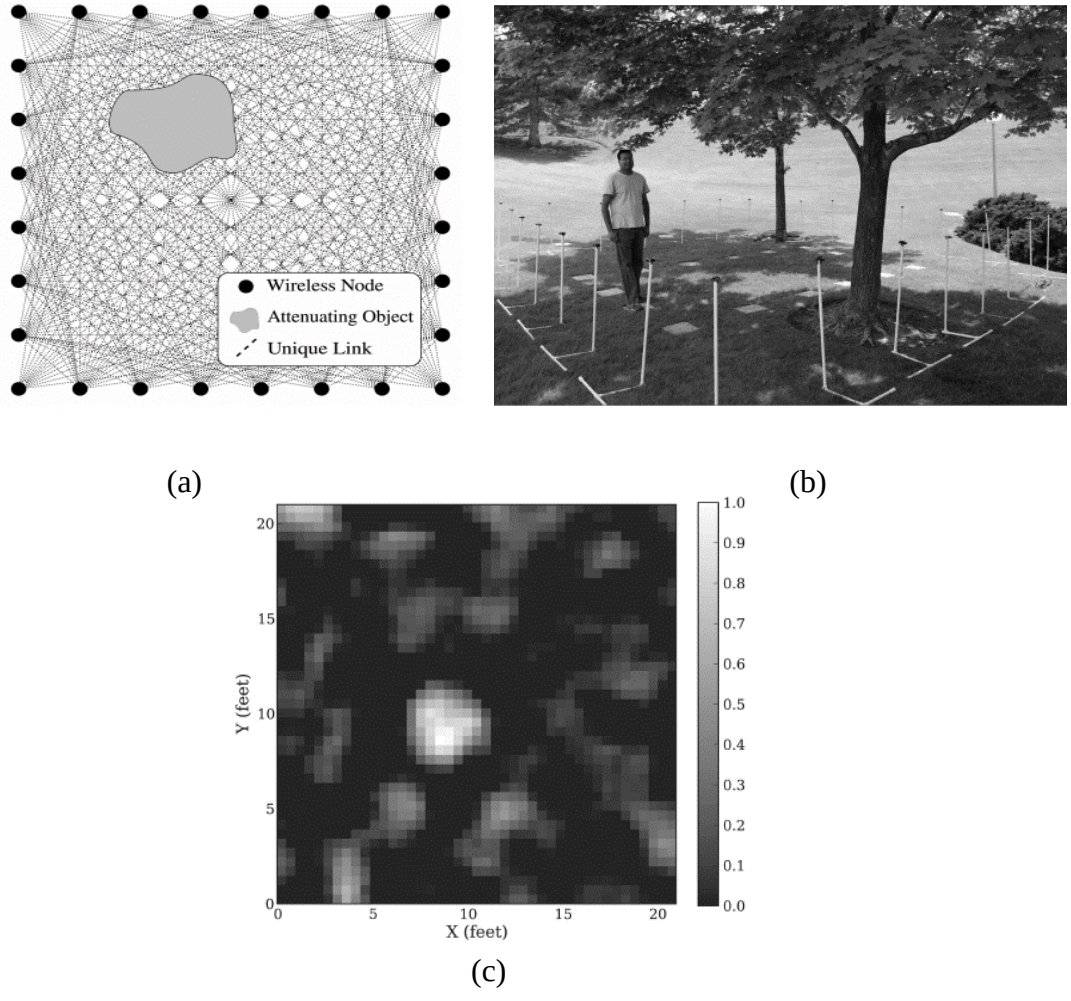

Figure 10: RTI system description (adapted from [76]): (a) an illustration of an RTI network; (b) a photograph of the deployed network with an participant; (c) constructed images of attenuation in the wireless network.

2.4.1.2 Gesture Recognition Using Wireless Singals

Qifan Pu and his colleagues presented a whole-home gesture recognition system, using a wireless signal named WiSee [88]. Unlike commercially available systems, e.g., Kinect

[89], WiSee requires neither an infrastructure of cameras nor user instrumentation of the devices.

Like the RTI system, Wisee enables applications in diverse domains, including home-automation, elderly health care and gaming. Using a swiping hand motion in-air, a user could control the music volume while showering, change the song playing on a music system in the living room while cooking, or turn up the thermostat while in bed. However, unlike the RTI system, WiSee doesn't depend on the signal attenuation within a large matrix of wireless nodes. Instead, it is based on a smaller number of nodes (typically Wi-Fi transceivers) and uses the Doppler shift in the received signal as a signature to identify the gesture. WiSee's proof of concept was implemented in GNU Radio, using the USRP-N210 hardware. Their results show that WiSee can identify and classify a set of nine gestures with an average accuracy of 94%. Figure 11 shows the proposed gestures and their corresponding Doppler shift signature. More information about the WiSee system can be found on their website [90]. A similar technique presented by Microsoft Research [91] provides a good example of human body interaction with its surrounding environment, however it doesn't use the antenna as sensor.

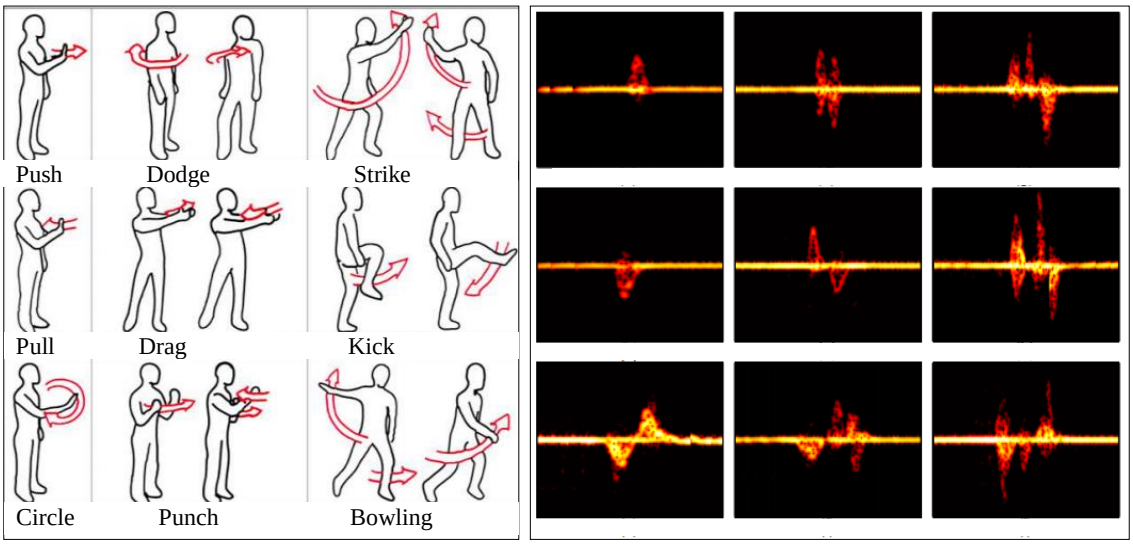

(a) (b)

Figure 11: WiSee system (adapted from [88]): (a) the proposed nine gestures for WiSee; (b) frequency–time Doppler profiles of the gestures

2.4.2 Related work in Near-Field Sensing

Near-field sensing takes place within the small region around the wireless device antenna, typically less than a few wavelengths. Hence, near-field sensing techniques

depend on the change in the antenna impedance, unlike the far field sensing techniques that depend on far field measurements, such as multipath shadowing and Doppler shift. The presence of objects or change of environmental conditions in the vicinity of an antenna leads to a shift in both the phase and magnitude of the antenna resonant frequency. Also, near-field sensing researches mainly focus on using measurements from single nodes, rather than a fusion of data from many nodes, as in far field sensing techniques. The details of selected recent researches of the near-field sensing techniques are discussed below.

2.4.2.1 Vital Sign Detection Based on Antenna Reflection Coefficient

Many recent works studied the detection and monitoring of human vital signals, e.g., heartbeat rate and respiratory system rate, based on the change in a nearby wireless link. These systems can detect vital signs from distances of 1 to 2 m. Some of these systems depend on far field measurements, such as the direction of arrival [92] or Doppler shift [93] of the received signals, while other depend on the antenna reflection coefficient [94, 95]. The far field measurements are highly affected by any slight human motion, which results in unreliable measurements.

Yong-Jun and colleagues [94] presented a vital sign detection sensor, based on the reflection coefficient variance from an antenna used in wireless communication devices. Unlike other works, they used a vital sign detection scheme based on the magnitude variation of the reflection coefficient from an antenna, so that it could be designed and placed as a parasite component in a conventional transceiver system.

The characteristics of the reflection coefficient of a dipole antenna are used as measurements of the vital signal in the near-field region. Since the human body has a different permittivity than the air, placing a human subject in the near field of the antenna shifts its resonant frequency and affects both the magnitude and phase of the reflection coefficient. The antenna was designed and matched at the 2.4-GHz ISM band, and it was connected to the base station through a 20-dB directional coupler and a power amplifier, as shown in Figure 12. The antenna was placed at several distances, from 1 cm to 61 cm, from a volunteer chest to cover the antenna near-field region. Their results showed close matching, with the reference signal measured using a piezo-electric finger pressure sensor for short distances. Analysing the data in the frequency domain showed the system's ability to correctly detect the heartbeat rate, even at 50 cm [94].

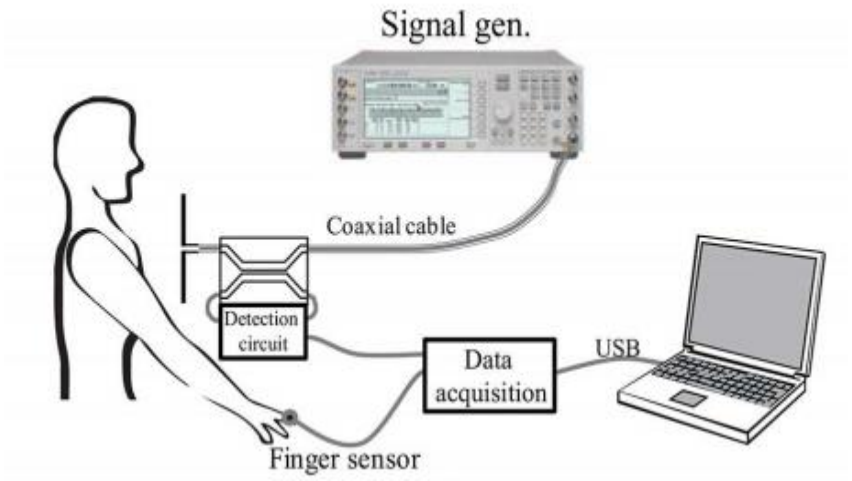

(a)

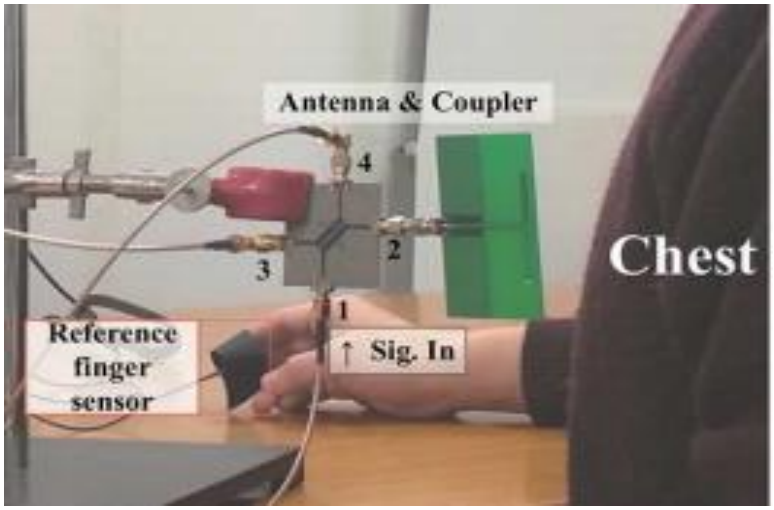

(b)

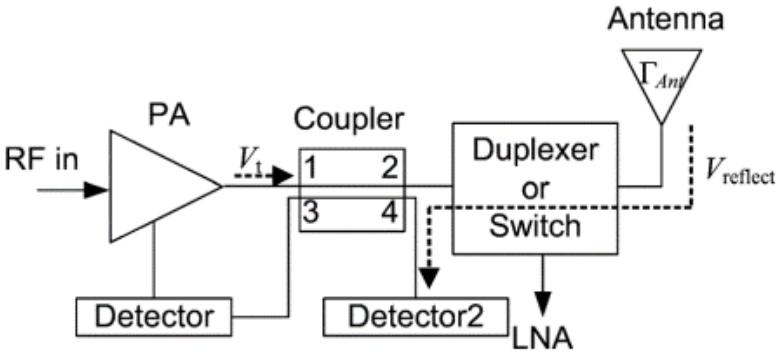

(c)

Figure 12: Vital sign detection system (adapted from [94]): (a) measurement setup of the proposed system; (b) photograph of the measurement setup with the antenna and the coupler; (c) details of the modified transceiver with a power sensor at Port 4

2.4.2.2 RFID Tag Antenna-Based Sensor

Following the success of RFID technology in many applications, a new trend of using the antenna of the RFID tag as a sensor has emerged in recent years [96-98]. In addition to its typical function as an identification tag, an RFID antenna can also be used as a sensor to the attached objects, based on the change in the antenna impedance. Many recent researches have employed this technique, mainly in structural health monitoring applications [96].

The attached object usually acts as a ground plane for the tag; hence, cracks [99] and strain [100] in the object surface or a change in the distance between the crack and the tag [101] leads to a shift in the tag resonant frequency, which can be picked by the reader. Figure 13 shows an example of crack detection, based on the change in the antenna reflection coefficient.

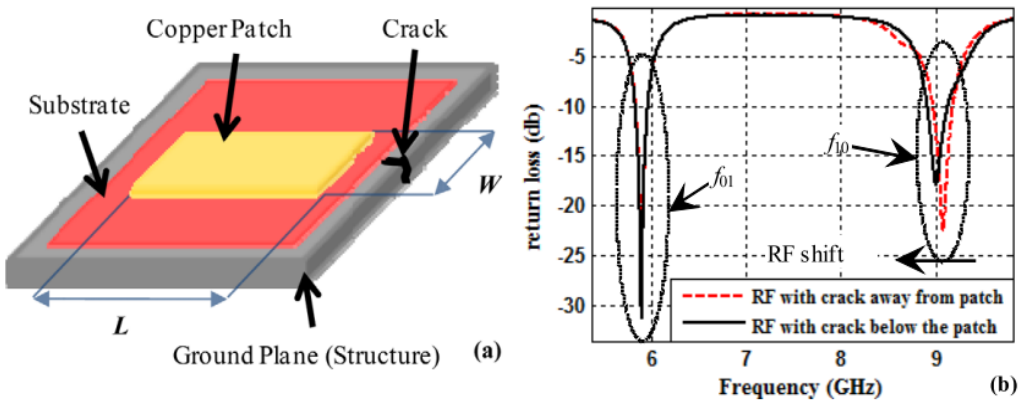

Figure 13: RFID Tag Antenna-Based Sensor (adapted from [99]): (a) patch antenna with a crack in its ground plane; (b) effect of a crack on S_{11} parameters of the patch

2.4.3 Related Work in Near-Field Sensing Using Specially Designed Antenna

The previous two subsections discussed related works that use low profile antennas and RFID tags as sensors for passive objects. These antennas and RFID tags are commercially available and widely used for wireless data transmission by many current wireless devices. One the other hand, this subsection review the related works that use specially designed antennas for near field sensing. The antennas in this case are meant to serve as RF sensors, but not for wireless data transmission.

2.4.3.1 Touchless Radar Sensor

Recently, Google announced a new project named Soli [102], which uses radar technology to detect the micro-motion of the human hand, thereby enabling a touchless interaction with wearable and other computer devices. According to their website, the Soli sensor can, with a high degree of accuracy, track sub-millimetre motions at high speed. The system can fit onto a chip; hence, it can be used inside even small wearable devices.

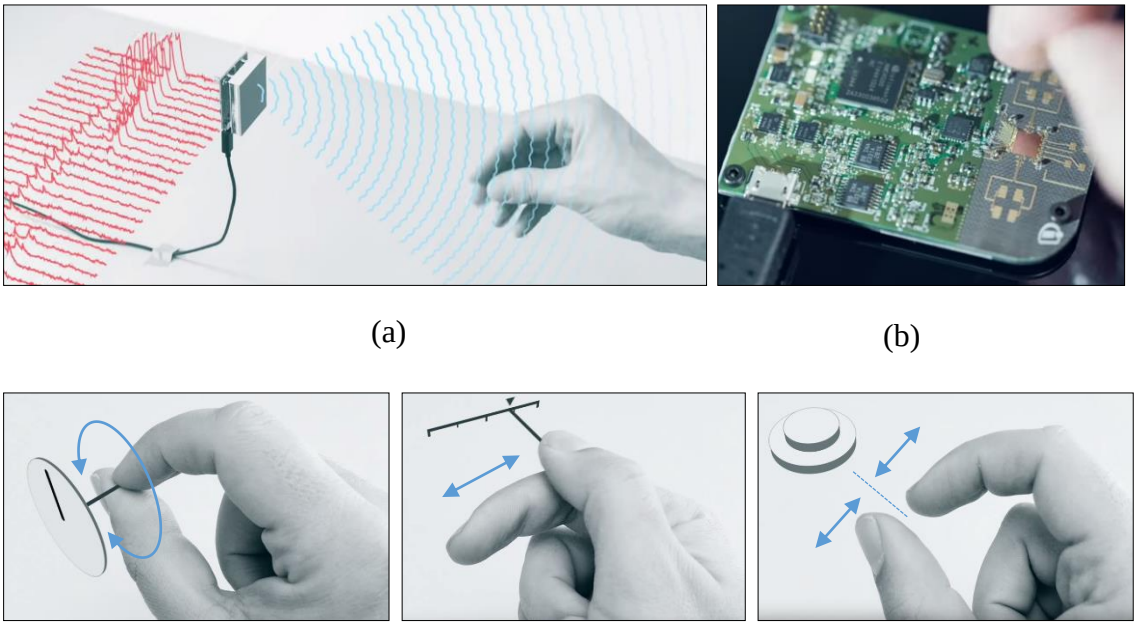

(a) (b)

(c)

Figure 14: Project Soli from Google (adapted from [102]): (a) illustration of the system concept; (b) radar-based gesture sensor; and (c) three examples of hand gestures corresponding to volume-roll, volume-slider and click-button, respectively

2.4.3.2 Wrist Pulse Detection

A novel wrist pulse sensor based on an electromagnetic near-field variation was presented in [103]. The design involves a compact resonator, shaped as a bracelet, and it is designed on a flexible substrate as an RF signal radiator, which can be worn on the wrist to measure a user's pulse. The slight changes in the radial artery diameter affect the distance between the wall of the major artery and the resonator; hence, they alter the reflection coefficient of the resonator. However, the system performance is highly affected by the tightness of the bracelet. Simulation results showed that the resonant frequency increases by more than 300MHz when the spacing between the bracelet and

the skin decreases to about 0.5 mm.

The system was designed to work at a 2.4-GHz ISM band. The experimental results showed that the system sensitivity is comparable to a conventional piezoelectric or photoplethysmography (PPG) sensor. Figure 15 (a) shows the system implementation, while Figure 15 (b) shows the sensor measurement compared to the reference measurement, using a piezoelectric sensor for finger pressure.

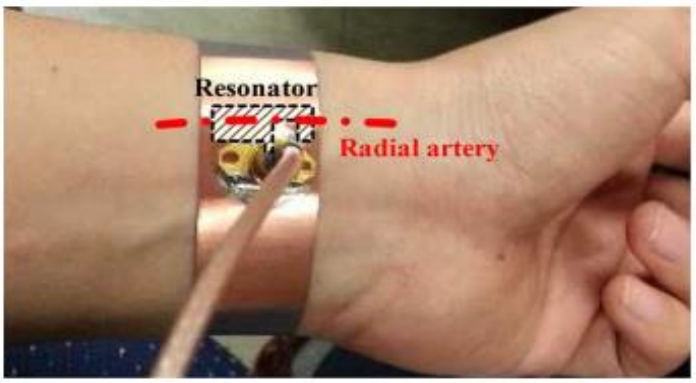

(a)

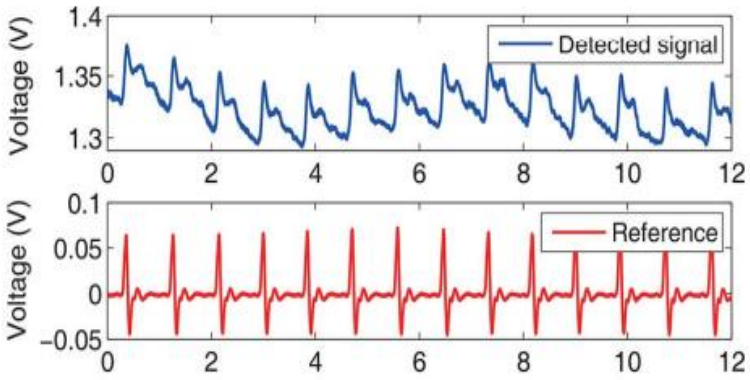

(b)

Figure 15: Wrist pulse detection (adapted from [103]): (a) photograph of the resonator implementation; (b) time domain data of the proposed system and piezoelectric reference

2.4.3.3 Pedestrian Protection Using Capacitive Sensor

A capacitive sensor for a pedestrian protection system in moving vehicles is presented by [104]. The system is proposed to reduce the severity of injuries in the case of an unavoidable frontal collision between a vehicle and a pedestrian. Although the system doesn't involve a wearable device, the design gives a good example of utilising the coupling between the human body and nearby objects to enhance the interaction between

environment's objects to the user. The proposed sensor involves placing a metallic sheet that emits an electric field inside the front bumper of a vehicle, in such a way that the emitted field is oriented towards the front of the vehicle. The interaction of the human body with the emitted field (as shown in Figure 16) induces a capacitive coupling with the sensor, which will enable the electronic device to detect the presence of the pedestrian. Laboratory-based results showed the system's ability to detect an intruder at a distance of 1 m when the vehicle speed is between 12 km/h and 72 km/h. Another suggested application for the sensor is for it to be employed in parking assistance, i.e., obstacle detection at the front and rear of the vehicle when the vehicle is moving at a very low speed.

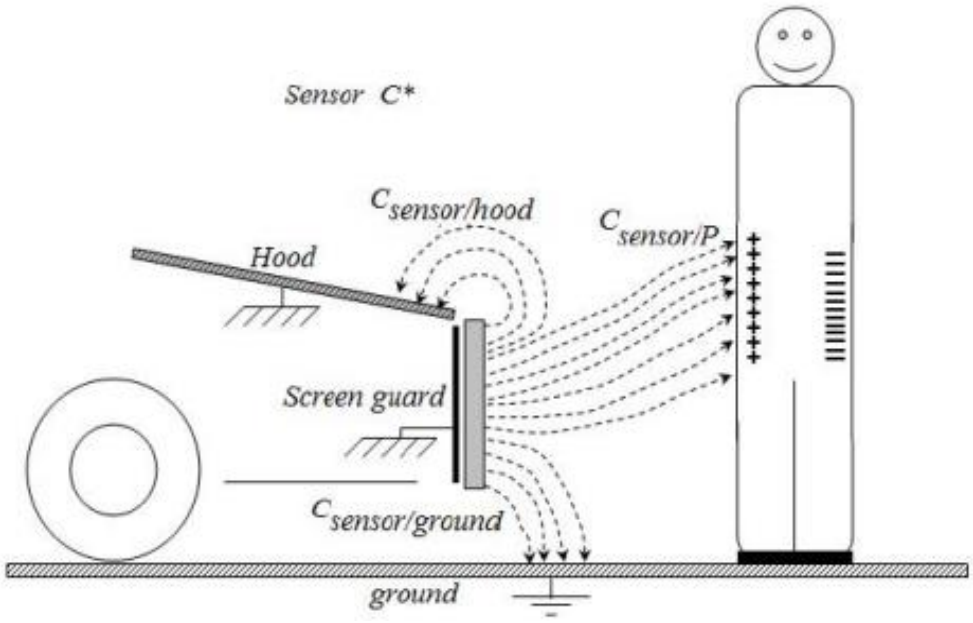

Figure 16: Capacitive coupling with a pedestrian in front of the capacitive sensor (adapted from [104])

2.5 Summary

This chapter presented a brief theoretical background on antenna measurements and WBAN concept and its protocols, followed by a review of related work. The literature review focused on the work that seeks, not merely to detect and compensate for the passive object interference on the RF transmission, but also to use the antenna as a sensor in addition to its traditional function in the communication process. The selected papers

in the review section were classified into three categories: far field sensing, near field sensing and near field sensing using specially designed antennas-like devices for the sensing process but not for wireless data transmission.

WBAN nodes attached to human body suffer from the continuous changes in the working environment, due to the normal activities of the human. This put node's antenna in frequent interaction with passive objects within the indoor environments and affect the WBAN communication. The challenge in applying previously mention solutions suggested by other authors, is that the WBAN antennas are, typically, designed to be less sensitive to theirs surrounding to reduce the coupling with human body. This obstruct the use of WBAN antenna as sensor for its surrounding. This leaves a gap for research in the area of antenna design and near field interaction with passive object, human body, and both as discussed by the next three chapters.

Chapter 3 Sensing Passive Objects in the Near Field of a Narrow Band Antenna

3.1 Chapter Outline

Many recent wireless networks depend on the RF signal strength to deduce or estimate certain measurements, for instance, wireless localisation and spectrum sensing applications. In wireless localisation, the network nodes estimate the distance between two adjacent nodes, based on the strength of the signals transmitted between them. As the distance between the nodes increases, the signal strength decreases. On the other hand, in spectrum sensing applications, the signal strength represents a basic mechanism to obtain awareness about spectrum usage and the existence of primary users in a nearby geographical area. Energy-based measurements are highly affected by other passive objects, especially items in indoor environments, such as walls, doors and furniture. These effects will cause inaccuracies in the measurements estimated from the signal strength, especially when the object is within the antenna near field.

This chapter presents a study of the effects of a metallic object placed within the near field of an antenna. Also, it proposes several schemes for the detection of the object and determines its distance using a commercially available, low profile, narrow band antenna. The layout of this chapter is detailed in Figure 17. In the following sections, two experimental setups are presented, whereby the object's effects are measured in terms of the reflection and transmission coefficients of two communicating antennas. The first setup, which focuses on the reflection coefficient, is presented in Section 3.2 and is followed by further analyses in Sections 3.3 and 3.4. The second setup, which discusses distance measurement using frequency sweeping, is presented in Section 3.5. Finally, Section 3.6 concludes the chapter.

3.2 Metallic Object Near a Single Antenna – Experiment I

To investigate the effect of metallic objects placed within an antenna near field on the antenna measurements (in term of S-parameters), an experimental setup was built, as shown in Figure 18. This section describes the experimental setup and discusses the results. Further analyses of the results are presented in Sections 3.3 and 3.4.

3.2.1 Test Setup of the Narrow Band Antenna with a Metallic Object

The experiments were conducted inside an anechoic chamber of steel construction that measures 2.5 m × 2.5 m × 2.5 m; the internal ground, ceiling and walls are clad with a foam absorber material.

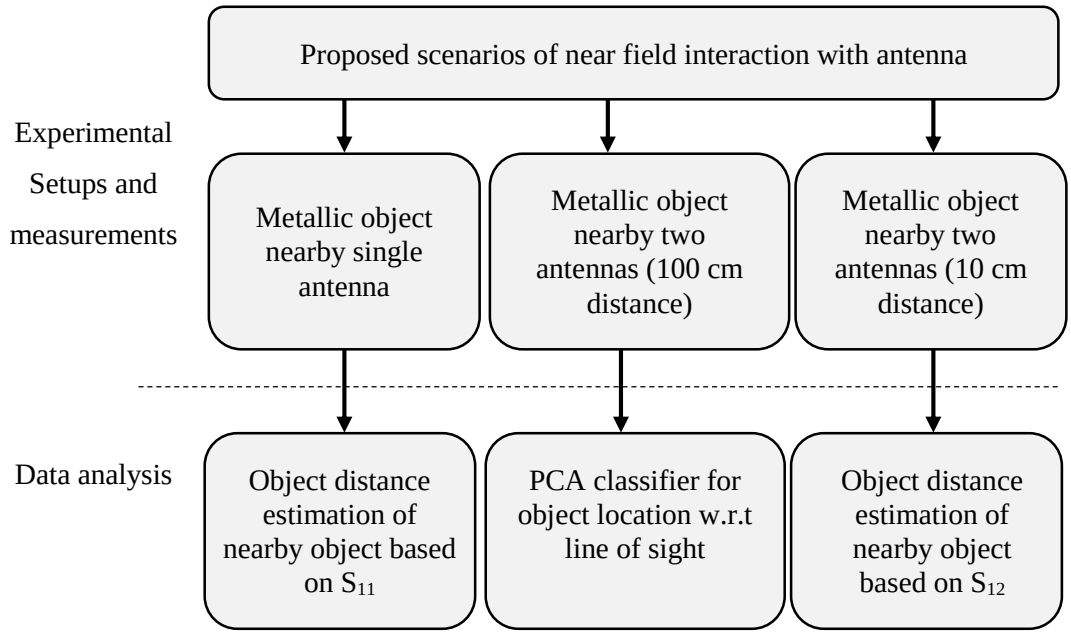

Figure 17: Chapter-3 layout

Two omnidirectional, 2.4-GHz quarter-wave dipole antennas were used, which are commercially available for WLAN applications that work in the 2.4-GHz ISM band. Each antennas has vertical polarisation, and its gain is 2.0 dBi. The two antennas, named *Antenna#1* and *Antenna#2*, were vertically fixed, using a plastic stand on a wooden stool, with a distance of 2.25 m between them and 1 m above the chamber floor, as shown in Figure 19. The effect of the wooden stool and the plastic stand was ignored, as the location of the metallic object was the only variable that was changed in each experimental setup. S-parameters were measured and recorded for both antennas, using a 2-Port network analyser (Agilent-8363B). The network analyser was set to work in the frequency range from 2 GHz to 3 GHz with 5 MHz steps; hence, each response consists of 201 frequency steps. Although this range is 10 times larger than the antenna bandwidth, it was selected to enable a comprehensive view of the changes in antenna measurements.

A plate of iron with dimensions 30×20×0.3 cm^3 (shown in Figure 18) was used as the metallic object. The plate thickness is several order of magnitude greater than material skin depth (calculated in Section 2.2.4). Hence, the amount of the electromagnetic wave that penetrates the plate at this frequency band is insignificant and most of the incident signal will reflect upon the plate surface. Non-metallic objects have no or very little effect on antennas within the near field. For the purpose of this experiment, a flat metallic plate with a clear surface was chosen. The object length and width were selected to be larger than the antenna length to reduce the likelihood of signal diffraction due to the object's edges affecting the results. Object thickness, on the other hand, doesn't affect the results, considering that the mutual coupling is actually happening between the antenna and its

image on the metallic surface. Hence, the experimental results will be valid for larger objects, as long as they have a nearly flat surface facing the used antenna. A top view of the setup layout is shown in Figure 19.The plate was placed in three positions relative to the two antennas, and they were named *p1*, *p2* and *p3*, as follows:

a) Position *p1*: The plate is placed behind *Antenna#1*, along the line of sight (LOS) between the two antennas. The plate works mainly as a reflector for the transmitted/received signal by *Antenna#1*.
b) Position *p2:* The plate is placed on the left side of the second antenna, beside *Antenna#1* at 90^0 relative to the LOS.
c) Position *p3*: The plate is placed on the LOS between the two antennas, yet it is closer to *Antenna#1*. The plate shadows the transmitted signal between the two antennas.

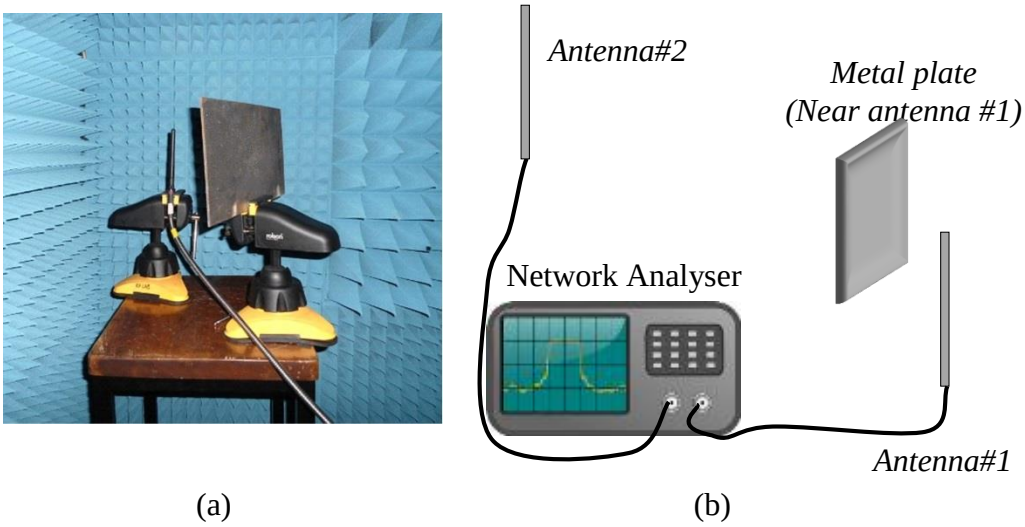

Figure 18: Experiment setup: (a) antenna and metal object picture; (b) setup illustration

Only one side position was considered, since the other side (to the right of *Antenna#1*) would be symmetrical with respect to the LOS. Also, other positions where the metal plate is above or below the antenna were not considered, because the antenna has different radiation patterns along the XZ- and XY-planes.

At each position, the plate was fixed vertically, facing the antenna. The distance between the plate and the antenna (*d*) was changed from 1 cm to 25 cm, by moving the plate away from the antenna by increments of 1 cm. In the experiment, distances between 1 cm and 25 cm were considered in order to include the near field and radiated near-field

areas.

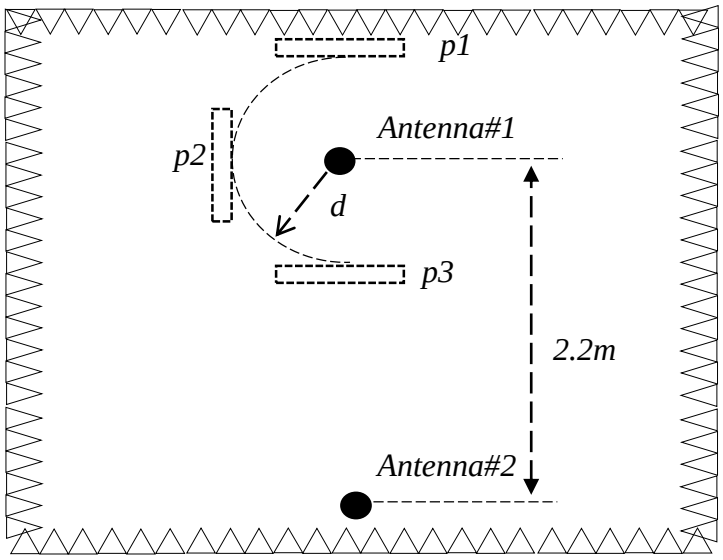

Figure 19: Setup layout (top view) shows the positions of the plate and the antennas

3.2.2 Results of S-parameters Change with Distance

The s-parameters, generated using the network analyser for the two antennas, consist of: S_{11}, S_{21}, S_{12} and S_{22}. Each one of them is a complex value (magnitude and phase). However, in the discussion below, only the magnitude values of the S_{11} and S_{12} parameters are considered. The parameters S_{11} and S_{12} correspond to the reflection coefficient and transmission coefficient, respectively, at *Antenna#1*. Since *Antenna#2* is relatively far (more than 2 meters) away from the metal plate, the plate has little or no effect on the S_{22} value. Similarly, the transmission coefficients S_{21} and S_{12} are identical, even when the object was introduced, due to transmission reciprocity [42]. At first, the S-parameters were recorded without the presence of a metal plate. Then the metallic object was introduced at several locations.

Figure 20 shows the magnitude of S_{11} and S_{12} before the metal object was placed. Since the test used a narrow band antenna, the minimum value of S_{11} was between 2.4GHz and 2.5GHz, as expected, while S_{12} shows the maximum value in this frequency range. The magnitude of S_{12} in this region depends mainly on the antenna gain and the distance between the two antennas. Figure 21 shows the magnitudes of S_{11} and S_{12} at position *p1* as functions of distance *d* and frequency. Similarly, Figure 22 and Figure 23 show the results for positions *p2* and *p3*, respectively. For more clarification, additional results are presented in Figure 24, in 2D form, for selected instances of distance *d*.

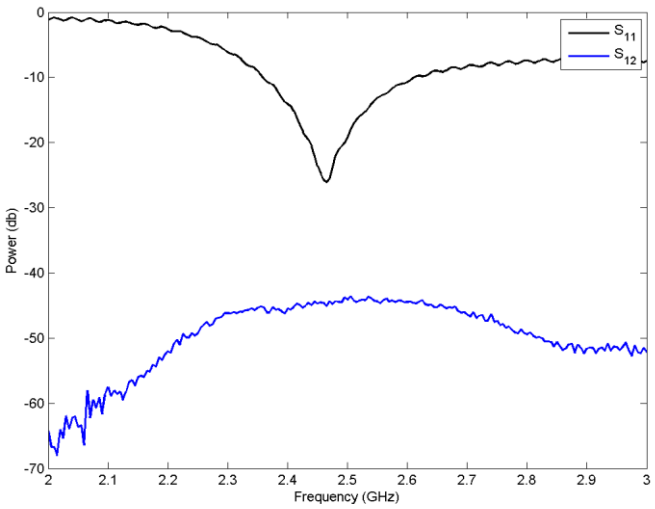

Figure 20: S_{11} and S_{12} magnitudes (when no metal plate is used)

The effects on the S_{12} magnitude range from a frequency-selected attenuation when the object is at position *p1*, to severe shadowing for small distances at position *p3*, as explained below:

a) At position *p1*, the metallic plate acteds as a reflector behind *Antenna#1*. Hence, *Antenna#1* received two copies of the transmitted signal from *Antenna#2*, the LOS component and the NLOS component (reflected from the plate). The interference between these two components appears as a frequency-dependent interference on the *Antenna#1* side. As the distance *d* increases, the response shows constructive and destructive interferences for different distance values. The difference between the constructive and destructive interferences is about 20 dB, and the distance between two consecutive peaks is about 6 cm.

b) At position *p2*, the metallic plate is still acting as a reflector, but the interference is less than that of *p1*. The distance between two consecutive peaks is about 15 cm in distance and 10 dB in value.

c) At position *p3*, the metal plate blocks the transmitted signal and causes a severe reduction in transmitted power (≈20db) in the first 5cm, as well as a high fluctuation in the S_{12} value. As the metal plate was moved away from the antenna, the S_{12} value increased and tend to be steady. For distances greater than 20cm, the effect vanishes and the value settles on its free space magnitude as shown in Figure 23 (a). Although the metallic plate is still inside the Fresnel Zone, the excess path loss (caused by sharp edge interference) is not noticeable.

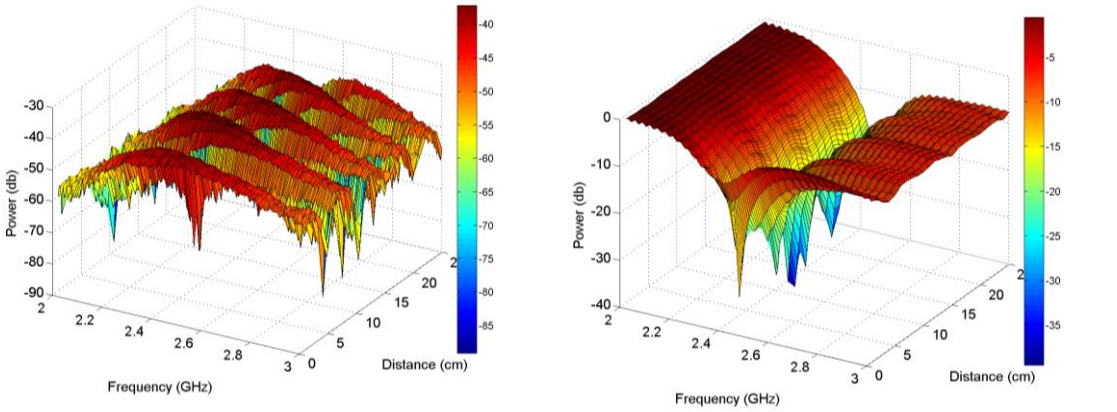

(a) (b)

Figure 21: Magnitude of S-parameter at position *p1*: (a) S_{12} and (b) S_{11}

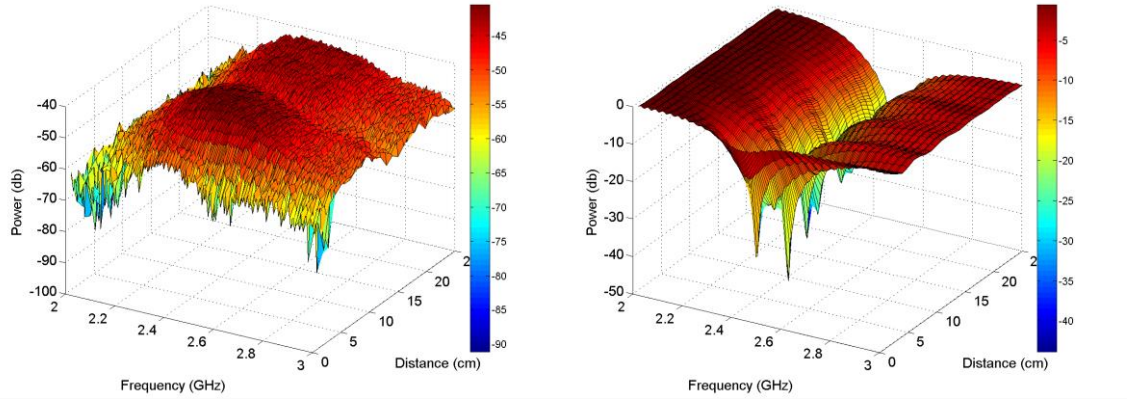

(a) (b)

Figure 22: Magnitude of S-parameter at position *p2*: (a) S_{12} and (b) S_{11}

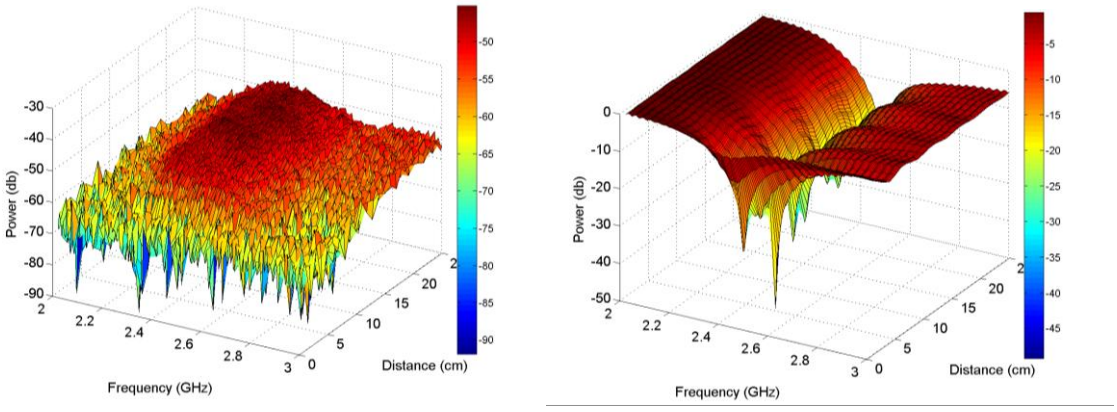

(a) (b)

Figure 23: Magnitude of S-parameter at position *p3*: (a) S_{12} and (b) S_{11}

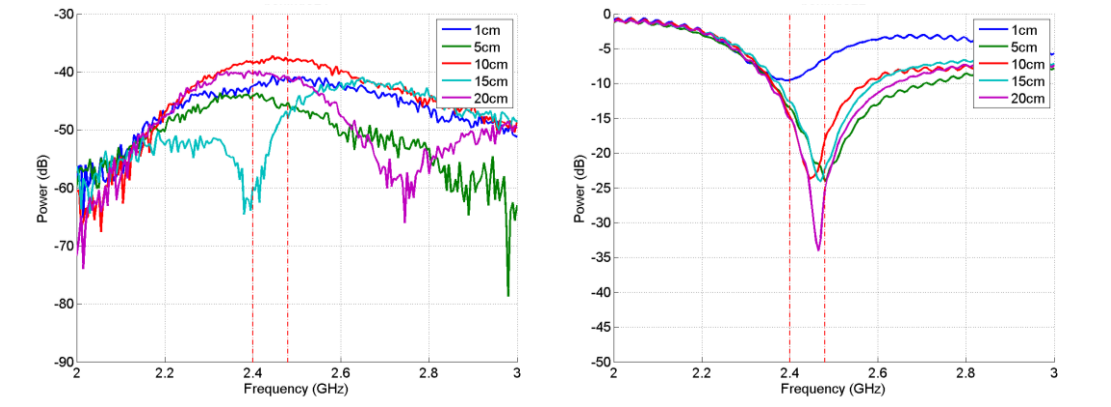

(a)

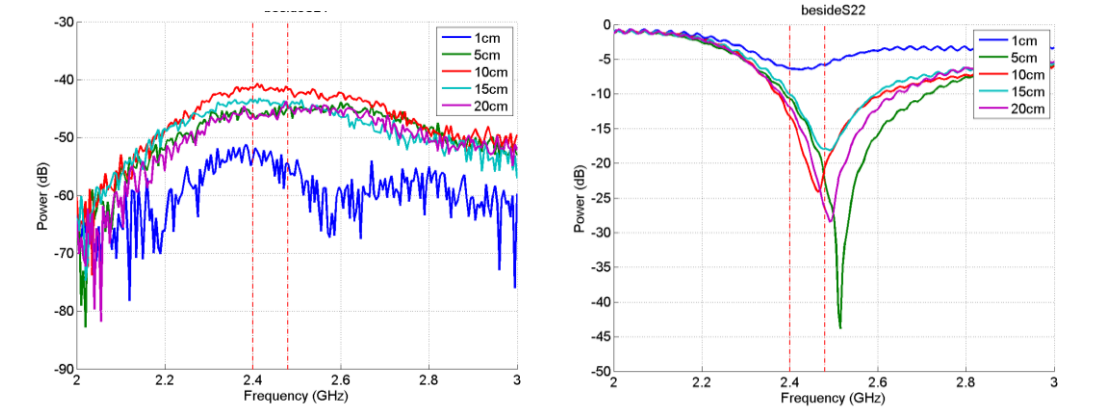

(b)

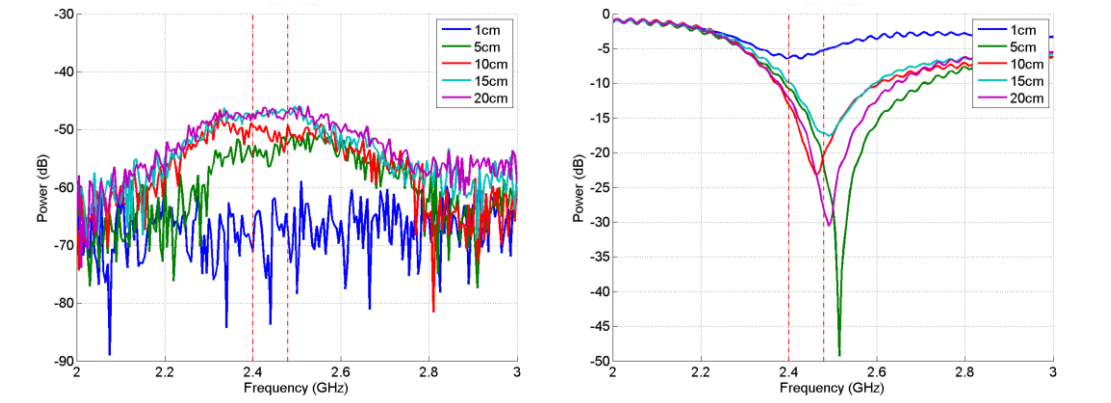

(c)

Figure 24: S_{12} (left) and S_{11} (right) at selected distances for three positions: (a) *p1*, (b) *p2* and (c) *p3* (the two vertical red lines represent the 2.4-GHz ISM band boundaries)

For S_{11}, the effects of the metallic object on the three positions are identical, except for slight changes (<1 dB) due to setup differences. This is because the antenna used in the experiment is omnidirectional in the H-plane. For small distances ($d < 5$ cm), the antenna is unable to transmit correctly, due to high coupling between the antenna and the metallic object, which makes the reflection coefficient above -10dB. For greater distances ($d \geq 5$ cm), the response of S_{11} at resonant frequency drops below -10dB. As the distance *d* increases, both the minimum value of the S_{11} response and its corresponding resonant frequency are affected. A further analysis of the S_{11} response is presented in the following section.

3.3 Detection of the Plate Distance to the Antenna, Based on the Reflection Coefficient

The results in the previous section showed that placing a metallic object near an antenna at distance *d* affects the antenna reflection coefficient, regardless of the object location with respect to the LOS between the two antennas. As the distance *d* changes, the antenna resonant frequency is shifted and the antenna reflection coefficient value is changed. By analysing these two parameters, an object's presence can be sensed, along with its relative distance to the antenna. Hence, this section investigates the ability of a single antenna to detect a metallic object's existence within the near field and estimate *d*, based solely on the reflection coefficient.

To validate the experimental results of the reflection coefficient presented in the previous section, a similar setup was modelled in simulation, and the results were compared. Also, the simulation investigated the effect of the metallic plate dimensions on the results; this consideration was not explored in the experimental setup. The simulation was performed in CST Microwave Studio [105], using a Time Domain Solver.

In the next subsections, the simulation model is explained in detail, with a comparison to the experimental results. Then, an analysis of the relation between distance *d* and the change in the reflection coefficient is presented.

3.3.1 Validation of Results Using CST-Software

A simulation was performed using CST Microwave Studio Suit [105]. In the simulation, an antenna was modelled with a metallic plate in the antenna near field. The antenna is a half-wave dipole antenna, designed to work in the 2.4-GHz ISM band. The plate dimensions and material are set to match the one used in the experimental setup.

Figure 25 depicts the simulation model, while the simulation specifications are listed in Table 1. The simulation was repeated three times; at each time, a different variable was swept, as shown in Table 2, and in each case, the S_{11} antenna was measured and plotted. The minimum values of the S_{11} and antenna resonant frequency were then plotted against each variable as follows:

a) In the first run, variable *d*, defined as the distance between the antenna and the metal plate, was swept from 2 cm to 50 cm, in 2 cm increments. The simulation results for this run are shown in Figure 26.
b) In the second run, variable *T*, defined as the metallic plate thickness, was swept from 0.3 cm to 3 cm in steps of 0.3cm. The simulation results for this run are shown in Figure 27.
c) Finally, variable *X*, defined as the plate length/width, was swept from 2 cm to 30 cm, with 2 cm increment. The simulation results for this run are shown in Figure 28.

Table 1: Simulation specifications

	Name	*Value*
Antenna		
	Radius	0.014778 cm
	Length	5.44 cm
	Feeding Gap	0.03522 cm
	Material	Copper, $\sigma=5.8*10^7$ (S/m)
Plate		
	Thickness	0.3 cm
	Dimensions	$X \times X \times T$
	Material	Iron, $\sigma=1.04*10^7$ (S/m)
Mesh property		
	Line per wavelength	20
	Lower mesh limit	15
	Mesh line ratio limit	10

Table 2: Simulation run parameters

run	*Distance d*	*Thickness T*	*Dimension X*
#1	Variable: 2 cm to 50 cm	0.3 cm	20 cm
#2	2.5 cm	Variable: 0.3 cm to 3 cm	20 cm
#3	5 cm	0.3 cm	Variable: 2 cm to 30 cm

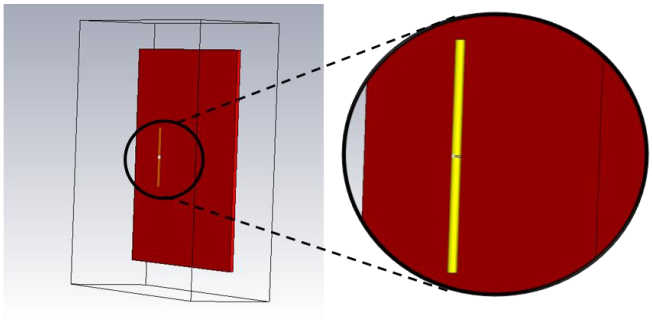

Figure 25: Dipole antenna and metal plate simulation model

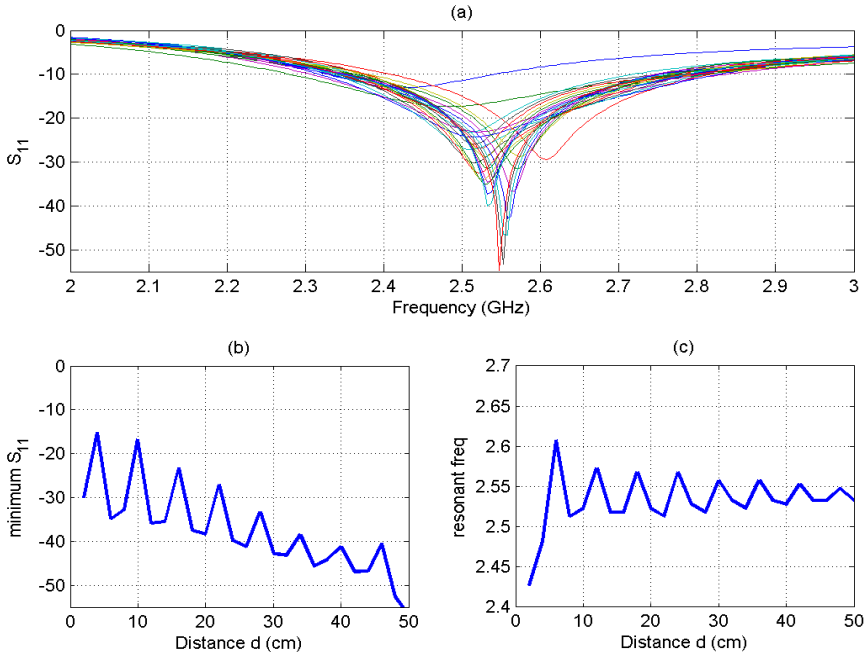

Figure 26: Antenna reflection coefficient vs. distance *d* (simulation run #1): (a) S_{11} response; (b) minimum value of each response; and (c) antenna resonant frequency of each response

Figure 26 (a) shows the accumulated responses of the reflection coefficient for all values of *d.* To understand the effect of changing distance *d* on the response, two parameters were observed: *antenna return loss* (R_{min}), defined as the minimum value of the reflection coefficient response, and *antenna resonant frequency* (F_{res}), defined as the frequency at which R_{min} occurs.

Each one of these two parameters was plotted as a function of *d*, as shown in Figure 26 (b) and Figure 26 (c), respectively. The figures show that F_{res} oscillates up and down in frequency range and R_{min} oscillates up and down the free space value. The oscillation starts at higher value for small *d* values and diminishes as *d* increases.

The second simulation run showed that changing the metallic plate dimensions causes

minor effects on the reflection coefficient response. Figure 27 (a) shows the reflection coefficient for several values of *T*. The return loss change is within 2 dB, and the changes in resonant frequency are less than 10Hz, as shown in Figure 27 (b) and Figure 27 (c). It is worth mentioning that, in this case, *d* is set to 2.5 cm; hence, both R_{min} and F_{res} have shifted from their initial values. On the other hand, changing the plate length/width can be viewed in three distinct ranges, with respect to the antenna's electrical length, which is approximately 3 cm. These regions are:

a) When *X* is greater than 3 cm, the change in *X* has a small effect on the response. Again, in this case, *d*=5 cm; hence, both R_{min} and F_{res} have shifted from their initial values.
b) When *X* is less than 3 cm, the R_{min} value drops below -50dB, while F_{res} is the same as it is for the larger values of X.
c) When *X* is approximately 3 cm, the R_{min} value drops to -40dB and F_{res} shifts to less than 2.4Gz.

In other words, the plate dimension shows a minor effect on the reflection coefficient, except when the object dimension is approximately equal to the antenna's electrical length, which causes a large shift in both the R_{min} and F_{res} values. Also, for a plate dimension less than 3 cm, there is large change in R_{min}, while F_{res} is not affected.

This case can be explained by comparing the setup to an array antenna and particularly Yagi-Uda antenna. In Yagi-Uda antenna the parasitic elements longer than the driver antenna have inductive impedance while shorter parasitic elements have capacitive impedance [42]. When the length of the parasitic element (the metallic plate in this setup) is the same as the driver antenna length, its impedance is reduced to pure resistive which cause the drop in the antenna return loss and the shift in its resonant frequency.

Finally, the simulation and experimental results of selected values of *d* are plotted in Figure 29. Despite the slight difference between the two sets of results, both of them clearly show a similar pattern of change in R_{min} and F_{res}, with respect to distance *d*. In conclusion, the simulation validated the experimental results and showed that, for a plate dimension larger than the antenna size, the distance *d* is the dominant factor that affects the antenna reflection coefficient. Hence, the next section analyses the relation between the reflection coefficient and distance *d*, based on the experimental results.

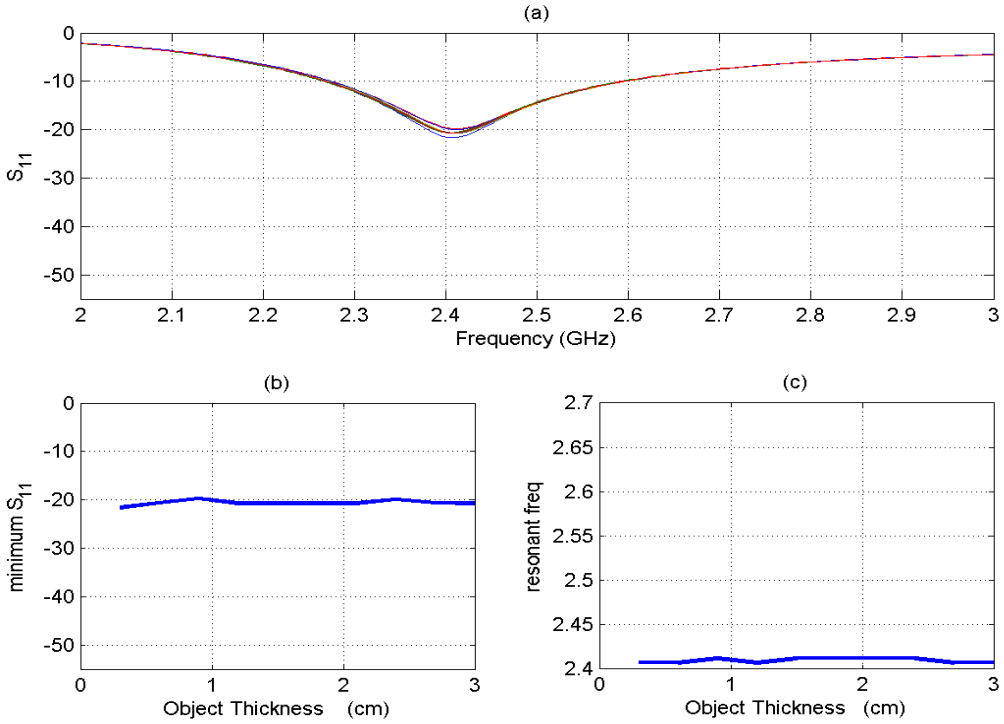

Figure 27: Antenna reflection coefficient vs. plate thickness (simulation run #2): (a) S_{11} response; (b) minimum value of each response; and (c) antenna resonant frequency of each response

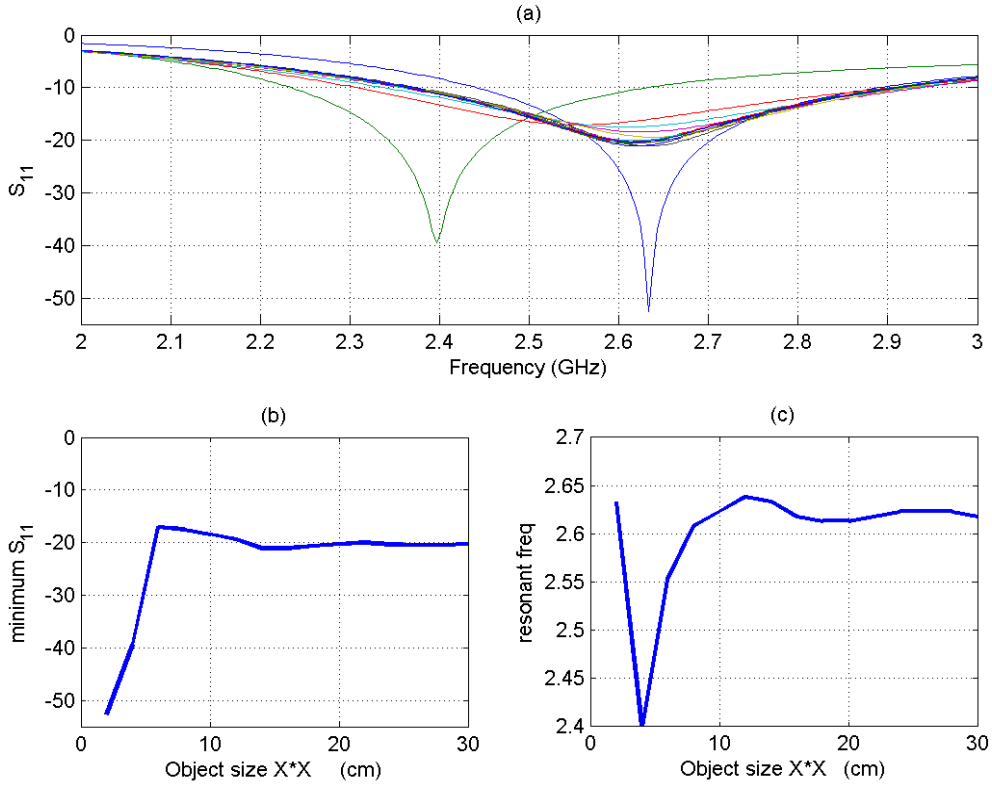

Figure 28: Antenna reflection coefficient vs. plate length (simulation run #3): (a) S_{11} response; (b) minimum value of each response; and (c) antenna resonant frequency of each response

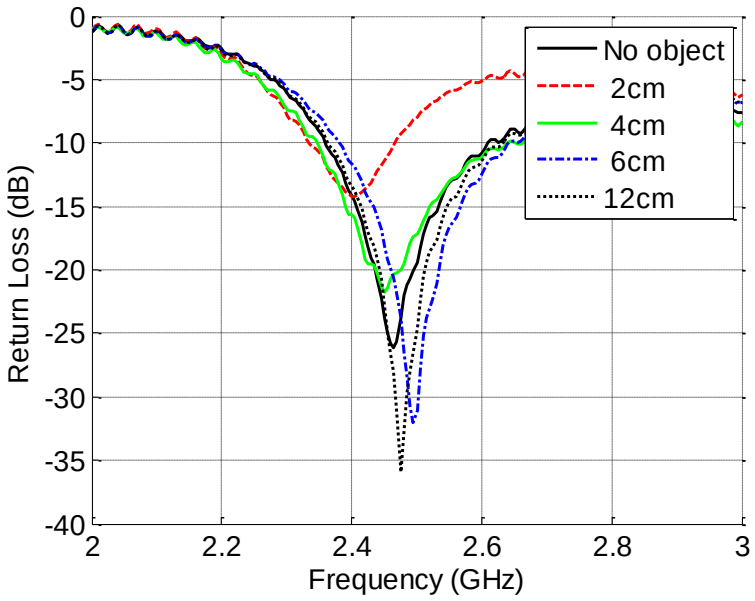

(a)

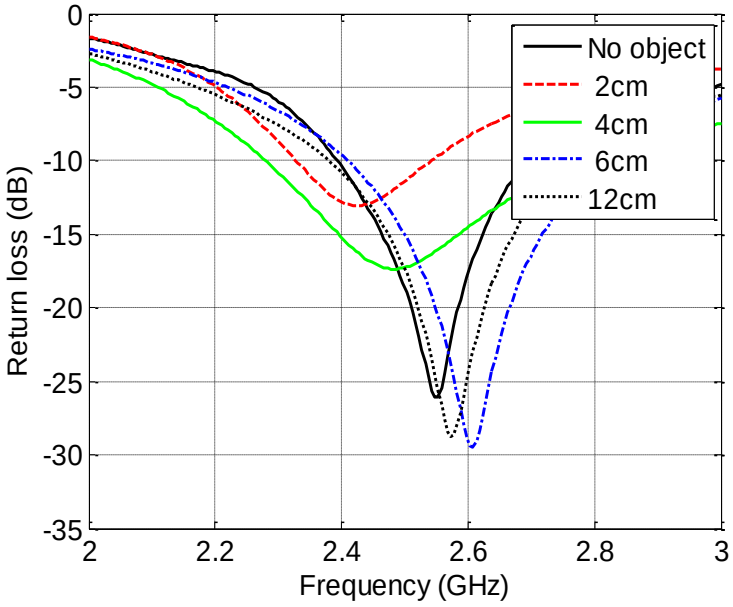

(b)

Figure 29: Reflection coefficient magnitude for selected values of *d*: (a) measured and (b) simulation

3.3.2 Distance Estimation Based on Changes in S_{11} Magnitude

The antenna reflection coefficient is highly affected by coupling with nearby metallic objects. This effect depends on the object's size, shape, material and coupling distance. As shown in previous sections, the effects of object size and shape are insignificant, for relatively large objects compared to a low profile antenna. It is worth mentioning that the

reflection coefficient is also affected by the change in environmental conditions, such as temperature, yet these changes are trivial within this context. Thus, a direct function can be determined, one that relates the reflection coefficient value to the coupling distance, regardless of the object location around the omnidirectional antenna. Within the current experimental setup results, the effects of the object's material on the reflection coefficient are not considered. Conversely, the results show a clear relation between the reflection coefficient and object location within a distance of a few wavelengths from the antenna, as shown in Figure 29. This relation is characterised by two parameters: the antenna resonant frequency F_{res} (which corresponds to the lowest value in the reflection coefficient response) and the value of the reflection coefficient at this frequency, R_{min}. When the object was placed at distance *d* from the antenna, these values shifted slightly to new values, F_{res}^{d} and R_{min}^{d}. When the object is removed or placed outside an antenna near field, these parameters settle on their initial condition values, R_{min}^{∞} and F_{res}^{∞}.

Changes in F_{res}^{d} and R_{min}^{d} as functions of the coupling distance are shown in Figure 30. For Figure 30 (a), the value of F_{res}^{d} is found to be shifting up and down the antenna resonant at free space (which is 2.46 GHz) as the coupling distance changes. This change is within ± 50 MHz in the first 5 cm, then it decreases to ±20MHz from 5 cm to 15 cm. After 20 cm, it becomes less than ±10 MHz. Similarly, Figure 30 (b) shows that R_{min}^{n} shifts up and down R_{min}^{∞}, which is ≈ -26 dB as the distance changes. When the coupling distance is less than 5cm, the change in R_{min}^{d} value is within ±30 dB, and it decreases to ±10 dB in the next 10cm, then become less than ±5 dB after 20 cm. As discussed in previous section, the near field is bound to a few wavelengths, hnece for a 2.4-GHz band the near field radius is about 12 cm. Notice that F_{res} settled to its initial value at 25cm, while the effect on R_{min} is within 2 dB; hence, the total effect is expected to diminish around 30cm.

Since both parameters oscillate around initial values, the change in each parameter reaches zero at some distances. Hence, it is not possible to use either one of them as indicators of object existence, which is also confirmed by simulation results. However, it is worth noticing that changes in these two parameters are out of phase as shown in Figure 30 (d). The net change, Z_d at a specific distance *d* can be represented by using Pythagorean Theorem, as follows:

$$Z_d = \sqrt{a\left\| F_{res}^{d} - F_{min}^{\infty} \right\|^2 + b\left\| R_{res}^{d} - R_{min}^{\infty} \right\|^2}\ , \qquad (29)$$

where *a* and *b* are generic parameters used to tune the sensitivity of the antenna to F_{res}^{d} and F_{min}^{d}. For the current setup, Z_d is calculated as

$$Z_d = \sqrt{0.5 * \left\| F_{res}^{d} - 2.48Ghz \right\|^2 + \left\| R_{res}^{d} - (-25dB) \right\|^2}. \qquad (30)$$

Figure 30 (d) shows the calculated values of Z_d with distance, using (30). Although the Z_d response hasn't shown a proportional or monotonic relation with distance, the response can be divided into three distinct regions: (a) Z_d > 20 in the first 3cm, (b) 3<Z_d <13 between 5cm and 15cm, and (c) Z_d <5 approximately, for distances larger than 13cm. Therefore, Z_d gives an approximate indication of object existence with a dipole antenna near-field area.

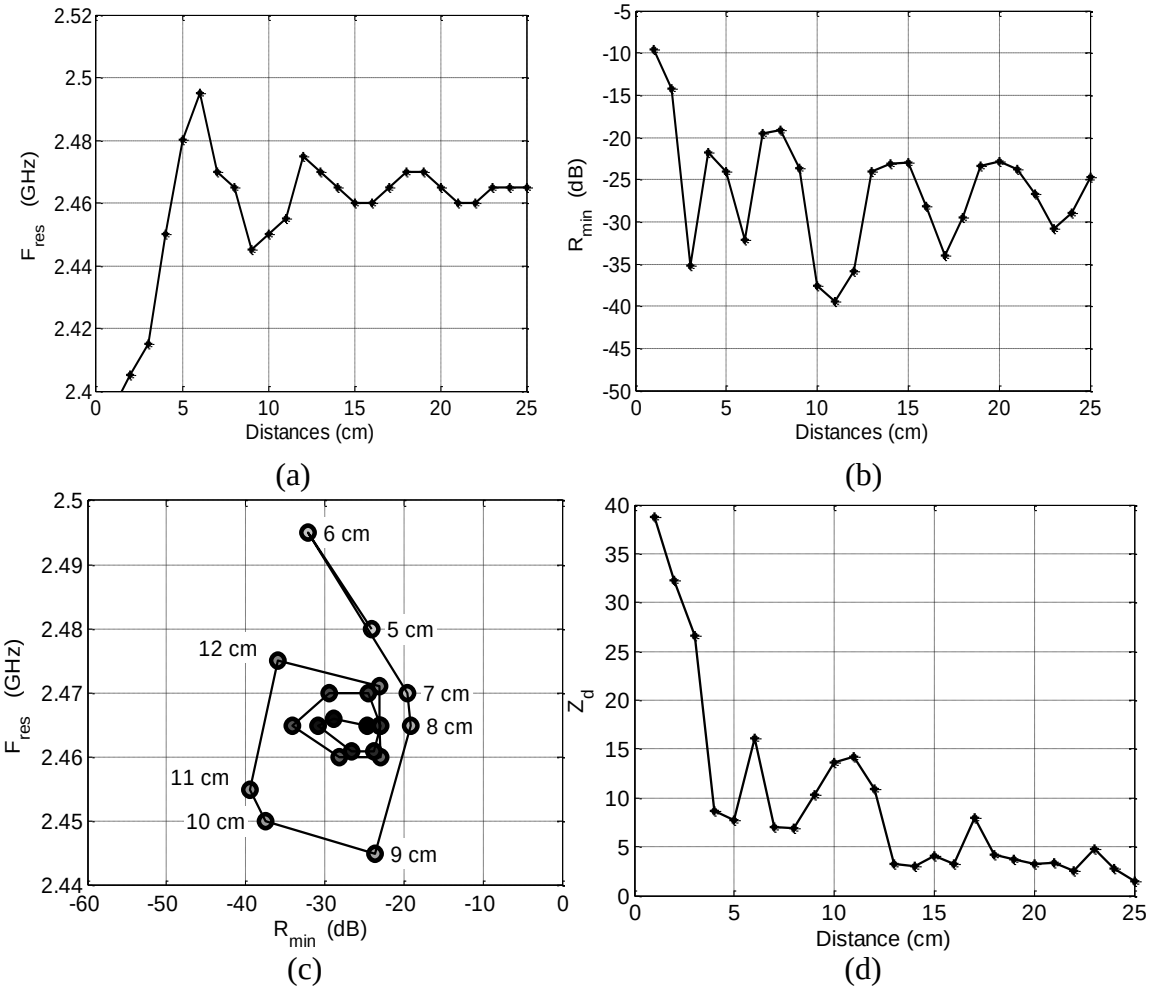

Figure 30: Change with distance: (a) F_{res} vs distance, (b) R_{min} vs distance, (c) F_{res} vs R_{min} and (d) Z_d vs distance

3.4 Object Location Classification Using Principal Component Analysis

From the previous section, it was concluded that it is possible to specify the approximate distance between an antenna and a metallic object placed within the near field, based on the antenna reflection coefficient. In this section, another step was taken to classify the object location with respect to the LOS between two communicating antennas, using principal component analysis (PCA). The classifier was applied to distinguish between the measurements from the three positions shown in Figure 19. The classifier uses the reflection coefficient response (magnitude and phase), as well as the transmission coefficient (magnitude and phase).

In the subsections below, a brief description of the PCA method is presented, then the classification approaches and results are discussed in detail. In the third section a study of the results statistical significance is presented.

3.4.1 Principal Component Analysis (PCA) Classifier

Principal Component Analysis (PCA) provides an advanced mathematical procedure to analyse data in multi-dimensional variable space and reflect data into lower dimensional space. It is mathematically defined as an orthogonal linear transformation that transforms the data to a new coordinate system such that the greatest variance by some projection of the data comes to lie on the first coordinate (called the first principal component), the second greatest variance lies on the second coordinate and so on. A simplified background on the method and the used MATLAB code are presented in Appendix A. For more details on the PCA classification, a quick tutorial is presented in [106], while [107] provides an extensive guide of the method and its applications.

3.4.2 Classification Methodology and Results

To apply the PCA, the data should be arranged in an $n \times m$ matrix, where n is the number of observations and m is the number of variables. The analysis in this section uses the experimental measurements obtained in Section 3.2. The PCA classifier was applied twice, each time with a different approach, depending on the way the data was organised. The results of the two approaches are shown in Figure 31 and Figure 32.

In the first approach, the experimental measurements were arranged as 79 measurements (observations). The first 75 observations represents measurements for the 75 locations in the experiment, which are based recorded at 3 positions: *p1*, *p2* and *p3*. At

each position, 25 distance steps were taken. The last 4 measurements were taken without the metal plate (non-metal). Each observation involves the aggregated frequency responses of the S_{11} magnitude, S_{11} phase, S_{12} magnitude and S_{12} phase in a single vector, representing the variables. As previously described, each frequency contains 201 steps, from 2 GHz to 3 GHz; hence, each observation contains 4 × 201 variables. The dimensions of the data matrix is 79 × 804.

Figure 31 shows the classification of the object location, based on the first two principal components, PC1 and PC2. Each marker (dot) in the figure represents a single observation, recorded when the object is placed at a different location. The marker's shape represents one of the three positions, while the marker size represents the plate's distance to the antenna; the larger dot size corresponds to a larger distance. For no-metal case the marker are of the same size.

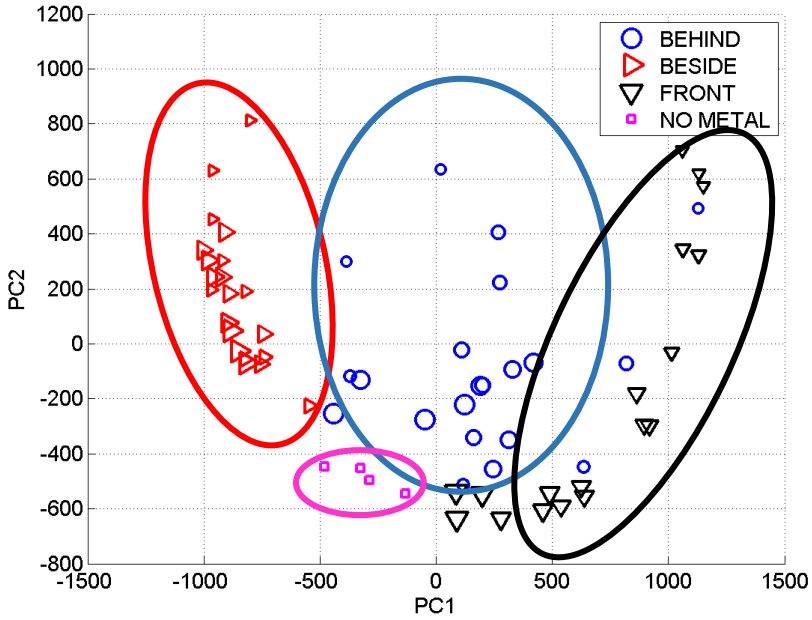

Figure 31: PCA classification for plate location, using S-parameters (for clarity, only distances larger than 5 cm are plotted)

The small markers in the figure in the upper middle (○), upper left (▷) and upper right (∇) sections clearly show a classification between the observations measured with small values of *d* at positions *p1*, *p2* and *p3*, respectively, while the non-metal observation corresponds to the square markers at the bottom (□). As the plate moves away from the antenna, its effect on the antenna diminishes; hence, the markers come closer to the

regions that represent the non-metal case. For large values of *d*, all of the markers settle on the bottom, and the classifier is unable to be clearly distinguished between the observations.

Since the PCA is a feature selection method, a second approach for classification was implemented using selected features of the same data sets. The responses of S_{11} and S_{12} were processed to produce five features, as listed in Table 3. The five features were calculated for each distance step and position in the previous setup. Hence, the dimension of the data matrix to be classified was 79 × 5, where each feature represents a variable. The aim of this approach is to find the features are most effective to be used as indicator for the object location and distance. However, the observations of position *p1* and *p3* are not clearly classified in this approach. Figure 32 shows the results of using PCA with the selected features. It can be seen that Features 3 and 5 are better than the other features in terms of distinguishing between the results (other features are appearing closer to the figure's origin, and their labels were removed for clarity).

Table 3: Features and their calculations

Feature name	*Feature Calculation*
Feature 1	Mean value of S_{12} magnitude response
Feature 2	Mean value of S_{12} phase response
Feature 3	R_{min}
Feature 4	F_{res}
Feature 5	Peak-to-peak of S_{11} phase response

In conclusion, Figure 31 shows that the PCA method have the potential to distinguish between different changes in antenna measurements due to different object locations around the antenna, while Figure 32 shows that among the proposed features, antenna return loss and Peak-to-peak of S_{11} phase are the most useful to detect the object location and distance.

To quantity the group classification showed in Figure 31, the results should be proven statistically significant. One way to prove that is by calculating the F-ratio of observed data (sample data set) and compare it to the f-distribution of the population data set. Since the population data set is unknown, its distribution can be approximated by statistical methods such as Bootstrap method and permutation test [108]. The statistical significance of the results is presented in the next section.

3.4.3 Statistical Significance of PCA Results

This section present the statistical significance calculation using permutation test. Permutation tests are used for nonparametric hypothesis testing. The objective of permutation tests is to determine whether an observed statistic deviates significantly from its null distribution, which is established conditionally on the data, and does not require a particular probability model. This characteristic of the permutation procedure matches the nonparametric nature of PCA, which makes the procedure suitable for inference in PCA. To establish a null distribution, first, the correlational structure of the observed data is destroyed by randomly rearranging the values within each variable (independent of the other variables). In this way, a data matrix of the same size as the original data matrix is constructed, with a random structure [108].

The statistical significance calculation on the PCA results shown in fig are explained in the next steps:

1. Define the null hypothesis:

$$H_0: \mu_{front} = \mu_{beside} = \mu_{behind} = \mu_{no\ metal} \ , \tag{31}$$

   or in other word: *PC1 and PC2 do not distinguish between the different observations.*
2. Specify the level of significance (α): Here it was set to the default value 0.05.
3. Select suitable number to repeat the permutation process:
   The minimum number of permutation is related to the significance level as follow:

$$min_{perm} = \frac{1}{\alpha} = \frac{1}{0.05} = 20. \tag{32}$$

   The maximum number of permutation is bounded by the number of possible ways to rearrange the observations while keeping the same number of groups and the same number of elements in each group. It is calculated as follow:

$$max_{perm} = \frac{(n_1 + n_2 + \ ... + \ n_n)!}{n_1!\, n_2! \ldots n_n!} \ , \tag{33}$$

where n_1, n_2, ... are the number of observations in each group. In the setup explained in the previous section the results belong to four groups that contain 25, 25, 25 and 4 observations respectively. Therefore the maximum number of possible permutation calculated as follow:

$$max_{perm} = \frac{79!}{25!\,25!\,25!\,4!} \,. \tag{34}$$

However this number is tremendously large and usually a much less number of permutations is enough for the purpose of statistical significance calculation. As suggested by [109], permutation number should be larger than 99, because permutation tests with a smaller number of permutations than 99 have too little power. Here we select the number of permutation to be 10000.

4. Generate the permutated data sets:
   It should be noted that since the variables in this test have different value ranges and means, the permutation is done only within columns. Also, each new permutated data set was compared to previously generated data sets to avoid the repetition.
5. Calculate the F-ratio for each permutation:
   The F-ratio is defined as the ratio of the between-group variability to the within-group variability, and it is calculated as follow:

$$F_{ratio} = \frac{\frac{\sum_{i=1}^{k} n_i(\bar{x}_i - \bar{x})^2}{k-1}}{\frac{\sum_{i=1}^{k}\sum_{j=1}^{n_i}(x_{ij} - \bar{x}_i)^2}{n-k}} \,, \tag{35}$$

where:

k is the number of groups,

n_i is the number of observations in the i^{th} group,

x_{ij} is the j^{th} observation of the i^{th} group,

$\bar{x}$ is the mean of all observations,

$\bar{x}_i$ is the mean of observations in the i^{th} group.

Since there are two principal components (PC1 and PC2), F-ratio is calculated for each component and the maximum value between the two is considered for the next steps.

6. Generate the F-distribution of the population set by aggregate the F-ratio values from all the permutation.
7. Calculate the F-ratio for the observed data set (original data set).
8. Calculate F_c, which is defined as the number of permutations with F-ratio larger than the F-ratio of the original data set.
9. Calculate the p-value as follow:

$$pvalue = \frac{no.of\ Permuation - F_c}{no.of\ Permuation} \ . \qquad (36)$$

The calculation were performed using MATLAB code listed in the next section. The calculated p-values are $1*10^{-5}$ and 0.0406 for the first and second principal component, respectively. Both of the p-values are below the selected level of significance, hence, **we reject the null hypothesis**.

Finally it is worth to notice two implications in the calculated p-values:

- As expected, the p-value of the first principal component is larger than the p-value of the second component, because the PCA algorithm sort the component based on their eigenvalues.
- To apply the permutation test, the observations in each groups assumed to be independent and identically distributed random variables. However, this is true only for the fourth group were the measurement repeated four times without the metallic plate. For each one of the other three groups, the test were repeated 25 times with changing the distance to the metallic plate at each time. It likely to get a better classification result (lower p-values) if the measurements were repeated without changing the distance.

3.5 Metallic Object Near Two Adjacent Antennas – Experiment II

In this section, the effect of a metallic object on the received power interference of two adjacent antennas was studied. Although distance measurements using frequency sweeping is a well-researched area [110, 111], this section investigates the ability of a low profile antenna, commercially available for current WSN technology, to be used as a detector for a nearby metallic object. Distance measurement using frequency sweeping is

an interesting technique, and it depends only on the received signal magnitude, making it suitable for inexpensive, off-the-shelf transceiver circuits. Also, it isn't affected by the fading caused by power losses over distance, as this techniques depends on the changes in the signal across frequency range rather than on the signal's absolute value. However, in our experimental setup, the reflection effect upon the metal plate was found to be too weak for distances further than 1 m, as it vanished rapidly.

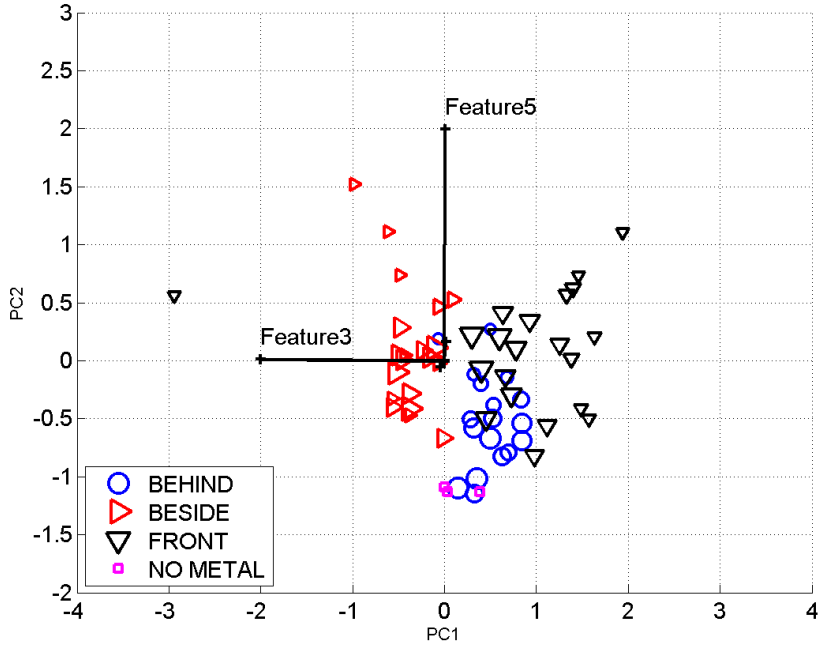

Figure 32: PCA classification for plate location, using extracted features of S-parameters

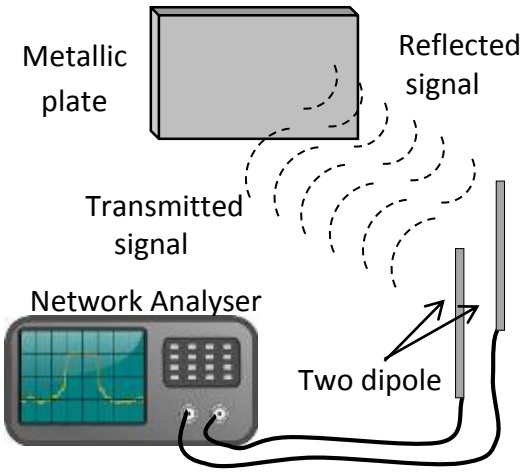

Figure 33: Distance measurement using two adjacent nodes

The experiment was conducted inside the same anechoic chamber described in Section 3.2. Two 2.4-GHz dipole antennas were fixed 10 cm apart and connected to an

Agilent-8363B Network Analyser. Both antennas were placed vertically, facing a metal plate (30 cm × 20 cm), which is fixed, using a sample holder that moves on a 1-m ramp. The distance (d) between the plate and the antennas was increased from 5 cm to 100 cm with 1 cm steps. At each step, the received signal is recorded over the frequency range, from 2 GHz to 3 GHz, with 5 MHz steps. Existence of other objects, i.e., the wooden ramp, desks and plastic holder, will affect the reading; however, the change in the signal will be related only to the metal plate, as it is the only thing that can change its position at each distance step.

By aggregating the S_{12} response for each distance step, a 2D surface for $V_{rec}(d,f)$, as a function of distance and frequency, is formulated. Figure 34 (a) shows the surface produced experimentally, while Figure 34 (b) shows similar results calculated analytically, using the reflection model in Section 2.2.3 for the same frequency and distance steps.

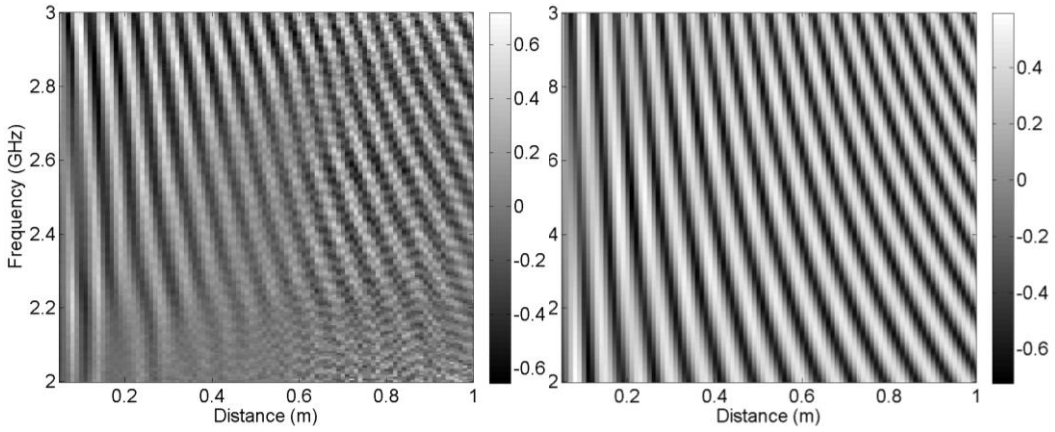

Figure 34: $V_{rec}(d,f)$ surface: (a) experimental and (b) simulation

The white regions in the figures represent peaks of the standing wave, while the dark regions represent the valleys. It should be noted that, to achieve this graph, the following steps were taken:

1. V_{rec} values represent the square root for the absolute magnitude of the S_{12} response.
2. V_{rec} values were normalised to the antenna pattern over a distance, to cancel the effect of fading due to distance change; i.e., at each distance step, the V_{rec} response over frequency was normalised to its mean value.
3. Then V_{rec} values were normalised to the antenna gain distribution across the frequency range. (Since the antenna gain is higher at the antenna resonant frequency).

When the plate is placed at 0.1 m, the receiver will suffer a single change in the received signal value (change from valley to peak) as the frequency is swept from 2 GHz to 3 GHz. But if the object were placed further away, e.g., 1 m, the receiver sensed six changes in the signal (changes from valley to peak) as the frequency changes. Figure 35 shows the change in the received signal across frequency at selected distances.

To draw a direct relation between the distance d and the change in V_{rec}, Fourier Transform (FT) was applied. Figure 36 shows the FT spectrum for the signals in Figure 35. The larger distances between the antenna and the metallic plate correspond to larger shift of the FT-magnitude components to a higher frequencies. Figure 8 shows the relation between the distance and location of the largest FT component (f_d). In this case, the accuracy in the distance estimation is approximately 15 cm. To gain more accuracy, we applied power spectrum centroid [112, 113] which is a measure of the middle-frequency component, obtained from the centre of area of the frequency response plot. The centre of gravity (COG) of FT components, was calculated using f_d the with its nearest two neighbouring FT components (f_{d-1} and f_{d+1}). The relation between the distance and COG(f_{d-1} , f_d, f_{d+1}) is also shown in Figure 37. Here, less than a 5-cm resolution was achieved. For distances larger than 20 cm, the relation between the COG(f_{d-1} , f_d, f_{d+1}) and the distance d, measured in centimetres, can be approximated as follows:

$$d \approx 0.0705 * \mathrm{COG}(f_{d-1}, f_d, f_{d+1}). \quad (37)$$

Accuracy of the distance measurement depends on the bandwidth used. A larger bandwidth achieves higher accuracy. However, a microwave radio signal of a 1 GHz bandwidth centred somewhere between 2 GHz and 10 GHz will have a wavelength of a few centimetres, which makes this range of frequencies more suitable for this technique.

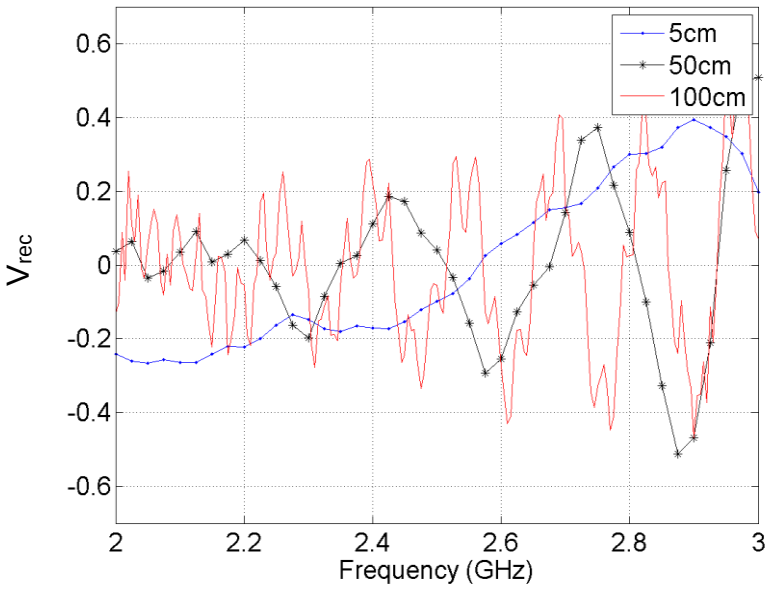

Figure 35: $V_{rec}(d,f)$ at selected distances

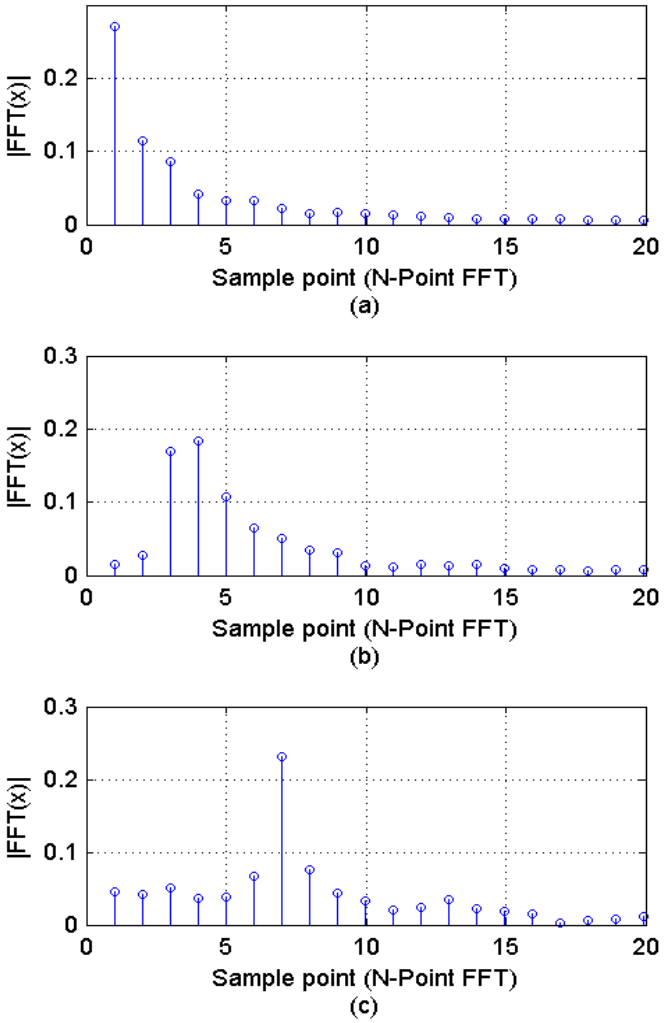

Figure 36: Fourier Transform of signal in Figure 35: (a) 1 cm, (b) 50 cm and (c) 100 cm, (Only the first 20 components are shown, as the rest are very close to zero).

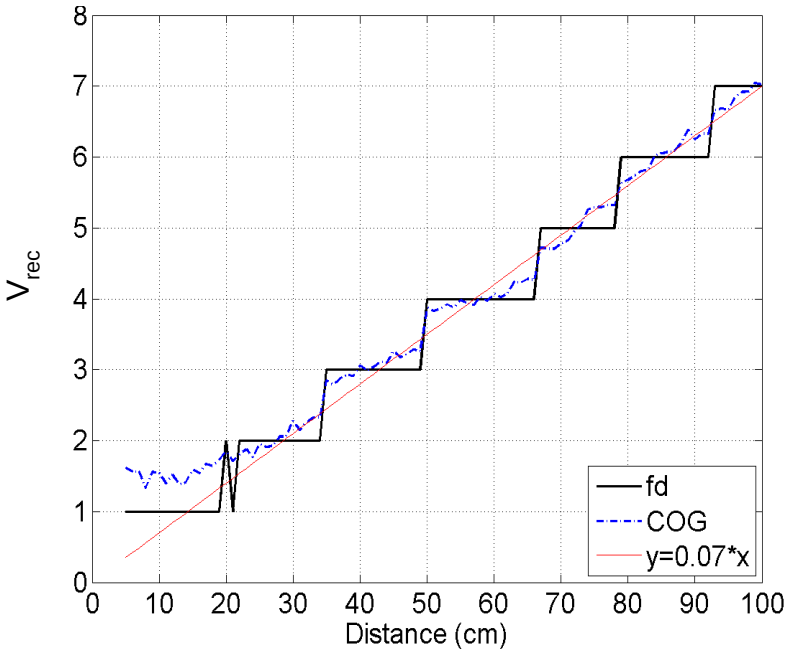

Figure 37: Relation of distance d and $V_{rec}(d,f)$ change

3.6 Summary

A metallic object near an antenna affects the signal strength, due to the reflection and shadowing. It also affects the antenna reflection coefficient, due to electromagnetic coupling. An experimental setup and simulation were presented to analyse the changes in the reflection coefficient over several distances within the near field of the 2.4-GHz dipole antenna. Results show that both the minimum value in the reflection coefficient response and the corresponding resonant frequency were changed, as the coupling distance changed. A relationship was concluded based on both parameters, to provide an approximate indication of the object distance to the antenna. Furthermore, principal component analysis was employed to show the antenna's ability to detect the object location around the antenna. The results show that using PCA with an S-parameter response has the potential to detect an object and estimate its location within a few wavelengths around the antenna. Another experimental setup was presented for a frequency sweeping distance measurement, where transmission coefficient measurements of two adjacent antennas were used to detect the distance to a nearby metallic object. However, the results of this method only accurate for distances outside the near field region. Although the tests and results presented in this chapter were achieved using a widely used, commercial, narrow band antenna, VNA is required to capture the effects. For these methods to be applied in low profile wireless nodes, they should be equipped with transceiver circuits able to measure the antenna reflection and transmission coefficients over a range of frequencies larger than the antenna narrow band.

Chapter 4 Design and Implementation of a Low Sensitivity UWB Antenna for WBAN Applications

4.1 Chapter Outline

In the framework of near field sensing in body area network, this chapter presents a new design for the UWB WBAN antenna. The chapter aims to introduce a design that conforms to the WBAN requirements of size, while achieving very low sensitivity when it comes in contact with the human body. As discussed in Chapter 2, the WBAN antenna is required to have an almost uniform radiation pattern in the plane parallel to the human body, and the radiation towards the body should be minimised to reduce absorption by the body tissue. The design starts by choosing a Vivaldi antenna widely used for ultra-wide band (UWB) application. Parametric studies and optimisation are presented at several design stages to maintain the reflection coefficient and radiation pattern within the WBAN requirements. Both the curved reflector and the horizontal feeding enhance the placement on the human body, while preserving a simple structure. Figure 38 shows the work flowchart.

This chapter is organised as follows. Section 4.2 introduces a brief background on the UWB WBAN requirement and related work. The design concept and simulation results are presented in Section 4.3, while the design implementation and experimental results are presented in Section 4.4. The tests of the antenna on the human body are discussed in 4.5. Finally, Section 4.6 concludes the chapter.

4.2 Background

A wide variety of applications that benefit from a wireless body area network (WBAN) requires both robust communications and high-precision ranging capabilities. These applications spans form the medical field to entertainment and gaming areas. Therefore, there has been an increasing interest in recent years in the use of ultra-wide-band (UWB) transmission technology in WBAN to fulfil these requirements. Low energy, spectral density, and the simplicity of the transceiver architecture are the main features that make UWB technology a good candidate for WBAN applications. Moreover, a UWB impulse radio can be used for robust data communications and precision ranging due its low susceptibility to multipath fading [114]. The desired operating frequencies for UWB are defined by U.S. Federal Communications Commission (FCC) regulations as 3.1 to 10.6 GHz.

One of the main challenges of a UWB system is the antenna design, as it plays a critical role in the WBAN applications. Generally, the UWB antennas require a compact form and low height, in addition to other inherent requirements, such as low back radiation and

suitable transient characteristics. However, reducing the UWB antenna size usually comes at the expense of deforming the radiation pattern and/or reducing the frequency bandwidth, due to impedance mismatch.

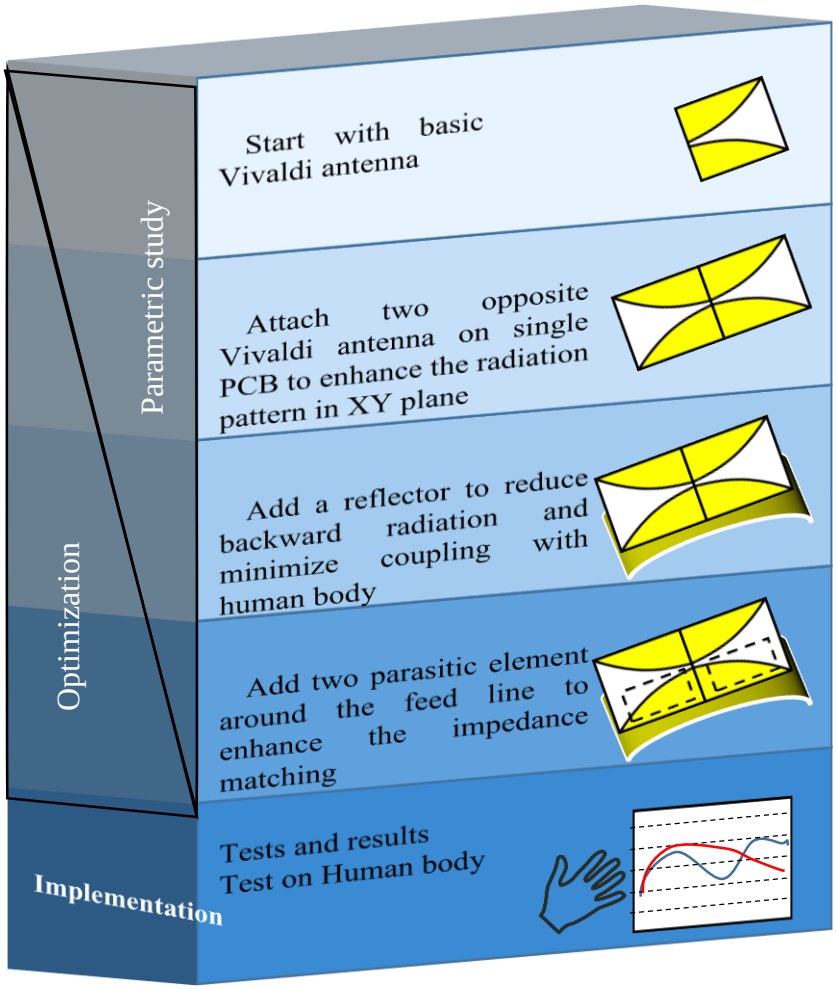

Figure 38: Flowchart of this chapter

Studies of the effects on antenna characteristics due to the human body and passive objects placed within the antenna near field have been increasing with the increase of wireless mobile devices [115-117]. Among the many designs for WBAN UWB antennas in previous studies, several have achieved reduced antenna dimensions, while maintaining good radiation and impedance measurements [5-8, 118]. Chahat [8] proposed a small printed UWB antenna with an overall height of 10 mm. The antenna showed good impedance matching over a UWB frequency range. A novel antenna presented by [5] consists of a bevel-edge feed structure and a metal plate with a folded strip, totalling 10 mm in height. The antenna shows a directional pattern with low back radiation, due to the 50×50 mm^2 ground plane. A directional, reduced-size wide slot antenna was presented by [118] for the 6-10 GHz band. A reflector plate was added to block the back radiation, making the final antenna height around 7 mm. Another low profile antenna, 8.5 mm in

height, was presented by [6] for WBAN. The antenna consists of two parts: a central mono-cone, responsible for the high frequency band, and a top-cross-plate, responsible for the lower frequency band. Both are fixed on a reflection plate that is 50 × 50 mm^2. The 3D printed miniaturised UWB antenna designed by [7] covers a wide frequency range, from 3.5-29.8 GHz. The design is characterised by its very small length and width dimensions compared to other designs, yet its height is 15 mm. It is worth noting that, although these designs offer an antenna height that is less than 15 mm [6-8], they require a vertical feeding (normal to the human body), which adds to the antenna height when it is installed on the human body and in the clothes.

Alternatively, a Vivaldi antenna is one of the promising candidates for UWB communication, due to its simple structure, broad band and high directionality. The Vivaldi design was first proposed by [119] and it has been adapted later by many researchers for several applications [120-122]. However, to accommodate a lower frequency, the antenna tend to have larger dimensions relative to other types of printed antennas. Several researchers have tackled Vivaldi antenna miniaturisation by introducing a loading element [123], slot edge [124], or stepped structure [125] to the original Vivaldi shape. However it is uncommon to use Vivaldi design in wearable applications because the antenna boresight extends along its length, making the antenna unsuitable for WBAN requirements. As an example, a new antenna design was proposed for on-body communication with an implanted capsule was presented by Wang [126]. In his design, a Vivaldi antenna was adopted to establish effective and efficient wireless links with the implanted capsule. The design is composed of four elements antenna on single substrate. Each element is composed of two opposite Vivaldi variants on one side of the substrate and is fed by a radial stub microstrip on the other side. With a metallic reflector at the Vivaldi side, a strong broadside radiation can be obtained from two opposite end-fire radiations resulting from two opposite planar Vivaldi variants. The final dimensions of the design are 131×131×10 mm^3. Results shows that 15-25 dB decoupling between the co- and cross-polarized components can be observed in 3-10 GHz.

4.3 Antenna Design Concept and Performance

The Vivaldi antenna is characterised by its high-gain, simple structure. However, the antenna is also known for its high directionality along it longest dimension. To comply with WBAN requirements, two Vivaldi antennas were placed on a single chip; by combining two opposite Vivaldi antennas on one PCB, the design achieves a more diverse radiation pattern in the PCB plane.

4.3.1 Proposed Antenna Structure

The two Vivaldi shapes were merged and fed by a single feed line to maintain the antenna's small size. Then a metallic sheet was added to the design to act as a reflector to minimise the antenna's coupling with the human body and reduce the radiation pattern towards the body. The antenna consists of a double-sided planar substrate and a curved reflector [127]. The bottom side of the planar substrate contains the feeding element with two parasitic patches, while the top side contains the radiator patches. The feeding element is a tapered strip line that extends from one side of the substrate to its middle, along the X-axis, and ends with two radial stubs that point toward the wide ends of Vivaldi shapes, along the Y-axis. On the top side, two radiator patches are placed side by side to form two Vivaldi shapes, opposite to each other. The shape of the radiation patches is based on parameter *p*, which defines the curvature of the Vivaldi antenna [128], as in the equation below:

$$\begin{aligned} f(y) &= Ae^{py} - Ae^{p} + \frac{g}{2} \qquad y \geq 0\,, \\ f(y) &= Ae^{p(-y)} - Ae^{p} + \frac{g}{2} \qquad y < 0\,, \end{aligned} \tag{38}$$

where *y* is starting from the centre along the Y-axis, and *A* is calculated as follows:

$$A = \frac{\frac{W}{2} - \frac{g}{2}}{e^{py/2} - e^{p}}. \tag{39}$$

Table 4: Description of antenna parameters

Symbol	*Description*
L	Antenna length
W	Antenna width
p	Vivaldi curvature exponent
g	Vivaldi gap
fw1	Feed line width (start)
fw2	Feed line width (end)
fL	Feed line length
f_rad	Feed stub radius
f_ang	Feed stub angle

The rest of the antenna's parameters are defined in

Table 4. By combining two opposite Vivaldi antennas on one substrate, the design achieved a more diverse radiation pattern in the XY-plane. Then, a reflector was added

to enhance the front radiation (along the +Z axis) and to reduce the radiation in the back hemisphere (along the -Z axis). The feeding point was connected to the strip line and one of the radiator patches. The schematic diagram of the top and bottom sides of the patch is shown in Figure 39 (a) and Figure 39 (b), respectively, while Figure 39 (c) shows the relative position of the reflector. Figure 40 shows a perspective view of the design.

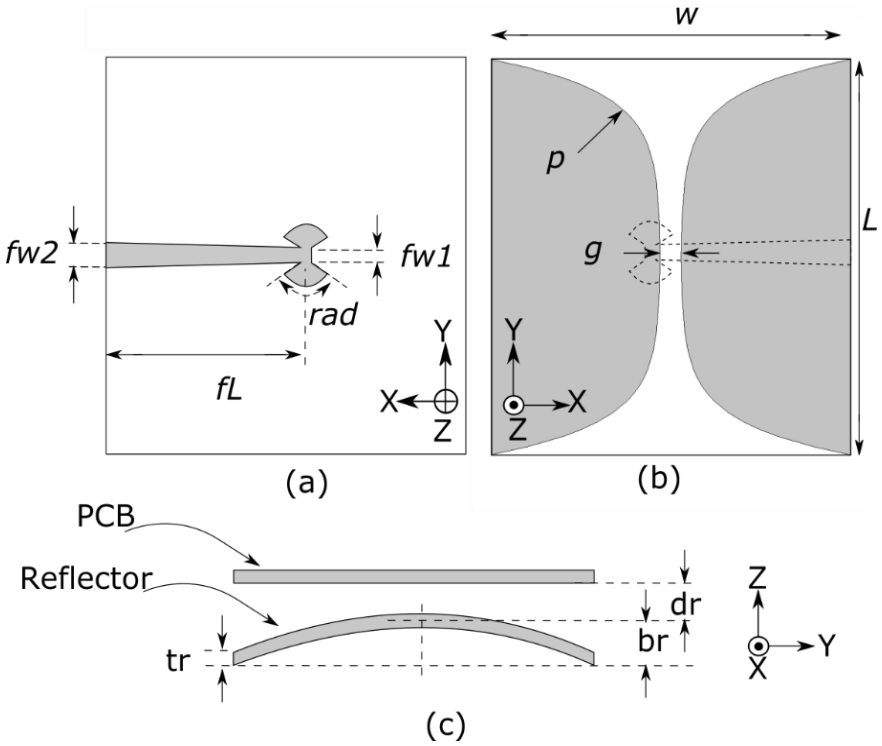

Figure 39: Antenna schematic: (a) bottom side, (b) top side and (c) reflector position

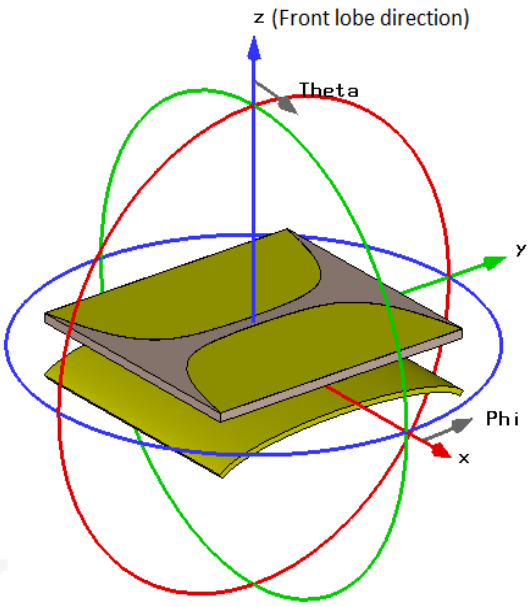

Figure 40: Proposed antenna (perspective view)

4.3.2 Parametric Study and Optimization

A parametric study was performed using selected parameters (shown in Table 5). The aim of the parametric study was to find the values that achieve the best impedance matching for the antenna, with a reflection coefficient of less than -10dB on the majority of the specified frequency band. Among the 216 simulation runs, only a few value combinations achieved this goal. Figure 41 shows seven selected responses that achieved -10dB over most of the UWB frequency range. The corresponding parameters of these seven simulation runs are listed in

Table 6. Generally, the width of the Vivaldi antenna should be greater than or equal to half the wavelength of the lower frequencies. However, results showed that changing the antenna width and length within the selected ranges doesn't have a significant effect on the impedance matching. The best values are shown to occur when the exponent, *p*, is set to a low value (around 0.2 mm), the feed line width is 3 mm and the feed line length is longer than half the antenna width.

Finally, the design parameters were optimised using the 'Trust Region Framework' optimisation method provided by CST MWS software. All of the parameters listed in Table 4 were optimised to within 10% of their initial values. The domain accuracy of the optimisation method was set to 0.001. The final values of the optimisation process are listed in Table 7.

Table 5: Parametric study instances

Parameter	*Parametric instances*
L	40, 52, 64 mm
W	48, 49, 50 mm
fW1	1, 2, 3 mm
fL	24, 25, 26 mm
p	0.2, 0.5, 0.7 mm
g	1.6, 2, 2.4 mm
f_ang	90°, 120°, 150°

Table 6: Parameter values for the responses shown in Figure 3

Run ID	*W*	*L*	*p*	*g*	*fw1*	*fL*	*f_ang*
1	48.0	26.0	0.2	1.6	3.0	26.0	120°
2	48.0	26.0	0.2	2.0	3.0	26.0	120°
3	49.0	26.0	0.2	2.0	3.0	26.0	120°
4	50.0	26.0	0.2	2.0	3.0	26.0	120°
5	48.0	26.0	0.2	2.4	3.0	26.0	120°
6	49.0	26.0	0.2	2.4	3.0	26.0	120°
7	48.0	32.0	0.2	2.4	3.0	26.0	120°

Table 7: Antenna parameters (mm) after optimisation

L	*W*	*L1*	*W1*	*p*	*g*	*fw1*	*fw2*	*fL*	*rad*
52	48	21.4	21.9	0.23	2.8	3.2	1.8	26.7	117°

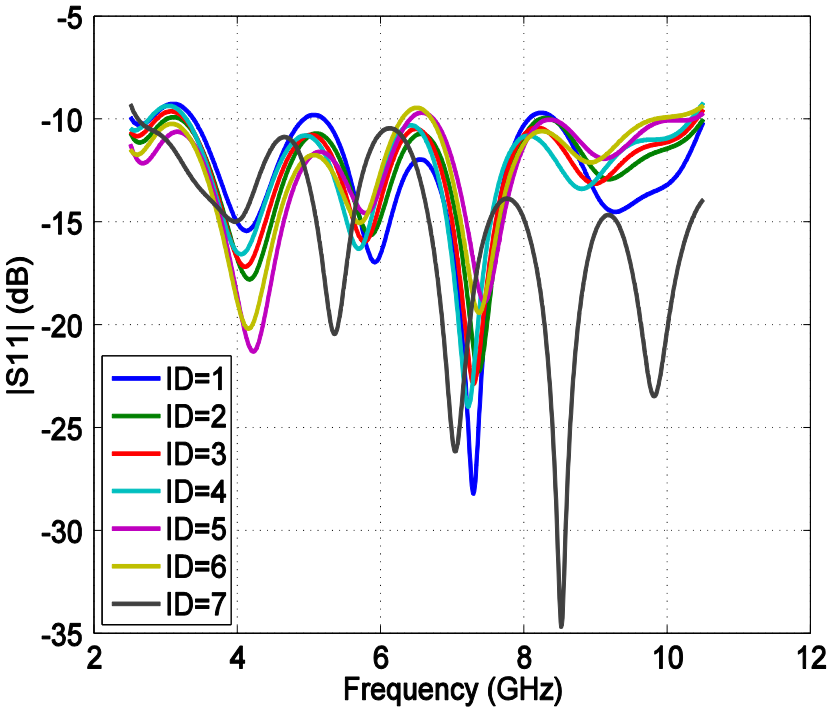

Figure 41: Reflection coefficient response for selected cases in the parametric study instances

4.3.3 Reflector Effect and Reflector Parametric Study

Although the Vivaldi antenna is a very good directional antenna, in the proposed design, both Vivaldi shapes are aligned to the body surface. To enhance the radiation pattern along the Z-axis, a reflector was added. Other ways to achieve a directional antenna pattern include adding the cavity or shielding plane behind the antenna or using the absorbing materials [129]. The usage a reflector with a WBAN antenna not only minimises the effects of the human body's proximity and body exposure to EM radiation, but it also increases the front lobe radiation, compared to the other methods. However, the introduction of a reflecting element had a large effect on the input impedance of the antenna, especially when the antenna is not inherently directional [58, 130, 131].

The proposed reflector, made of a thin copper sheet, is placed behind the substrate facing the bottom side, and the sheet is bent in an elliptical curve. Figure 39 (c) shows the

relative position of the reflector. The major radius is fixed at $L/2$, where L is the antenna length, while the minor radius, *br*, is variable. Hence, the sheet width is equal to the substrate width, and is slightly longer than the substrate to compensate for the curvature. The distance between the PCB and the reflector centre, *dr*, equals 5mm. To evaluate the reflector effect on antenna performance, a comparison of the antenna measurements without a reflector, with a flat reflector and with a curved reflector (shown in Figure 42) is conducted in terms of the radiation pattern and reflection coefficient. Figure 43 (a) shows that the front-to-back ratio on the XY-plane at 4 GHz changes from 0dB to 10 dB when a flat reflector is added at *dr*=5 mm. The results show that the change in the radiation pattern comes at the expense of increasing the reflection coefficient magnitude value ($|S_{11}|$). When the reflector is added, there is an increase of about 7 dB in $|S_{11}|$, as shown in Figure 43 (b). The total front-to-back ratio for the three selected frequencies at 4 GHz, 7 GHz and 10 GHz are 10.01 dB, 4.37 dB and 5.46 dB, respectively. The total front-to-back ratio (R_{Total}), is defined as the ratio of the summation of the radiated power in the upper hemisphere to the summation of the radiated power in the lower hemisphere, and is calculated as follow:

$$R_{Total} = \frac{\sum_{-90=<theta=<90} P_r}{\sum_{theta>90,\ theta<-90} P_r}, \tag{40}$$

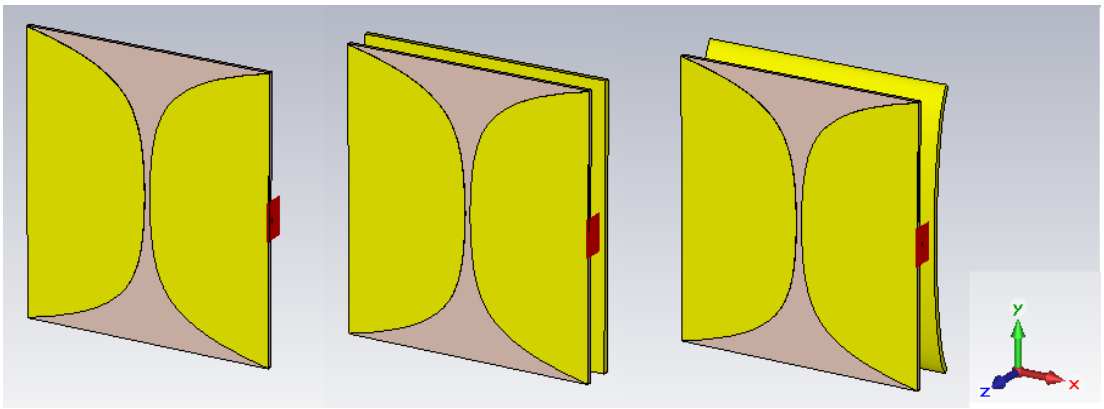

(a) (b) (c)

Figure 42: Proposed antenna: (a) without a reflector; (b) with a flat reflector; and (c) with a curved reflector

Figure 43 shows that the curved reflector (with *br*=5 mm and *dr*=5 mm) has

approximately the same effect on the radiation pattern but a lesser effect on the $|S_{11}|$ compared to the flat reflector. Hence, a curved reflector was adopted for the proposed antenna design. In addition to the enhancement in the radiation pattern, a curved reflector is more suitable t mount on human body parts, like an arm or torso, compared to the flat reflector.

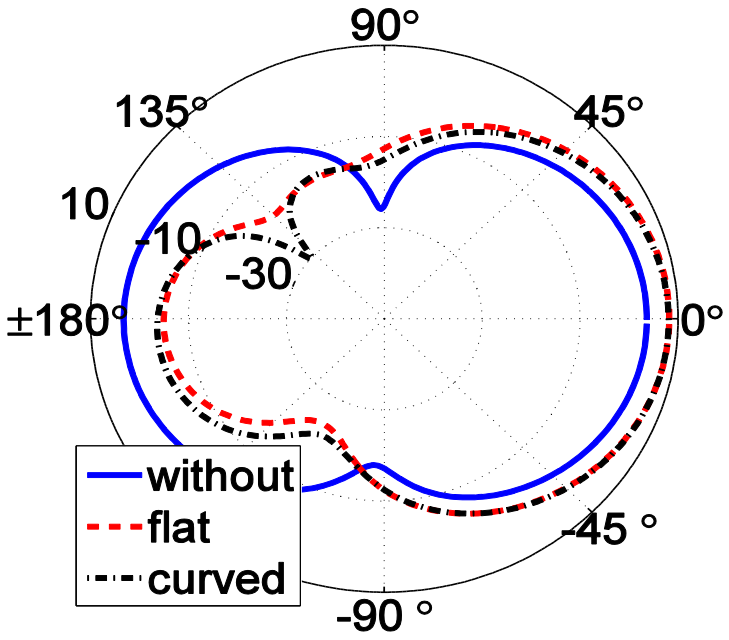

(a)

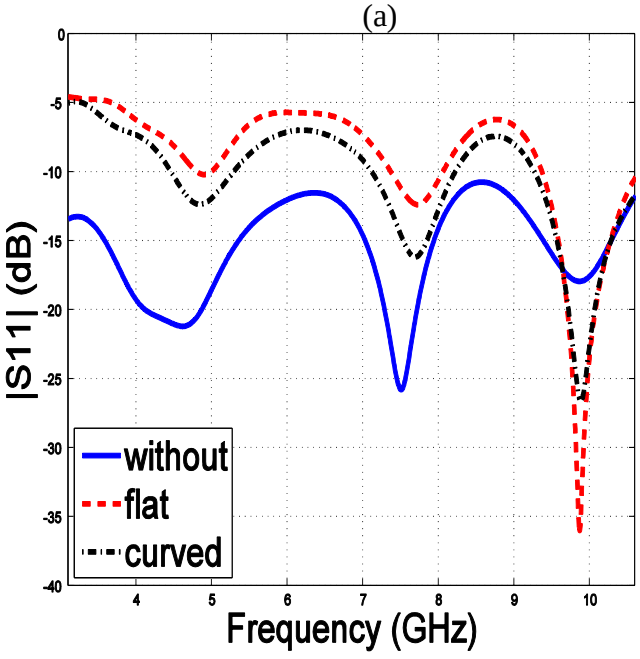

(b)

Figure 43: Comparison of the reflector effects, without the parasitic elements: (a) XZ radiation pattern at 4 GHz and (b) $|S_{11}|$ response

A parametric study was performed to evaluate the reflector effect on the antenna performance in terms of $|S_{11}|$. Three parameters were selected for this parametric study:

- The minor radius of the reflector curvature, *br*,
- The distance between the PCB and the reflector centre, *dr*,
- The reflector thickness, *tr*.

The range of both the *br* and *dr* values is between 1 mm and 9 mm, with a step of 1 mm, while the *tr* range is between 1 mm and 3 mm, with a step of 0.5 mm. Selected results are presented in Figure 44. As is expected, the larger values of *br* and *dr* correspond to the higher percentage of $|S_{11}|$ responses above the -10dB threshold. As *br* and *dr* increase, the effect of the reflector on the antenna is decreased and the $|S_{11}|$ response returns to its initial response without reflector, as shown in Figure 43 (b). However, increasing the *br* and *dr* values will result in a larger (thicker) antenna, which contradicts the size requirement of the WBAN antenna design. On the other hand, small values of *dr* will degrade the antenna performance, such as in the case of *dr*= 1 mm, where the response is above -8 dB at most frequencies in the specified range. It is worth noting here that, since the change in $|S_{11}|$ is within a few dB for a few millimetres of change in *br*, the curved reflector benefits outweigh its effects on the S_{11}. Moreover, the curvature makes the design more convenient for placement on different body parts, as discussed above.

For the reflector thickness, results show that *tr* has very little effect on the $|S_{11}|$ response. The average difference between 1 mm reflector and 3 mm reflector is less than 0.5dB. In the final design, both *br* and *dr* were set to 5 mm, which makes the total antenna thickness 11.6mm (including the antenna substrate thickness). Since the $|S_{11}|$ response is still higher than the -10dB threshold at some frequencies, a further step was taken by adding a parasitic elements; this will be discussed in Section 4.3.5.

4.3.4 Current distribution

A Vivaldi antenna is a traveling wave antenna, which means that the electromagnetic wave is radiated gradually as it moves through the antenna surface. The high frequencies are emitted first near the centre of the antenna, while the low frequencies are emitted later, at the edges. Therefore, the ends of the curved reflector participate more in lower frequency radiation than higher. This is evident from the current distribution, shown in Figure 45. Hence, the reflector has a greater effect on the radiation of lower frequencies than on the radiation of higher frequencies.

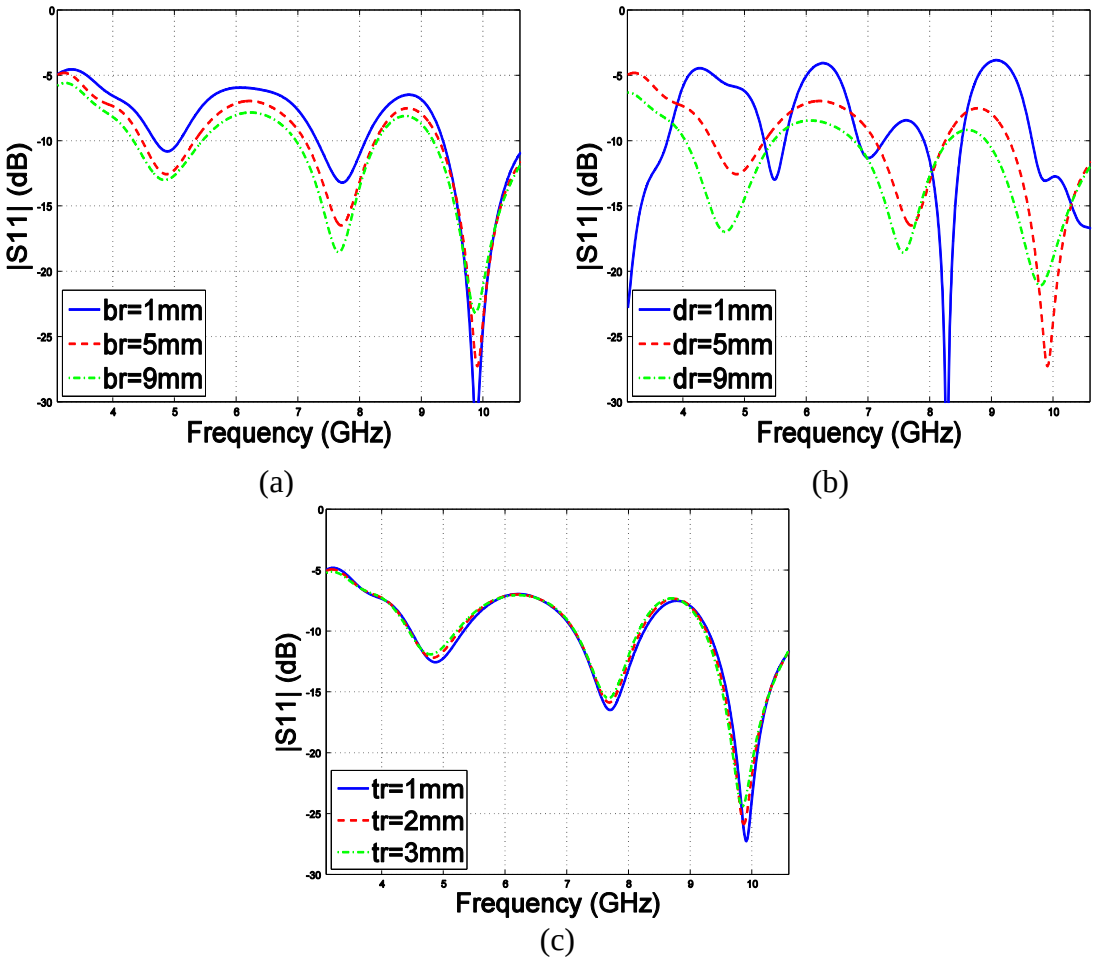

Figure 44: Parametric study of $|S_{11}|$ for reflector parameters: (a) *dr* = 5 mm, *tr* = 1 mm and variable *br*; (b) *br*=5 mm, *tr* = 1 mm and variable *dr*; and (c) *dr* = 5 mm, *br* = 5 mm and variable *tr*

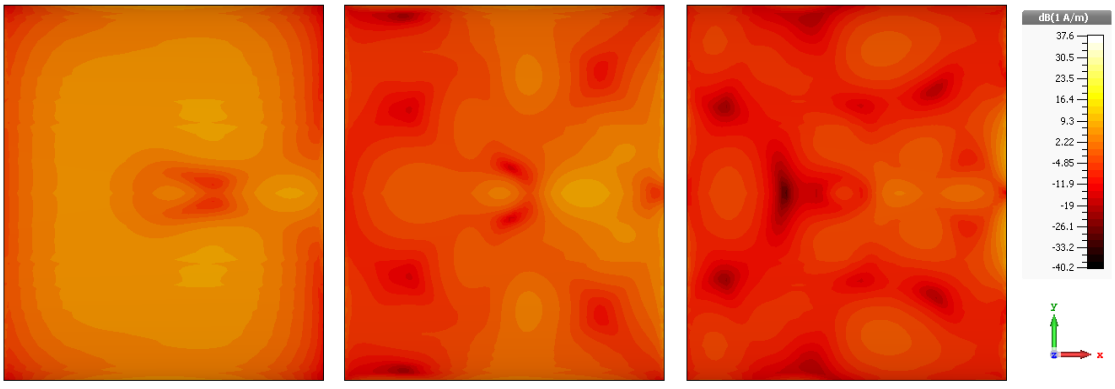

(a) (b) (c)

Figure 45: Current distribution of the reflector surface at (a) 4 GHz, (b) 7 GHz and (c) 10 GHz

4.3.5 Parasitic Element

After the introduction of the curvature to the reflector deign, $|S_{11}|$ response enhanced compared to flat reflector. To reduce the $|S_{11}|$ even more, a second step is taken by adding two parasitic patches to the bottom side of the antenna substrate (as shown in Figure 46). Not to be confused with coplanar waveguide, both patches act as parasitic elements, since they are not connected to the feeding point. The two parasitic patches are symmetric around the feed line and characterised by four parameters:

- *g1*: the gap between the parasitic patch and the antenna centre along the X-axis.
- *g2*: the gap between the parasitic patch and the feed line.
- *g3*: the gap between the parasitic patch and the antenna edge along the Y-axis.
- *g4*: the gap between the parasitic patch and the antenna edge along the X-axis.

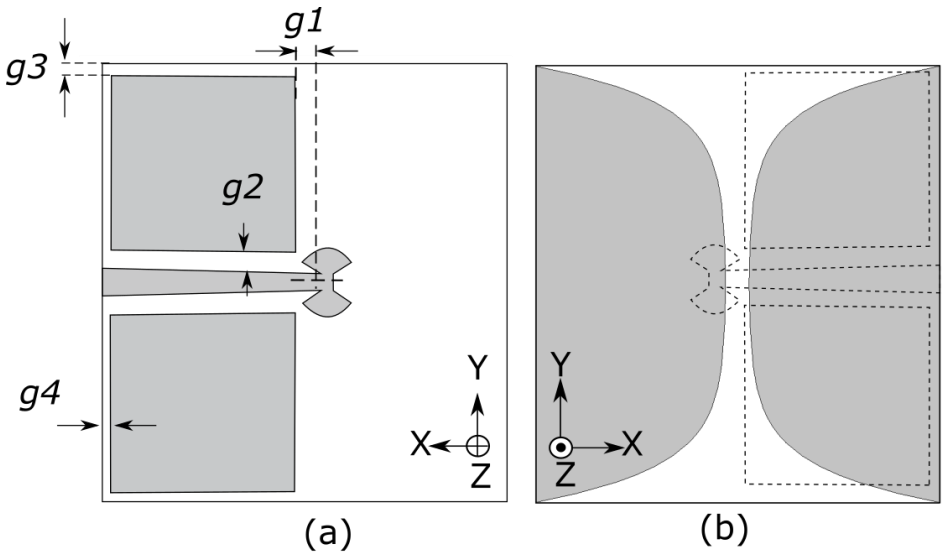

Figure 46: Proposed antenna schematic with parasitic patches: (a) bottom side and (b) top side

A parametric study for these four parameters was conducted in simulation. At each run, one parameter was set to 1 mm, 5 mm and 10 mm, while the other two parameters was fixed to 5 mm, and in every case, $|S_{11}|$ is recorded. The results showed that the antennas achieve better impedance matching when gap1, gap3 and gap4 are set to 1 mm. For gap2, the best results were achieved when it was set to a value larger than 1 mm.

The four parameters were also optimised, using the 'Trust Region Framework' optimisation method to achieve better matching. The final values of these parameters are shown in Table 8; hence, the dimensions of each patch are approximately 21.4×21.9 mm^2.

The $|S_{11}|$ response, with and without parasitic elements, is shown in Figure 48. The figure shows that, by adding the parasitic elements, the design achieves impedance matching over 90% of the specified range, with few regions where the $|S_{11}|$ response is greater than -10dB. These regions can be eliminated with further parameter optimisation.

Table 8: Parasitic patch parameters (mm)

g1	*g2*	*g3*	*g4*
1.3	3.8	0.7	0.6

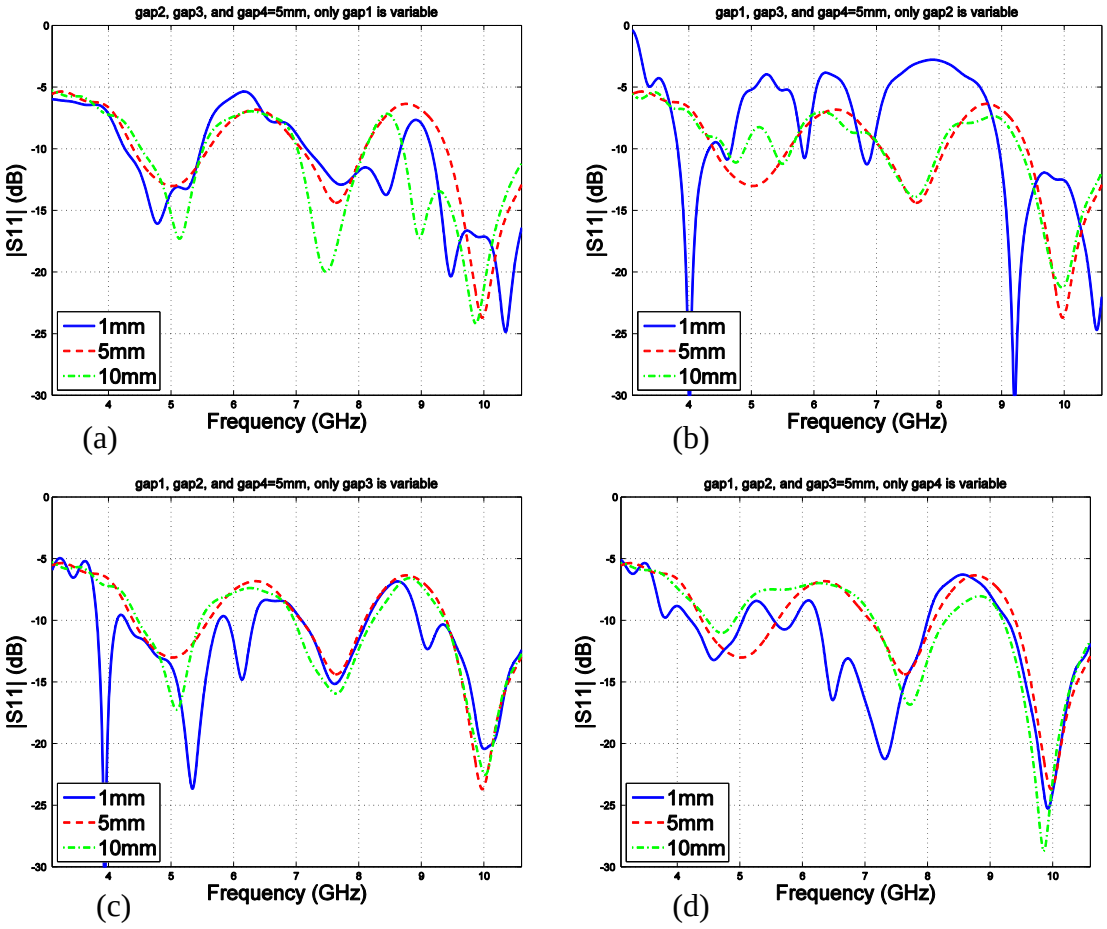

Figure 47: Parametric study of $|S_{11}|$ for parasitic patch parameters: (a) *gap1* variable, (b) *gap2* variable, (c) *gap3* variable and (d) *gap4* variable

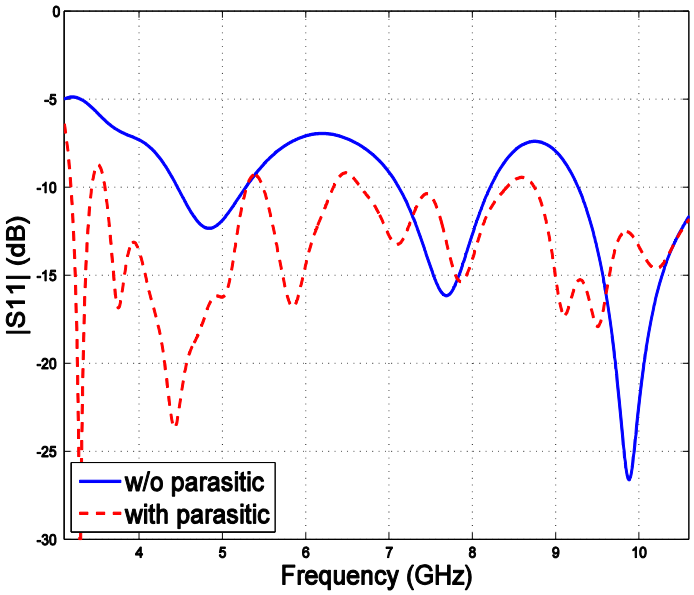

Figure 48: $|S_{11}|$ response with and without parasitic elements

4.3.6 Radiation Efficiency

In the simulation of the proposed antenna, another two antenna measurements were also considered: radiation efficiency and total efficiency. Radiation efficiency factor is the ratio of the radiated power to the total power accepted by the antenna, while the total efficiency factor is the ratio of the radiated power to the total power sent to the antenna, i.e., taking into account the impedance mismatch. To assess the effect of the parasitic elements and the reflector on the antenna, radiation efficiency and total efficiency were computed for the following cases:

- Antenna design with both the parasitic elements and the reflector
- Antenna design with the parasitic elements and without the reflector
- Antenna design with the reflector and without the parasitic elements
- Antenna design with neither the reflector nor the parasitic elements

The simulation measurements were recorded at three frequencies: 4 GHz, 7 GHz and 10 GHz; the results are shown in Figure 49. These results show that the antenna's total efficiency is higher at low frequencies. After introducing the reflector, the total efficiency drops to 70%. Meanwhile, adding the parasitic element enhanced the efficiency at a low frequency, yet it degraded the higher frequency radiation.

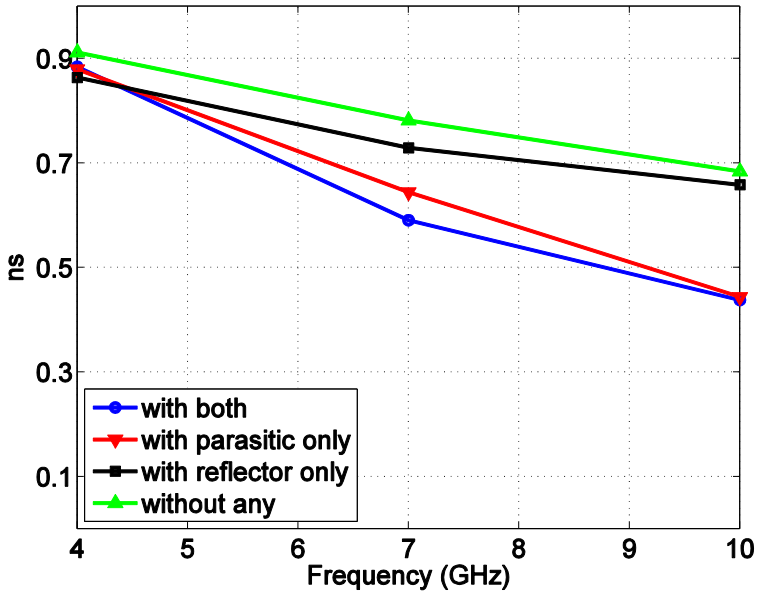

(a)

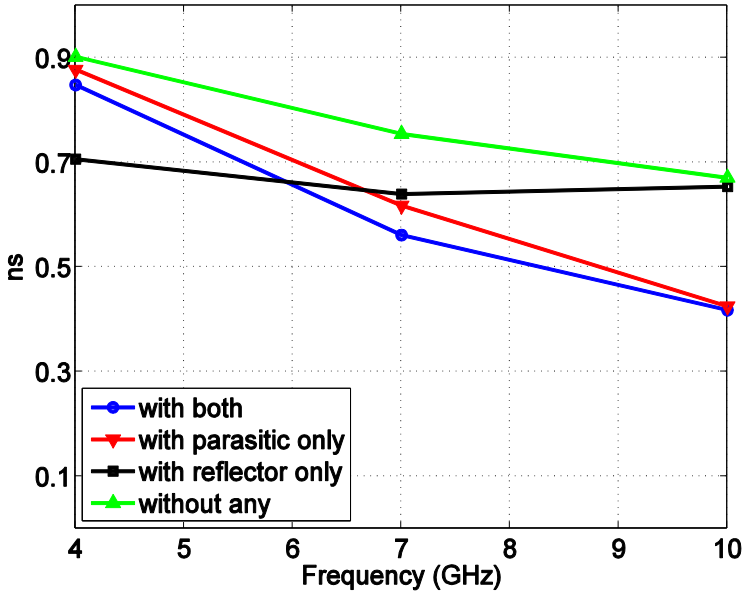

(b)

Figure 49: Antenna efficiency radiation with the effect of the reflector and the parasitic elements: (a) radiation efficiency and (b) total efficiency (b).

4.3.7 Group Delay

To assess the transient characteristics of the proposed antenna, the relative group delay is measured in simulation. The group delay $\tau_g(\omega)$ of an antenna characterises the frequency dependence of the time delay [132]. It is defined in the frequency domain as

$$\tau_g(\omega) = -\frac{d\varphi(\omega)}{d\omega} = -\frac{d\varphi(f)}{2\pi df}, \tag{41}$$

where $\varphi(f)$ is the frequency-dependent phase of the radiated signal.

Of interest is also the mean group delay $\overline{\tau_g}$, as it is a single number for the whole UWB frequency range:

$$\overline{\tau_g} = \frac{1}{\omega_2 - \omega_1}(\omega)d\omega\,, \tag{42}$$

A measure for the constancy of the group delay is the deviation from the mean group delay $\overline{\tau_g}$, denoted as a relative group delay $\tau_{g,rel}(\omega)$, and calculated as follow [132]:

$$\tau_{g,rel}(\omega) = \tau_g - \overline{\tau_g}. \tag{43}$$

For the proposed antenna, the group delay was measured in the simulation for the setup shown in Figure 50 (a), where the two antennas aligned along the Z-axis. Figure 50 (b) shows a comparison between the relative group delay of the proposed antenna with and without the parasitic elements. The figures show that, although adding the patch increases the relative group delay at some frequencies, yet the overall response is still within ± 0.1 ns.

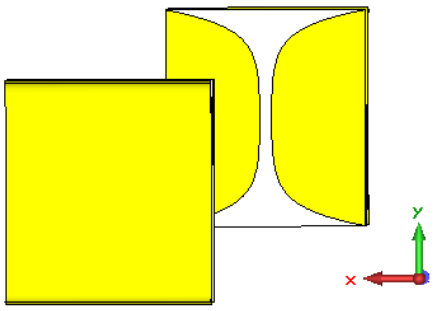

(a)

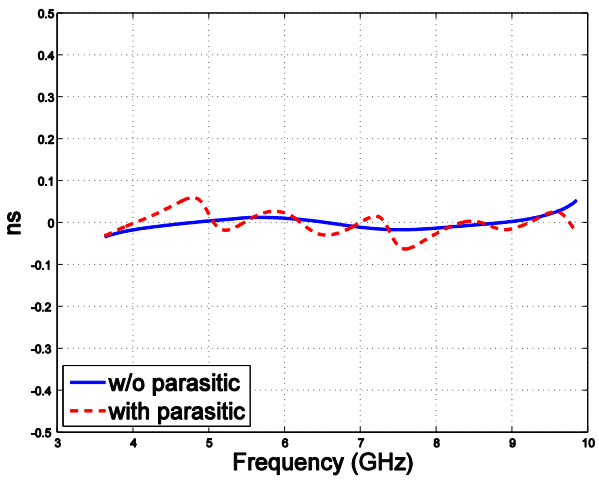

(b)

Figure 50: Group delay for the design with reflector (with and without parasitic elements)

4.4 Implementation and Experimental Setup and Results

The design was implemented using a double-sided FR4 fiberglass board with a relative dielectric constant $\varepsilon_r = 4.5$, tangent loss $\tan\delta = 0.022$ and 1.6-mm thickness. The reflector is made of a curved copper sheet with a conductivity of 5.8×10^7 S/m. The sheet's dimensions are 48×54.5 mm^2, with 0.5 mm of thickness. To make the structure mechanically stable, Styrofoam padding was added between the antenna and the reflector, so that *br* = 5 mm and *dr* = 5 mm. The dielectric constant of Styrofoam is very close to that of air [133], which does not cause a significant variance to performance. The final structural dimensions are $48 \times 52 \times 11.6$ mm^3.

Experimental measurements of the antenna were taken inside an anechoic chamber, where the antenna reflection coefficient and radiation pattern were recorded. Figure 51 shows the measured and simulated $|S_{11}|$ response. Good agreement between the simulated and measured results can be observed over the whole UWB band, while a slight inconsistency exists at some frequencies, which is likely due to the deterioration of the test jig.

Similarly, the radiation pattern was measured inside the anechoic chamber in both the XZ- and YZ-plane. In each plane, the radiation pattern was measured in both co-polarisation (*Phi* angle) and cross-polarisation (*Theta* angle). Each radiation pattern was recorded at 23 steps (15° rotation). For comparison, Figure 52 shows the simulated vs measured radiation pattern in the YZ-plane at 4GHz. The figure highlights some differences between the simulation and the experimental results. However, the radiation pattern shapes of the experimental results conform to the radiation pattern shapes of the simulation and the differences are only in the magnitude values of each set. Hence, these differences are mainly due to the slight implementation variance. The measured radiation patterns of the antenna at three selected frequencies—4 GHz, 7 GHz and 10 GHz—are shown in Figure 53 for both the XZ- and YZ-planes. Both sets of results show that the radiation pattern in the front lobe (along the +Z axis) is always larger than that of the back lobe (along the -Z axis), especially at lower frequencies, as discussed in the previous section. Also, both sets of results show that the cross-polarisation component is stronger in the XZ-plane than the co-polarisation component, while in the YZ-plane, the case is reversed. This is expected, since the radiation of Vivaldi shape is inherently polarised.

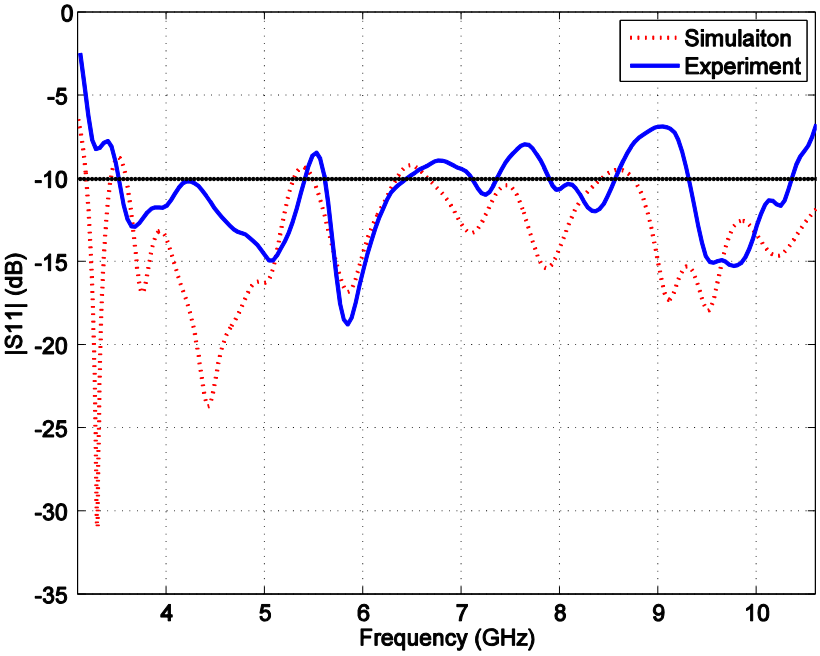

Figure 51: Simulated and measured antenna $|S_{11}|$ response

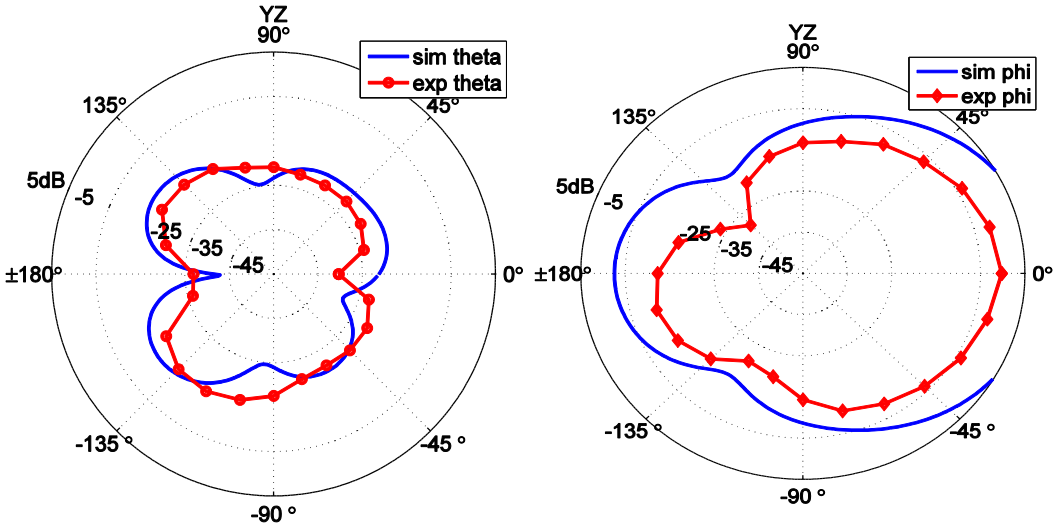

Figure 52: Simulated vs measured radiation pattern in the YZ-plane at 4 GHz

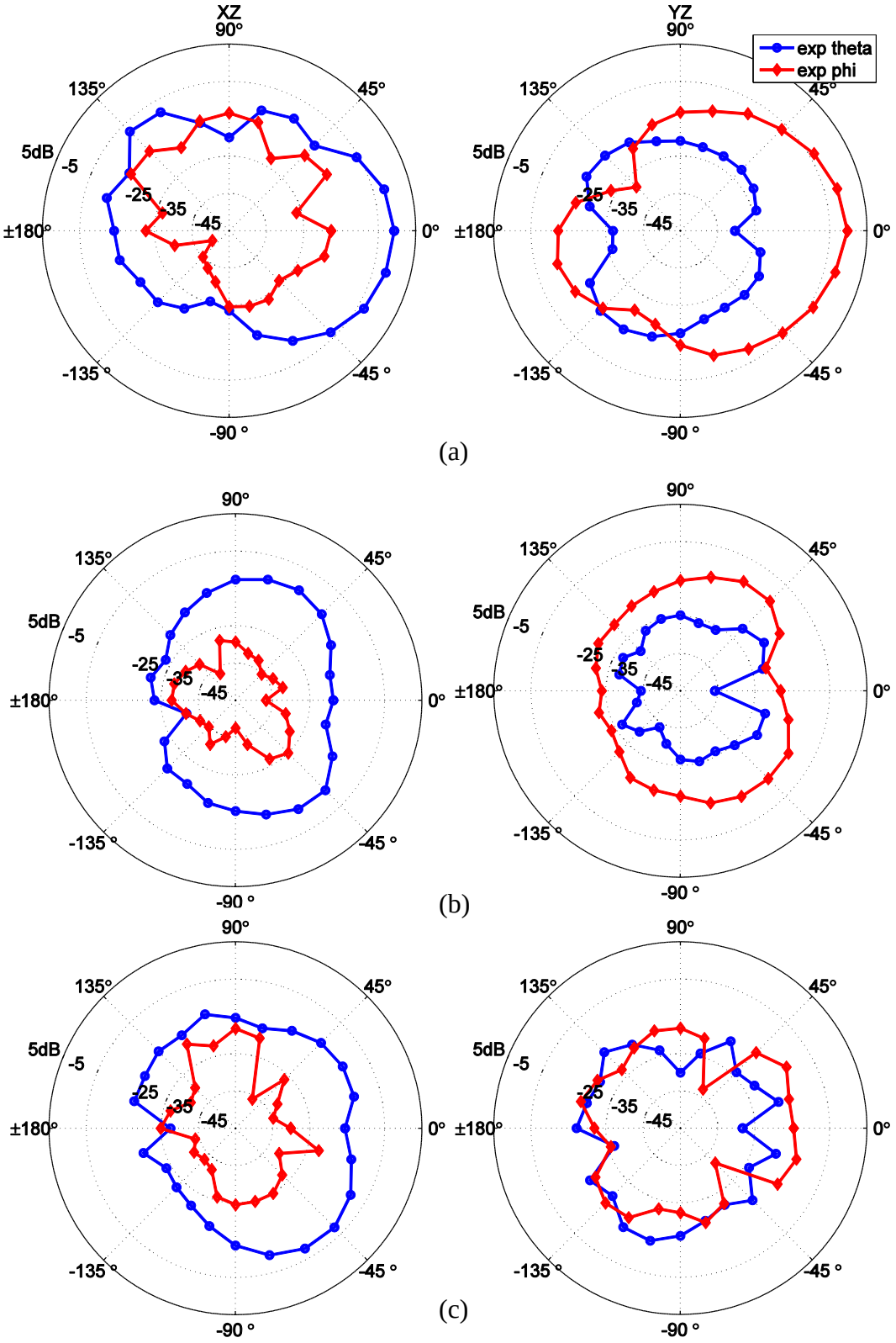

Figure 53: Measured radiation pattern in the XZ- (left) and YZ- (right) planes at (a) 4 GHz, (b) 7 GHz and (c) 10 GHz.

4.5 Human Hand Experiment

To evaluate the antenna's performance with human proximity, a test was done outside the anechoic chamber. In this test, the antenna reflection coefficient was first measured without human proximity in an indoor environment, and then the reflection coefficient was measured when the antenna was mounted on a human body. The stimulus power of the VNA port was set to 0 dBm. Two cases were considered for the human body's test position: *on hand palm* and *on arm* (shown in Figure 54 (b) and Figure 54 (c), respectively). For the *on arm* position, the antenna's contact area with human skin is larger than it is in the *on hand palm* position, because of the curvature. It should be mentioned that, although the UWB antennas are expected to see a trivial change under the proximity effects, due to their low-Q nature, they can be sensitive to the proximity of the human body [6].

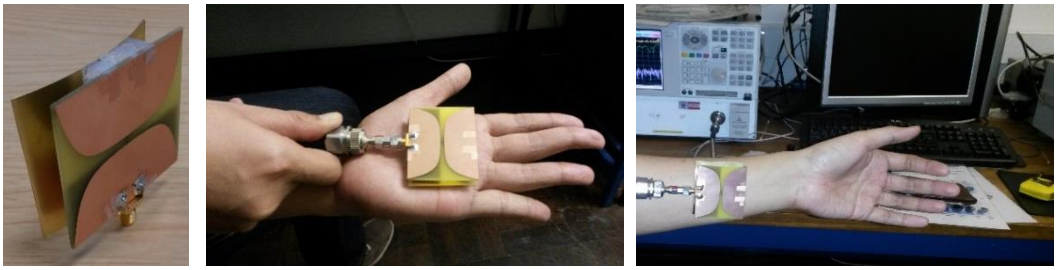

(a) (b) (c)

Figure 54: Proposed antenna: (a) antenna picture; (b) on hand palm test position; and (c) on arm test position

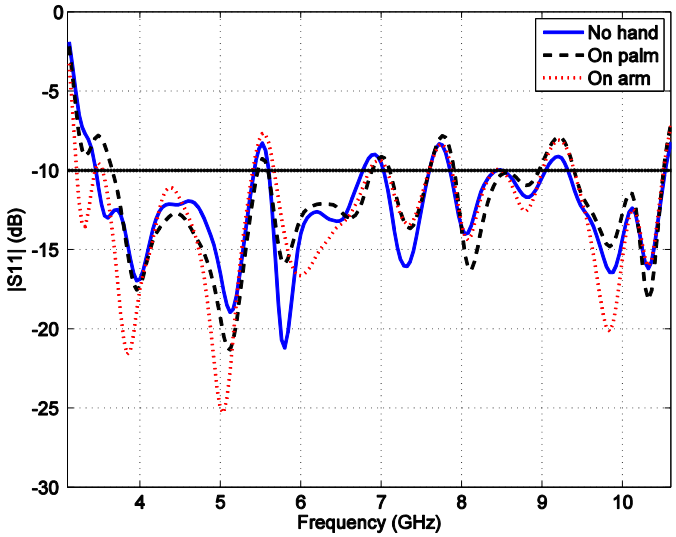

Figure 55: Measured |S11| response outside anechoic chamber, with and without the human hand.

The test results shown in Figure 55 show the low sensitivity of the proposed antenna

to the human body's proximity. For the '*on arm*' position, even though the reflector is attached directly to the body surface, yet the change in the $|S_{11}|$ response is insignificant, except for a few frequencies in which the change reaches 5dB.

4.6 Summary

This chapter presented a new antenna design for wireless body network (WBAN), characterised by its compact thickness and low back radiation. The proposed design makes use of a Vivaldi antenna widely used for an ultra-wide band (UWB), and it modifies the size and radiation pattern to match the WBAN requirements. Two Vivaldi shapes are fit onto a single PCB to achieve a broader radiation, then a curved reflector is added to enhance the front-to-back ratio, with a total antenna height of 11.6mm. Both the inherent horizontal feeding of the design and the curved reflector improve the design suitability for placement on the human body. The antenna's performance, in terms of the reflection coefficient and radiation pattern, was measured experimentally inside an anechoic chamber, and the experimental results show good matching with simulation. In addition, the results show that the proposed design can operate in most of the UWB band approved by the Federal Communications Commission (3.1–10.6 GHz), with a front-to-back ratio of up to 10dB at low frequencies. Finally, a test on a human hand is presented to demonstrate the antenna's sensitivity to contact with the human body.

The main issues of the design process and the results can be summarised as follows:

- The Vivaldi antenna structure is simple and can be adapted to fit the WBAN requirements of small size and radiation pattern, in addition to the Vivaldi antenna's inherent characteristics, such as high gain and wide-band impedance matching.
- Introducing the reflector to the design reduced the backward radiation and enhanced the front-to-back-ratio. It also reduced the antenna sensitivity to coupling with the human body. However, the reflector affected the impedance matching and, therefore, reduced the antenna's total efficiency, especially at the higher frequencies. To enhance the impedance matching, two parasitic patches were added to the design.
- To test the antenna sensitivity to the human body, experiments were conducted, whereby the antenna is mounted on a human hand and arm. Results in terms of the reflection coefficient show an insignificant change when the antenna is placed on human skin.

Chapter 5 NEAR-FIELD SENSING USING THE UWB WBAN ANTENNA

5.1 Chapter Outline

In the framework of sensing nearby objects using the WBAN antenna, the previous chapters presented a study of the effects of metallic objects on the measurements of a narrow band antenna, and proposed selected features to be used as indicators for object existence and distance. Then the design and implementation of a low profile UWB for the WBAN application was proposed. Simulation and experimental tests were performed, off-body only. The aim of this chapter is to study the combined effect of the human body and metallic object in the near field on an UWB antenna and to investigate the reflector effects on antenna sensitivity to nearby objects. With regard to this aim, the following objectives are targeted by this chapter:

- Measure antenna sensitivity to a nearby object without the human body
- Validate the low sensitivity of the proposed antenna to the human body.
- Investigate the reflector's role in changing the antenna sensitivity to the human body and nearby object.
- Analyse the antenna measurements and extract indicators to detect and estimate the distance to nearby objects within the antenna near field.

First, to achieve the above objectives, this chapter presents a set of experimental tests and it is followed by data analysis. The experimental tests involve on-body and off-body experiments, which use the two proposed designs from the previous chapter, i.e., with and without a reflector. Then, the chapter presents an analyses of the S-parameters and proposed two new features. Finally, a classification method is used to classify the object location for the on-body tests. A diagram details the work of this chapter in Figure 56.

This chapter is organised as follows. Section 5.2 presents a brief background WBAN near field sensing. Section 5.3 presents the off-body test setups and data analysis, while the on-body test setups and data analysis were presented in Section 5.4. Section 5.5 presents the two proposed indicators for the metallic object's distance from the antenna in the on-body test. Classification results for metallic object detection using PCA are presented in Section 5.6. Finally, Section 5.7 concludes the chapter.

Tasks	Objectives	Methods
Off-body experimental measurements	• Measure sensitivity to nearby object without human body	• Measure and compare antenna S-parameters with metallic object nearby the UWB at several locations.
On-body experimental measurements	• Validate the design objective • Study the reflector effect on the antenna sensitivity	• Measure and compare antenna S-parameters: o On several body parts o With and without metallic object o Variable distance to the object
Data analysis	• Detect the metallic object existence. • Estimate the distance to the metallic object.	• Analysis of antenna measurements: o Root means square o Peak to peak o PCA classifier

Figure 56: Chapter-5 layout

5.2 Background

Although WBAN shares many of its characteristics and challenges with other types of wireless sensor networks, it suffers from a unique challenge, presented by the continuous change in the surrounding environment, due to the continuous movement of the human body, monitored by the WBAN. This challenge, combined with the fact that WBANs are assumed to usually work in an indoor environment, complicates the channel model. The investigation of indoor channel models for WBAN usually covers the effects of indoor objects (in the far field), and it is currently an active topic for many researchers [134-137]. An experimental characterisation for an off-body propagation channel at different positions is presented in [138]. The effects of a pseudo dynamic of the human body on the signal propagation in WBAN were also studied for narrow band antennas [139], ultra-wideband antennas [140] and RFID tags [141]. Antenna diversity was presented as a solution to relieve the negative effect of human movement on the channel conditions [17, 32, 142]. For contact with the human body, authors in [143] presented a simplified spherical model of the lossy body and studied its interaction with elementary sources placed within or on it. The effect of clothes on a textile antenna was studied by [9], using a set of experiments with a number of garments, including a thick woollen jumper and a ski jacket. Although the effect of metallic objects near antennas is highly addressed in

fields like RFID tags [29], this topic has not been investigated thoroughly for WBAN applications.

5.3 Off-body Antenna Measurements with a Passive Object in the Near Field

In this section, the proposed antenna was tested inside an anechoic chamber to measure the change in the antenna measurements when a metallic object was presented in the antenna near field. Tests were conducted without the existence of a human body. The experimental setup and results are detailed in the following subsections.

5.3.1 Experimental Setup for Off-body UWB Antenna with a Metallic Object

The experiment was conducted inside an anechoic chamber of steel construction, which measures 2.5 m × 2.5 m × 2.5 m, and the internal ground, ceiling and walls are clad with a foam absorber material. The setup in general is similar to the experimental setup described in Chapter 3. However, in this chapter, the proposed antenna is used, instead of the narrow band antenna. Two UWB antennas were used, both implemented as the antenna with a reflector design, described in Chapter 4. The two antennas, named *Antenna#1* and *Antenna#2*, were vertically fixed with a plastic stand on a wooden stool, with a distance of 2.25 m between them and 1m above the chamber floor, as shown in Figure 18. The effect of the wooden stool and the plastic stand was ignored, as the metallic object location was the only variable that was changed in each experimental setup. S-parameters were measured and recorded for both antennas, using a 2-Port network analyser (Agilent-8363B). The network analyser was set to work in the frequency range from 3 GHz to 11 GHz, with 40 MHz steps; hence, each response consists of 201 frequency steps.

A mild steel plate of dimensions 30 × 20 cm^2 was used as the metal object. The object length and width were selected to be larger than the antenna length to reduce the likelihood of signal diffraction, due to the object's edges affecting the results. In contrast, object thickness doesn't affect the results, considering that the mutual coupling is actually happening between the antenna and its image on the metallic surface. Hence, the experimental results will be valid for larger objects as long as they have an almost flat surface facing the antenna. The plate was placed in three positions relative to the two antennas, and they were named *p1*, *p2* and *p3* (shown in Figure 19), similar to the setup in Section 3.2.

At each position, the plate was fixed vertically, facing the antenna. The distance between the plate and the antenna (*d*) was changed from 1 cm to 25 cm, as the plate was

moved 1 cm away from the antenna each time. In the experiment, the distances between 1 cm and 25 cm to include the near field and radiated near-field areas.

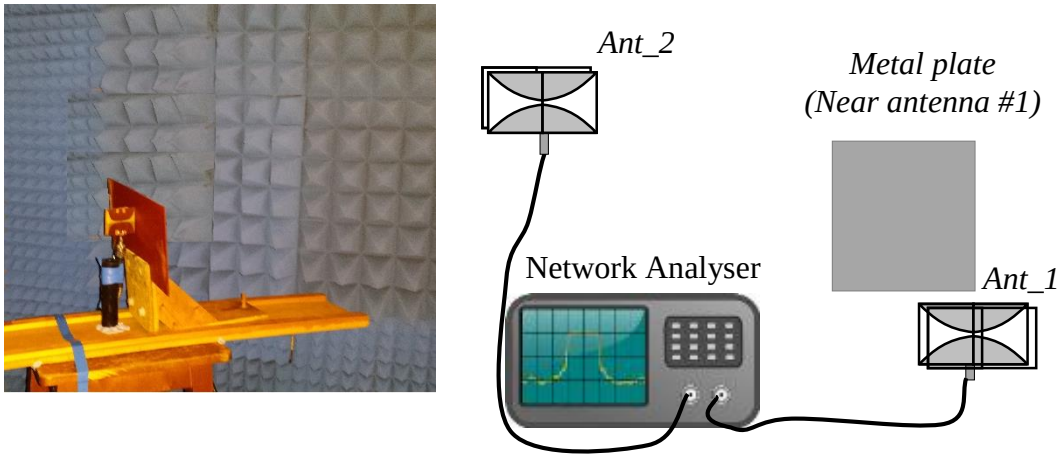

Figure 57: Experiment setup: (a) antenna and metal object picture; (b) setup illustration

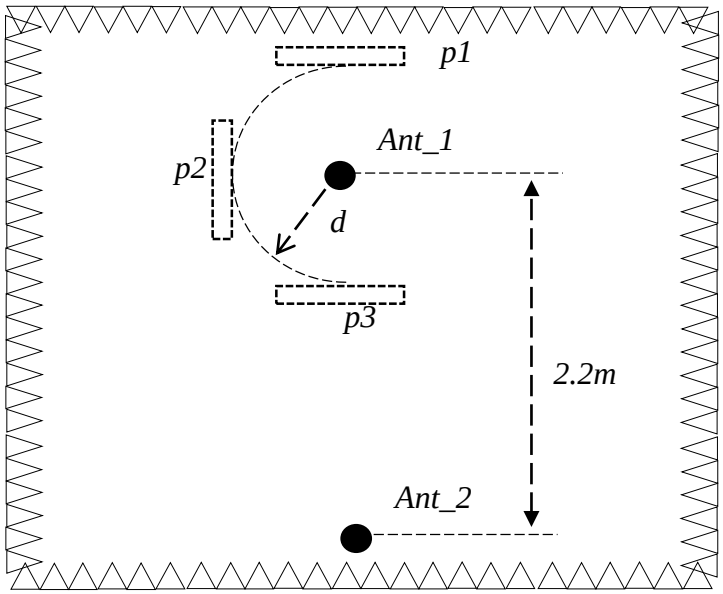

Figure 58: Off-body test setup layout (top view) shows the positions of the plate and the antennas

5.3.2 Results and Discussion for Off-body Antenna with Metallic Object

In the discussion below, only the magnitude values of the S_{11} and S_{12} parameters are considered, as explained in Section 3.2. The S_{11} and S_{12} magnitudes were plotted against the frequency and the distance *d*, as shown in Figure 59 and Figure 60 for the three positions, *p1*, *p2* and *p3*. For more clarification, the responses of S_{11} and S_{12} at selected distances are also shown, in Figure 61.

By examining Figure 59, the following observations about the S_{12} magnitude values can be concluded:

- In general, the S_{12} magnitude values at lower frequencies are around -50 dB, while at higher frequencies, the values are below -70 dB, which is due to the fact that the antenna radiation efficiency is better at lower frequencies, as explained in Chapter 4. Hence, the effects of the metallic object are much clearer at lower frequencies. The highest values of S_{12} occur around the 4-GHz frequency.
- At position *p1*, the metallic plate acts as a reflector behind *Antenna#1*. As the metallic plate is moved gradually, the S_{12} values oscillate up and down, due to interference of the reflected signal from the metallic plate. The oscillation is about 5dB from peak to peak, and the oscillation rate, with respect to distance *d*, is about 5 cm at 3 GHz; this becomes 3 cm at 6 GHz. At higher frequencies, the oscillation is buried under the noise level.
- At position *p2*, the metallic plate still acts as a reflector, but the interference is less than *p1*. The oscillation in the S_{12} value is indistinct (within 2 dB) and only noticeable around the 4-GHz frequency.
- At position *p3*, the metal plate blocks the transmitted signal and causes a severe reduction in transmitted power in the first 5 cm, which makes the S_{12} value drop below -50dB. As the metal plate is moved away from the antenna, the S_{12} values increase. For distances greater than 20 cm, the effect vanishes and the value settles on the remaining magnitude values.

Figure 60 shows the S_{11} responses with distance *d*. The change in S_{11} can be summarised as follows:

- Since the antenna has a non-uniform radiation pattern along the H-plane, the effects of the metallic object on S_{11} in the three positions are different.
- At position *p1*, the value of S_{11} is almost constant with respect to change in distance *d*. This is because the reflector is shielding the antenna from the effect

of the metallic plate.

- At position *p2*, the S_{11} value changes up and down with a change in distance *d*, mainly in the frequencies below 8 GHz; meanwhile, for higher frequencies, the S_{11} response is almost constant with the change in distance *d*. This is related to the fact that the antenna radiation efficiency below 8 GHz is much higher than its efficiency above 8 GHz. For distances less than 5cm, the change in the S_{11} values is around 10dB. For distances greater than 5 cm, the response is settled, except for the band around the 4-GHz frequency, where the S_{11} value is still affected by the change in *d*.
- At position *p3*, the response of S_{11} is almost constant, except for slight changes around the 4-GHz and 6-GHz frequencies. For distances less than 5cm, these changes are about 5dB and they become less than 2 dB for larger distances.

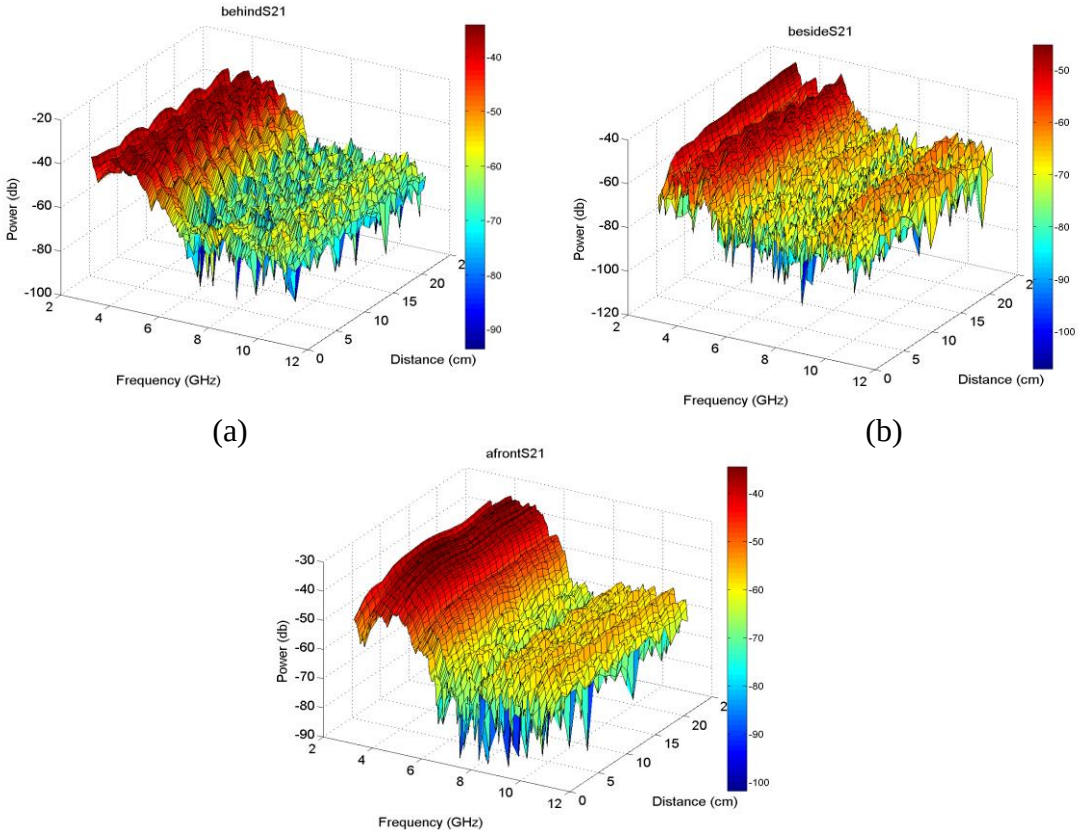

Figure 59: S_{12} magnitude for Off-body antenna at position (a) *p1*, (b) *p2* and (c) *p3*

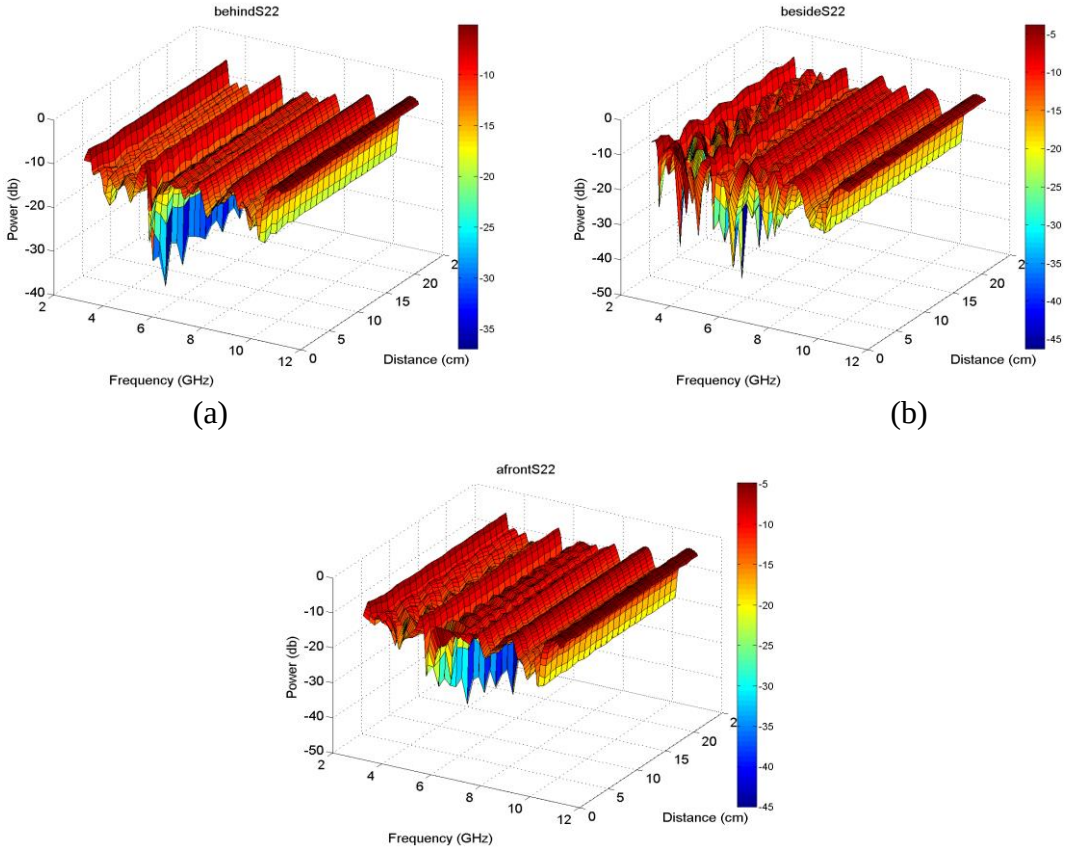

Figure 60: S_{11} magnitude for Off-body antenna at position (a) *p1*, (b) *p2* and (c) *p3*

Figure 62 and Figure 63 show the minimum values of the S_{11} responses, as well as their corresponding frequencies plotted against distance. Although the proposed antenna is a UWB antenna, these graphs show how some local resonant frequencies change due to a nearby object. It is clear from Figure 62 that the minimum value of the S_{11} response changes with distance *d*, and this change is within a few dB at position *p1*. At positions *p2* and *p3*, the changes are larger than that of *p1* and about 10dB below 15cm; they become smaller as *d* increases. However, the frequencies corresponding to the minimum values appear to be unaffected by distance *d*, as shown in Figure 62 (a) and Figure 62 (c). This is because the S_{11} responses were recorded at a 50-MHz step; hence, small changes in frequency (within a few MHz) are not shown in the graphs. Although Figure 62 (b) shows large changes in the frequency value, this is only because the S_{11} response of the antenna at *p2* exhibits several resonant frequencies with relatively equal return loss values, as shown in Figure 61 (b).

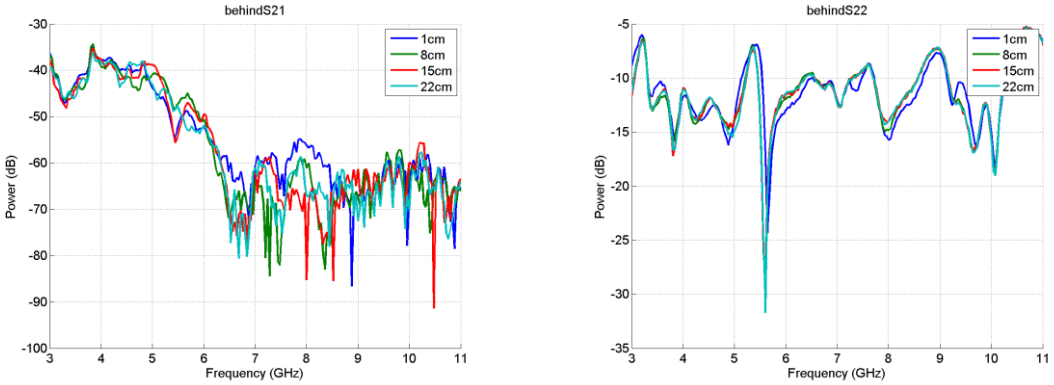

(a)

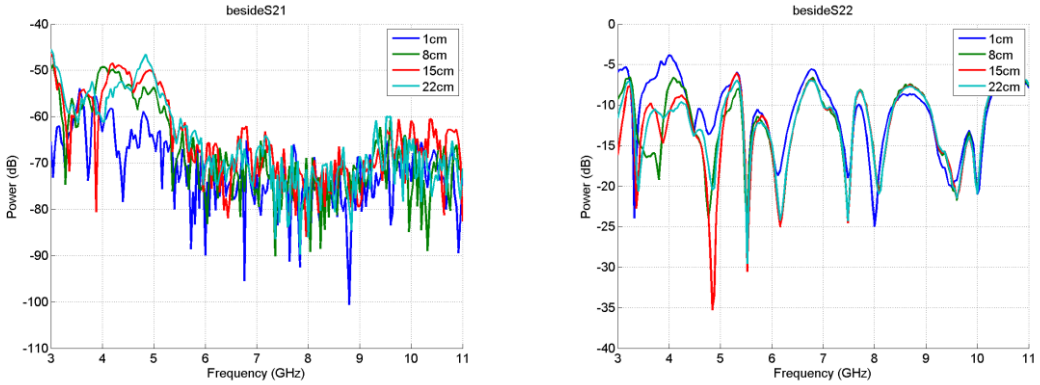

(b)

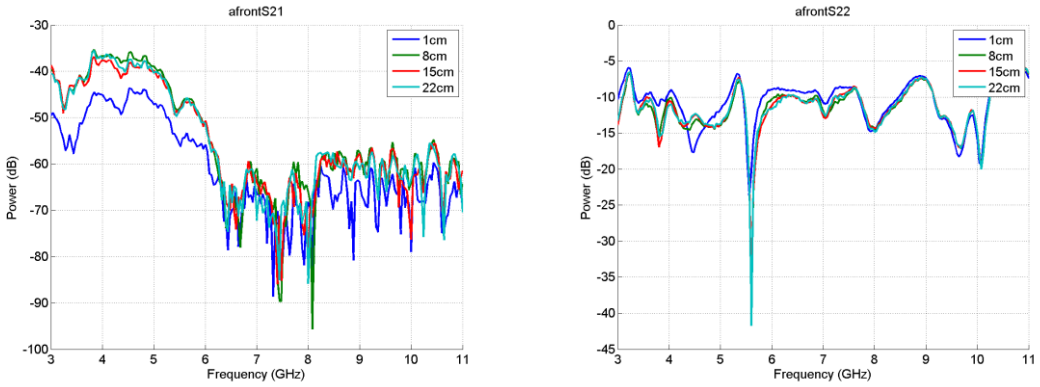

(c)

Figure 61: Off-body antennas, S_{12} (left) and S_{11} (right), at selected distances for three positions: (a) *p1*, (b) *p2* and (c) *p3*

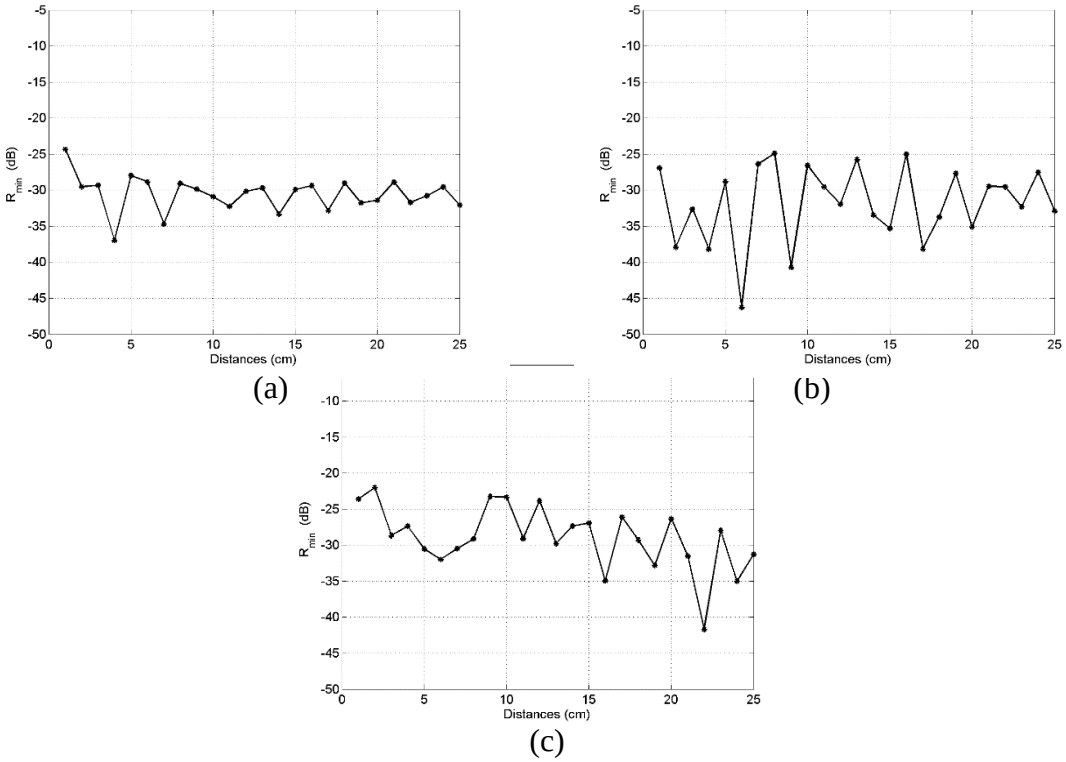

Figure 62: Minimum value of the S_{11} response with distance *d*, at position (a) *p1*, (b) *p2* and (c) *p3*

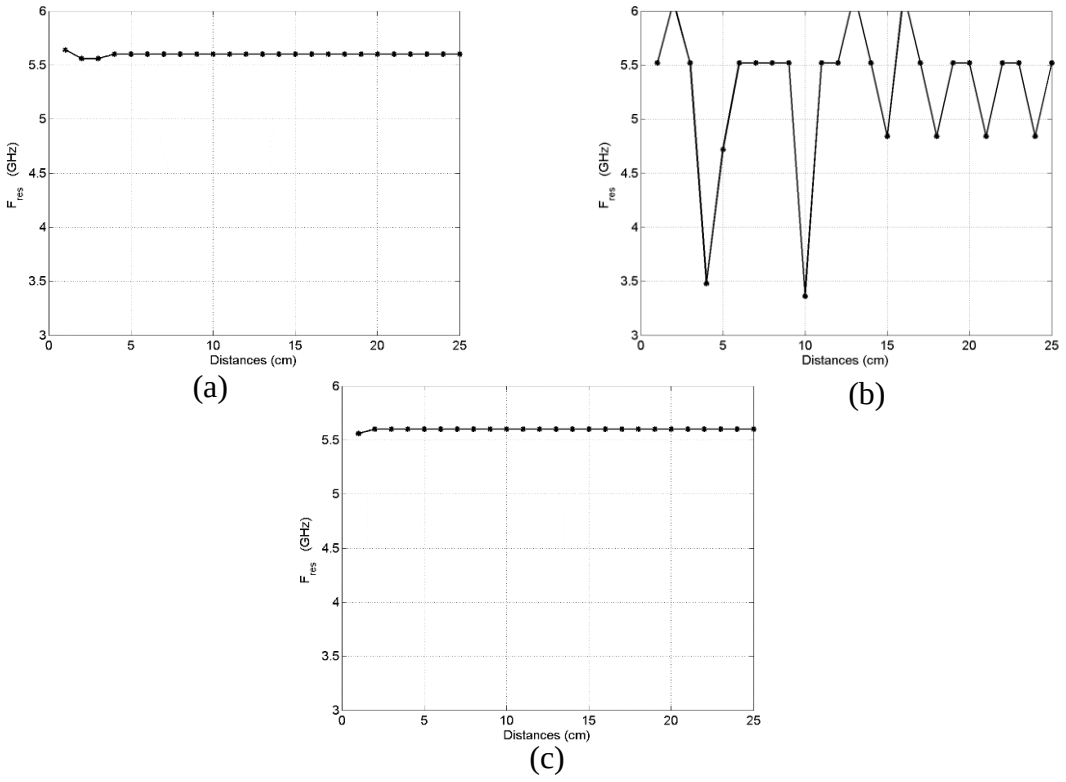

Figure 63: Frequency corresponding to the minimum value of S_{11} responses, at positions (a) *p1*, (b) *p2* and (c) *p3*

5.4 On-body Antenna Measurements

This section discusses the changes in an antenna's S-parameter when it comes into contact with the human body, as well as a metallic object, through several experiments. In these experiments, the proposed antenna was mounted on several parts of the human body and tested inside an anechoic chamber. The antenna diagrams shown in Chapter 4 are redrawn again in Figure 64 and Figure 65 for clarity. Both designs of the antenna, with a reflector or without a reflector, were used to investigate the benefits of the reflector in terms of sensitivity to the human body. Then a metallic object was introduced to the test setup in the near field of the antenna. Section 5.4.1 presents the test setup and results of the on-body test, while Section 5.4.2 presents the on-body antenna results when a metallic object is introduced.

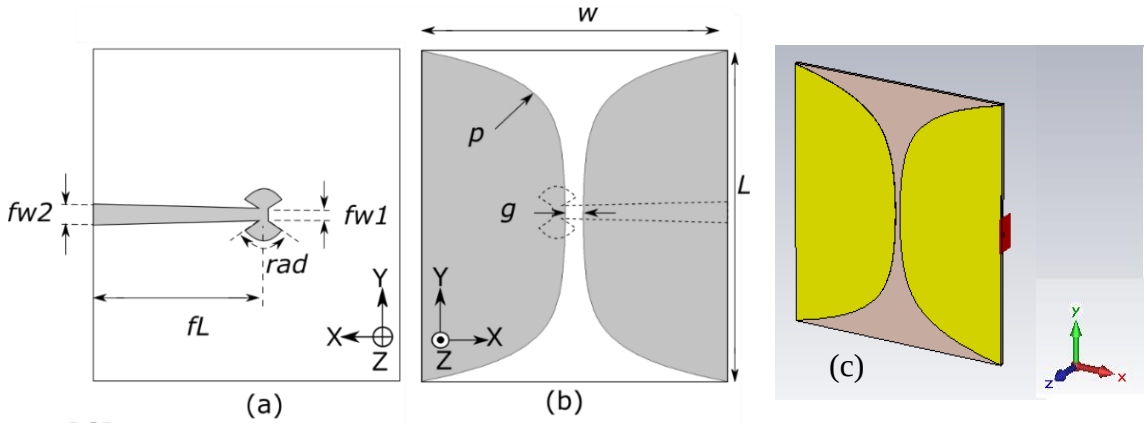

Figure 64: Proposed antenna without a reflector: (a) top, (b) bottom and (c) perspective view

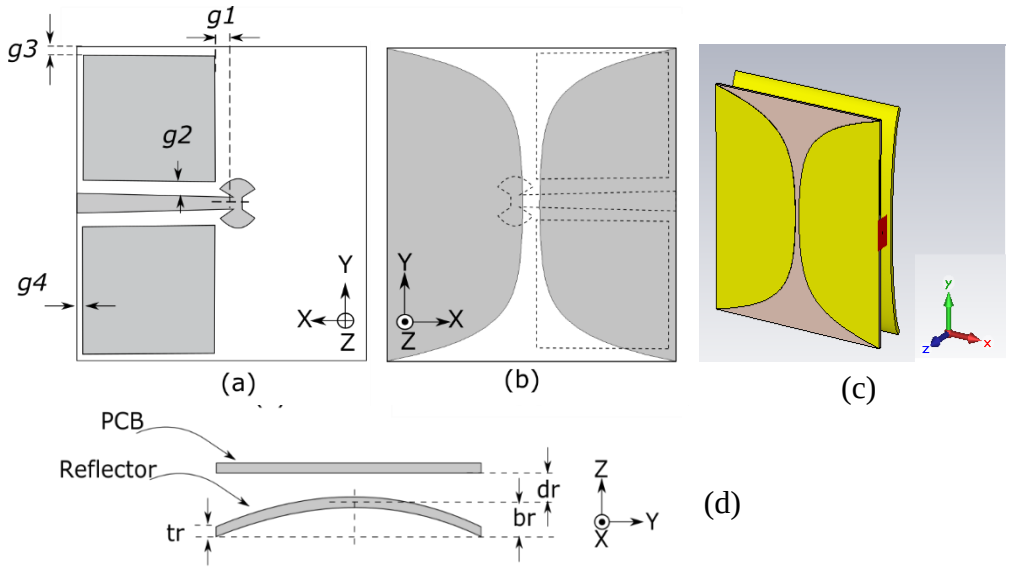

Figure 65: Proposed antenna with a reflector: (a) top, (b) bottom, (c) side and (d) perspective view

5.4.1 On-body Antenna Measurements without a Passive Object in the Near Field

In this test, two antennas were fixed inside an anechoic chamber, with a 2-m distance between them. One antenna was fixed on a wooden stand 1 m above the ground, while the other antenna was mounted on a human body, as shown in Figure 66. The test was repeated for several human body parts, as shown in Figure 67 and explained below:

- Free space: both antennas were fixed on a wooden stand (without the human body).
- On hand #1: antenna #1 was mounted on a human hand (near the wrist)
- On hand #2: antenna #1 was mounted on a human hand (near the wrist) and the volunteer was wearing a wrist watch on the same hand.
- On arm: antenna #1 was mounted on a human forearm (the region of the arm between the elbow and the wrist).
- On shoulder #1, #2 and #3: antenna #1 was mounted on a human shoulder at three different positions, as shown in Figure 67 (b).

In all of these locations, the antennas were placed face-to-face, except for shoulder #2 and shoulder #3, where the antenna was rotated with the human body. The whole test was repeated for the antenna design with reflector and without reflector.

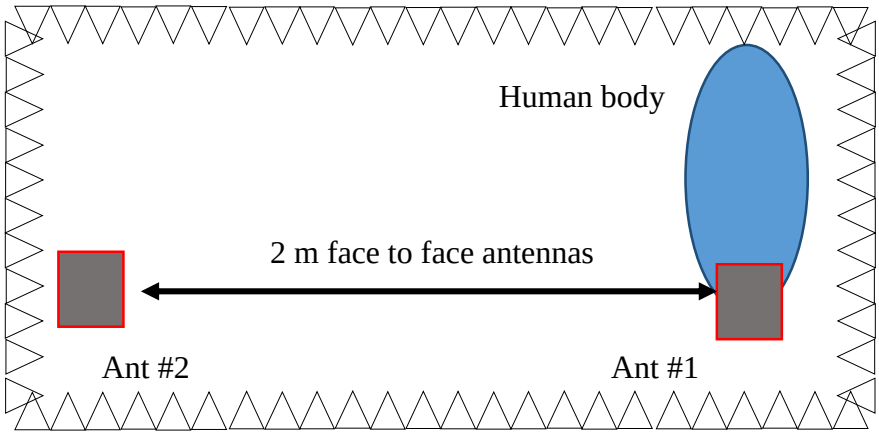

Figure 66: Top view of on-body test setup inside anechoic chamber

For simplicity, the experimental results were viewed in three groups; each group compares the antenna performance (with and without a reflector) at a subset of the locations specified above, as shown in the next three figures. Figure 68 compares the results of S_{11} and S_{12} at the following locations: On-hand#1, On-arm#2 and On-Shoulder#1. The figure shows that for an antenna with a reflector, the changes in the S_{11} responses at the three locations are trivial in most of the specified frequency range.

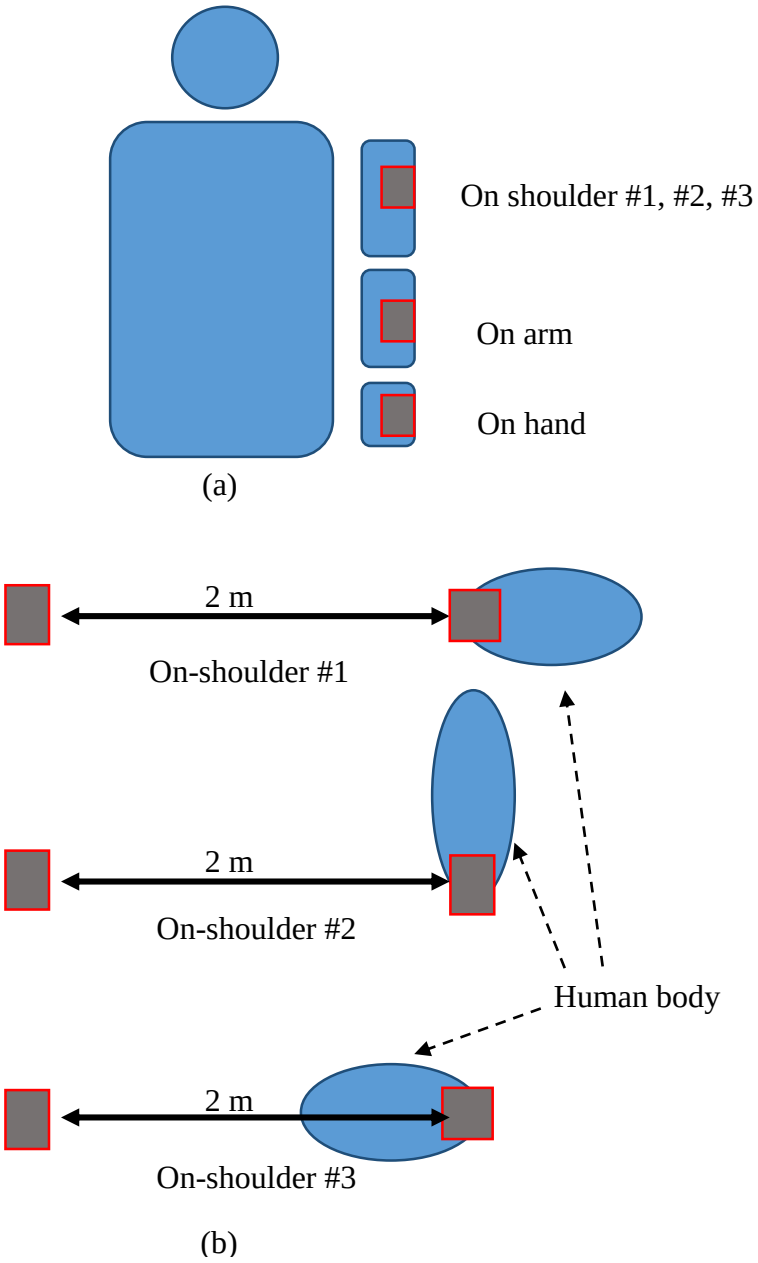

Figure 67: Antenna on body location: (a) the positions of the antennas on several body parts (b) three locations of on-shoulder test

On the other hand, the antenna with a reflector was highly affected by changes to the antenna's position on the human body. During the test with the antenna (without the reflector), it was noticed that the S_{11} responses change drastically, even with slight movement on the same location. This is due to the fact that the antenna feed line is placed directly on the skin; hence, its impedance varies, based on the variation of the contact area with skin. This also affects S_{12}, as can be seen in Figure 68 (b), where the S_{12} magnitude values in the low frequencies for the antenna without a reflector are smaller than those of the antenna with a reflector.

To measure the effect of metallic accessories (wristwatch) on the antenna behaviours, Figure 69 compares the results of S_{11} and S_{12} at the following locations: on-hand#1 and on-hand#2. The figure also compares the on-hand responses with a 'free space' case response. Results show that, for the antenna with a reflector, there is a large sensitivity to the metallic watch, as noticed from the S_{11} responses. Due to the relatively small size of the watch, this change is less than the change to the human body when compared to the free space case. However, for the antenna without a reflector, the change due to the metallic watch is very small (within 2 dB) compared to the human body.

Finally, Figure 70 compares the results of S_{11} and S_{12} at the three shoulder locations shown in Figure 67 (b). The S_{11} responses at on-shoulder#1 and on-shoulder#2 are similar, with insignificant changes. On the other hand, the S_{11} response for the antenna with a reflector at on-shoulder#3 showed larger changes than the other two shoulder locations. This is because the human body, at this position, blocks the signal completely. This can be seen clearly from Figure 70 (b) where the S_{12} response drops below -65 dB. For the antenna without a reflector, the difference in the S_{11} responses of the three positions is more than 5 dB for most of the specified frequency range.

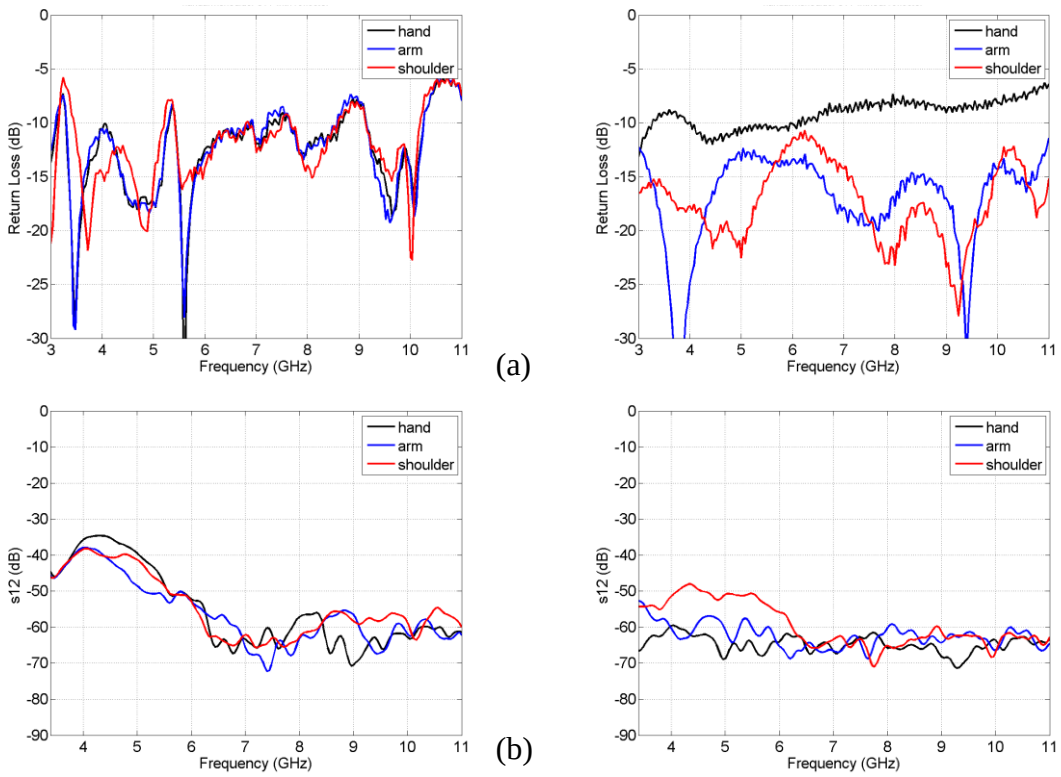

Figure 68: On-body test results (hand, arm and shoulder) for the antenna with a reflector (left) and without a reflector (right): (a) S_{11}, (b) S_{12}

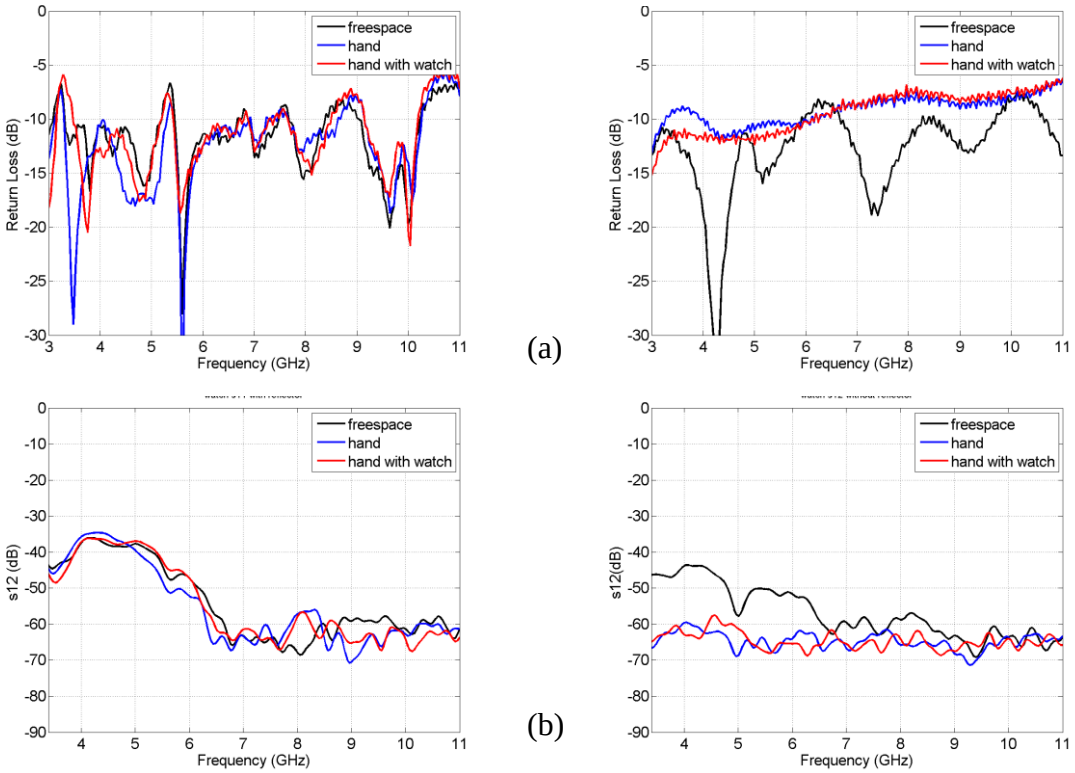

Figure 69: On-body test results (hand, hand with watch) for the antenna with a reflector (left) and without a reflector (right): (a) S_{11} and (b) S_{12}

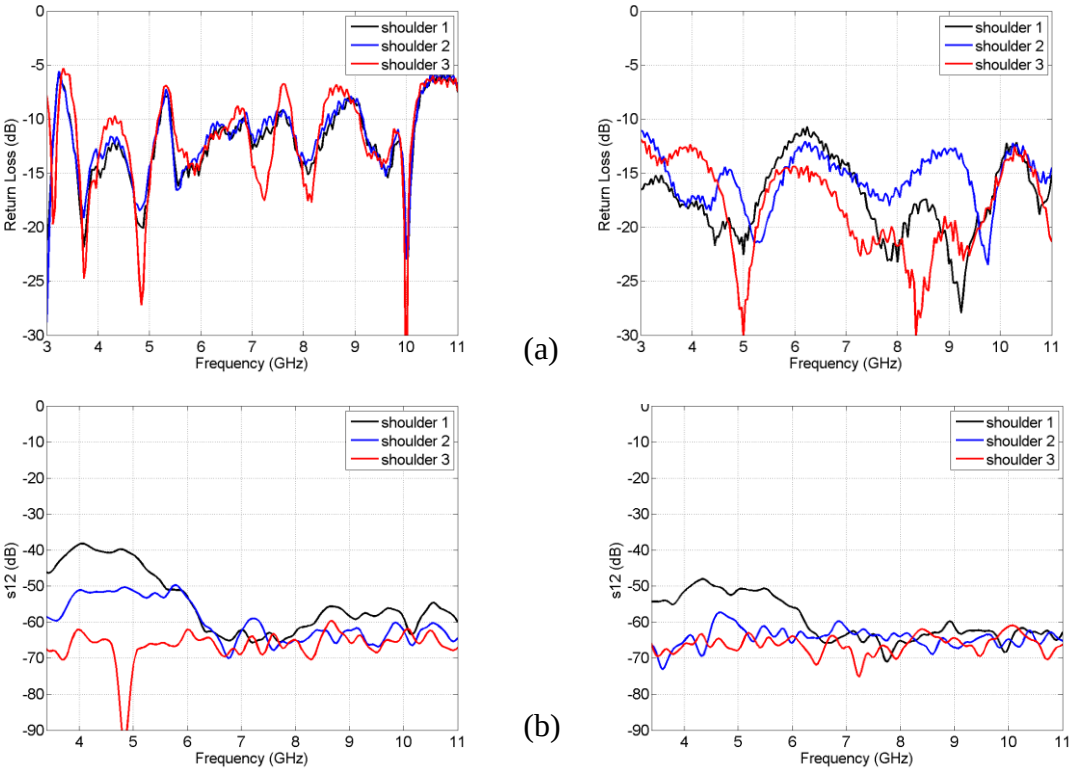

Figure 70: On-body test results (three shoulder positions) for the antenna with a reflector (left) and without a reflector (right): (a) S_{11} and (b) S_{12}

5.4.2 On-body Antenna Measurements with a Passive Object in the Near Field

This section presents the setup and measurements of an antenna under the effect of both the human body and a metallic object. The test setup is similar to the one described in the previous section, with some variations. Antenna#1 was mounted on only one body part (on arm), and a metallic plate (size 30 cm × 20 cm) was introduced, as shown in Figure 71. The antennas were placed face-to-face, while the metallic plate was placed beside antenna#1. The distance between antenna#1 and the metallic plate (named *d*) was varied from 1 cm to 25 cm, at a step of 1 cm. At each step, the s-parameters of the antenna were measured and recorded. The whole test was repeated twice, for the antenna design with a reflector and without a reflector.

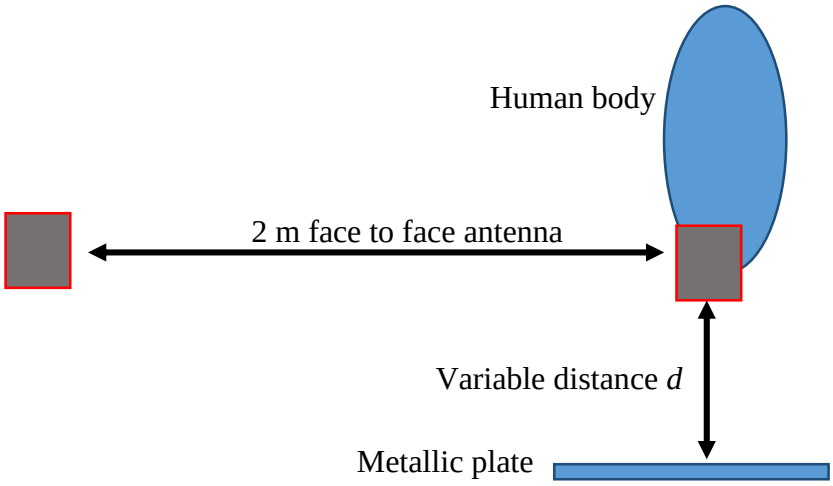

Figure 71: Layout (top view) of on-body test with metallic object

Figure 72 shows the responses of S_{11} and S_{12} at selected distances for both the antenna with a reflector and without reflector, while Figure 73 shows the responses for all of the 25 steps. As can be seen in Figure 72, the change in distance *d* caused a change in the response of S_{11}. For the antenna with a reflector, the change is within 5 dB and appears mostly at the resonant frequencies of the S_{11} response at 3.5 GHz, 5.5 GHz and 8 GHz. For the antenna without a reflector, the change is higher; it is around 5db in most of the responses and more than 10 dB in the resonant frequencies regions. The next section presents the details of the feature extraction methods, to quantify these changes.

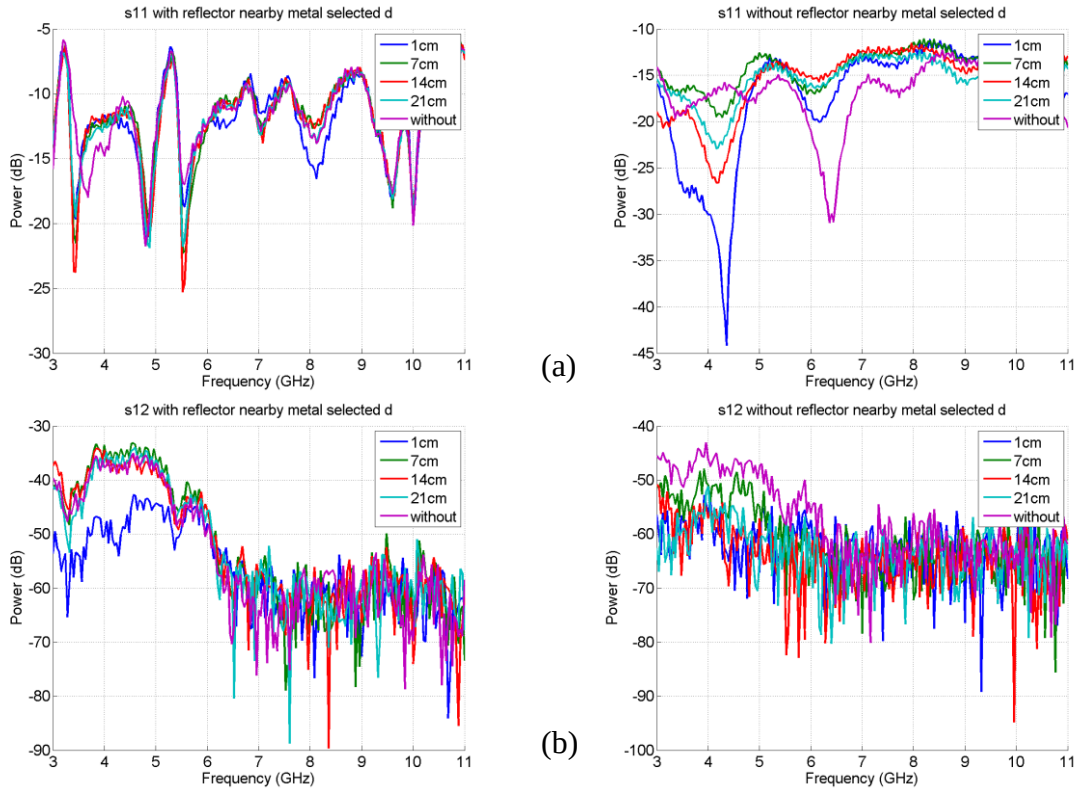

Figure 72: On-body test results with a metallic object at selected distances, for the antenna with a reflector (left) and without a reflector (right): (a) S_{11} and (b) S_{12}

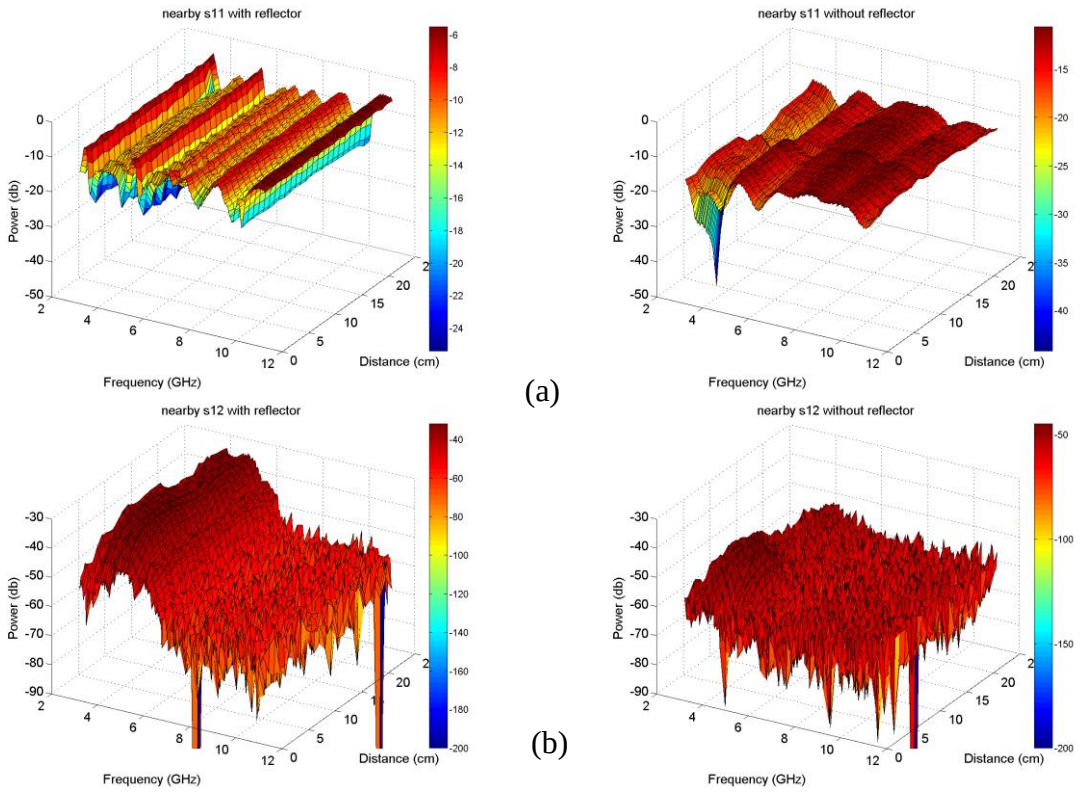

Figure 73: On-body test results with a metallic object, for the antenna with a reflector (left) and without a reflector (right): (a) S_{11} and (b) S_{12}

5.5 Proposed indicators for object detection near an on-body antenna

This section proposes two methods that relate the change in the s-parameter response to distance *d*, between the antenna and the metallic object within the antenna near field. Using the data presented in Section 5.4.2, two features are proposed: *root-mean-square* and *peak-to-peak*. The *root-mean-square* feature at distance *d* is calculated as follows:

$$diff^d = S^d - S^{freespace}, \tag{44}$$

$$rms^d = root\_mean\_square\,(diff^d), \tag{45}$$

where S^d is the S-parameter response (S_{11} or S_{12}) when the metallic plate is at distance *d*, and $S^{freespace}$ is the S-parameter response when the metallic plate is not presented.

The *peak-to-peak* feature at distance *d* is calculated as follows:

$$p2p^d = max(diff^d) - min(diff^d). \tag{46}$$

Figure 74 shows the values of the *root-mean-square* feature of the S_{11} response, plotted at each distance step for the antenna design with and without a reflector. In the figure, the dots represent the calculated rms_{11} values, while the line represents the fitted data. For the antenna design with a reflector, the value of the rms_{11} feature stays relatively constant at distances less than 10 cm, then the value starts to decrease monotonically with the distance. On the other hand, the *rms* feature does not show a direct relation to distance change for the antenna without reflector. Similarly, the values of the *peak-to-peak* feature of the S_{11} response (shown in Figure 75) show a monotonic decrease in the feature value, with an increase of distances above 10 cm for the design with a reflector, as compared with the design without a reflector. For the S_{12} results, equations (1) - (3) were also applied to the S_{12} responses at each distance step, to calculate rms_{12} and $p2p_{12}$; this is shown in Figure 76. However, the results show the change in the S_{12} features that is not directly related to the change in distance *d*, for the antenna with reflector and without reflector.

In conclusion, the results show that the rms_{11} and $p2p\_{11}$ feature provide indicators for the object existence near an on-body antenna for distances above 10 cm when the reflector is used. Further analysis of the data is presented in next section to classify the nearby object and distinguish between the human body and a metallic object.

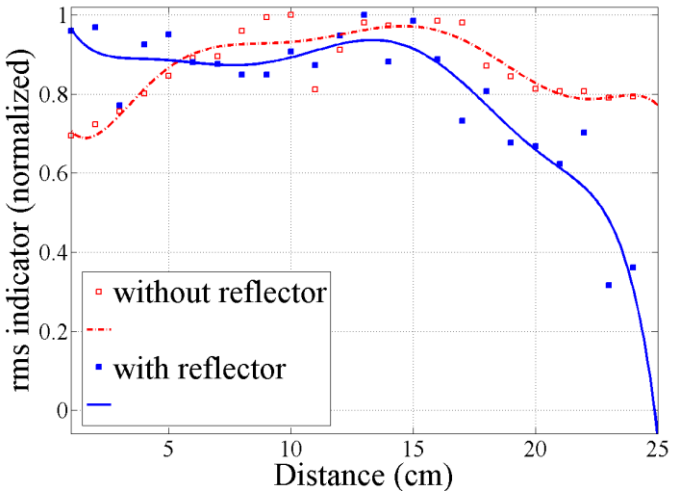

Figure 74: *rms* feature for S_{11} vs distance *d*

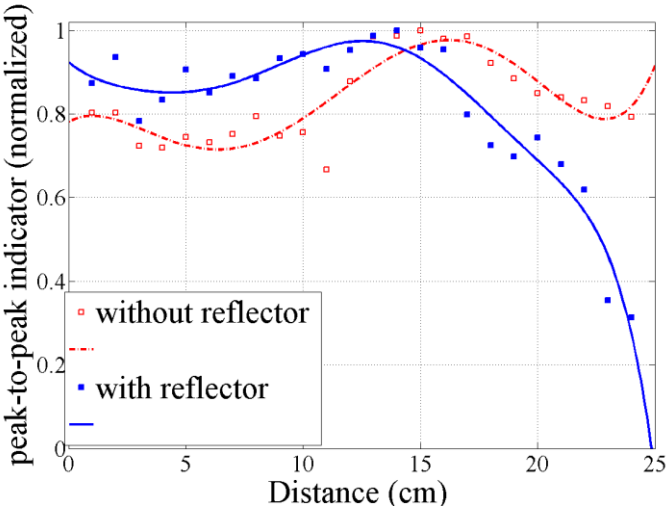

Figure 75: *peak-to-peak* feature for S_{11} vs distance *d*

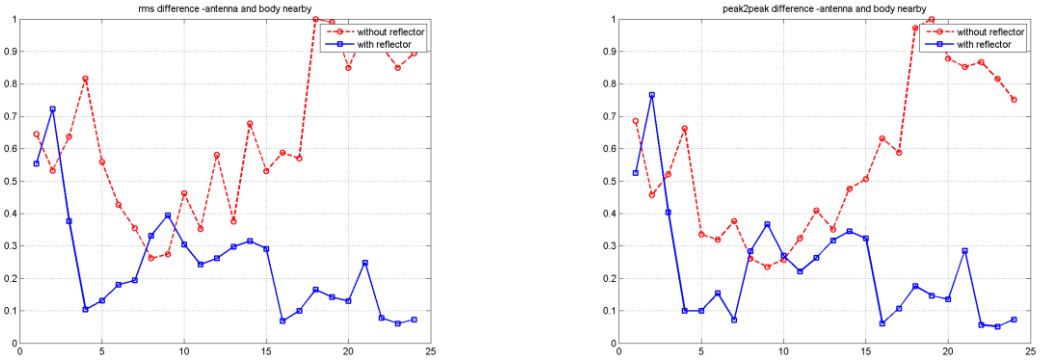

Figure 76: S_{12} features vs distance *d*: (a) *rms* and (b) *peak-to-peak*

5.6 Classification methodology and results for on-body tests

To apply the PCA, data should be arranged in an $n \times m$ matrix, where n is the number of observations and m is the number of variables. The analysis in this section uses the experimental measurements obtained in Section 5.4. The experimental measurements were arranged as 32 observations. The first 25 observations represented measurements for the 25 locations in the experiment, i.e., 25 distance steps. The next 7 measurements were taken on the human body without a metal plate. Each observation involved the aggregated frequency responses of the S_{11} magnitude, S_{11} phase, S_{12} magnitude and S_{12} phase in a single vector, representing the *variables*. As previously described, each frequency contains 201 steps from 3GHz to 11GHz; hence, each *observation* will contain 4×201 *variables*. This classifies the dimension of the data matrix as 32×804.

Figure 77 and Figure 78 show the classification of an object or antenna location, based on the first two principal components, PC1 and PC2, for the antenna with or without a reflector. Each marker in the figure represents a single *observation* in which the metallic object or the antenna is placed at a different location. The marker shape represents a different measurement.

For the antenna with a reflector, the results in Figure 77 clearly show the ability of the antenna to detect a nearby object. The blue markers (O) in the lower left side of the figure represent on-body measurements with nearby metallic objects. The black markers (∇) in the upper left represent the on-body measurements without a metallic object on several body parts. From the figure, it can be seen that the free space case, where the antenna was tested without a human body or metallic object, appears within the other cases of on-body antennas and far from the cases of metallic objects. However, there are two exceptions in this classification. The first is the case that represents the location of on-hand#2, where the antenna is placed on hand with a metallic watch. In this case, the corresponding marker (∇3) appears next to the blue markers, which emphasises the antenna's ability to detect metallic objects. The second exception is the case that represents the on-shoulder#3 location, where the antenna is placed on the shoulder and the body was on the line-of-sight between the two antennas. Due to the large change in the S_{12} response, the corresponding marker appears on the far right side of the figure, yet it is separated from the blue markers.

On the other hand, Figure 78 shows the classification results for the antenna without a reflector. As can be shown in the figure, the markers corresponding to cases with and without a metallic object are scattered in the figure and cannot be classified.

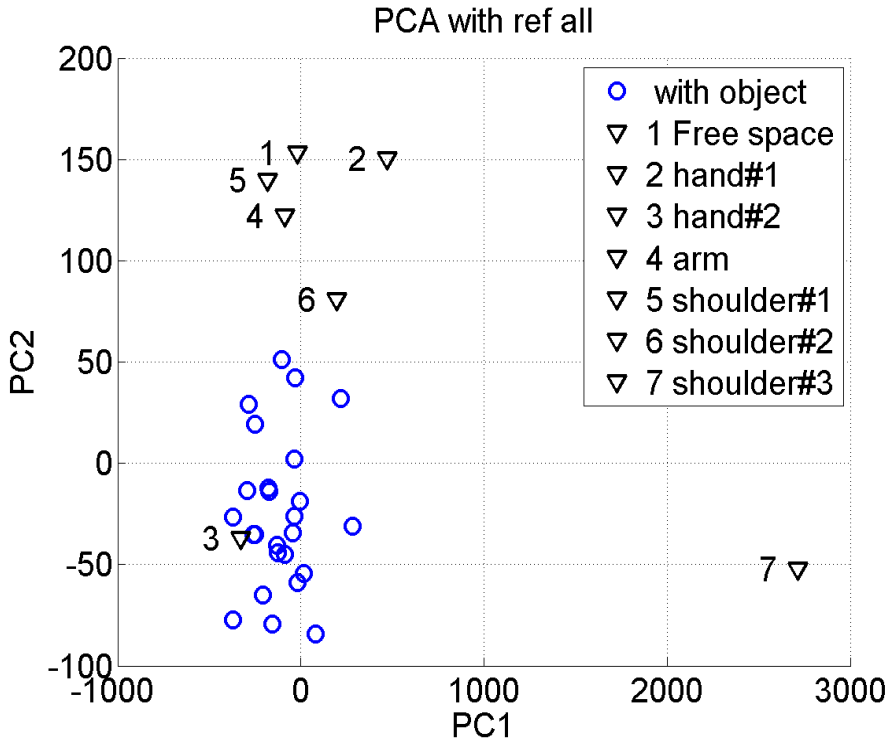

Figure 77: PCA classification for the antenna with a reflector

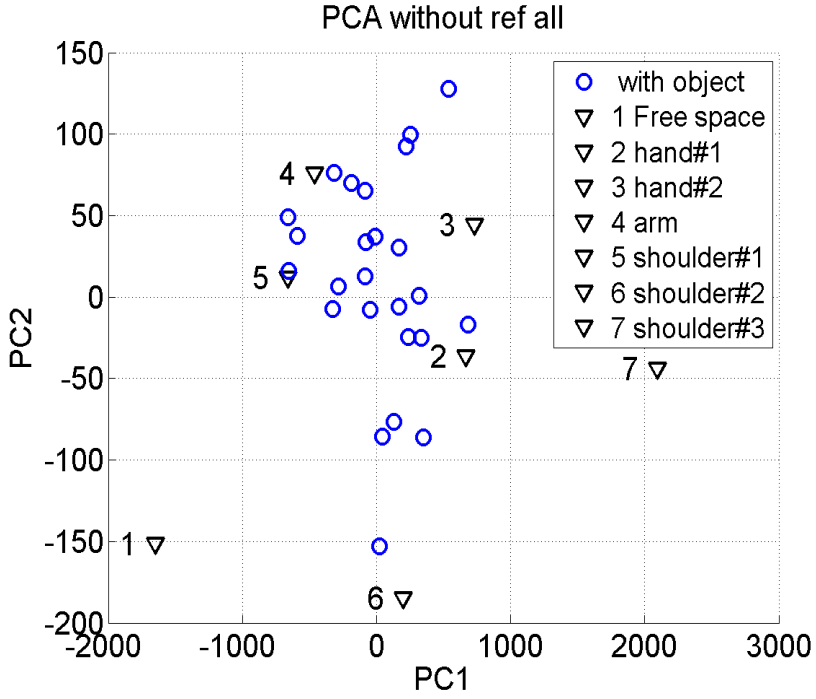

Figure 78: PCA classification for the antenna without a reflector

5.7 Summary

This chapter presented a study of nearby objects and their effect in the near field of the WBAN antenna on the antenna measurements and how these effects can be used to sense and detect the objects. First, an experimental setup was presented to study the metallic object effects on an off-body UWB antenna inside an anechoic chamber, where the antenna proposed in Chapter 4 was used. Then, a similar experimental setup was carried out, but for on-body measurements, where the antenna was mounted on a human body's hand, arm and shoulder. In each case, the antenna's S-parameters were recorded and compared for the antenna with a reflector and without a reflector. Later, a metallic object was introduced to the on-body test setup at several distances from the antenna. The results show that, for the antenna with a reflector, the change in the antenna reflection coefficient, due to placing it on several body parts, is within a few dB. However, for the antenna without a reflector, the antenna reflection coefficient, as well as the transmission coefficient, was highly sensitive to contact with the human body. The average change in the reflection coefficient at several body locations is larger than 5 dB. Based on the results of the on-body test with a metallic object, two features were proposed (*root-mean-square* and *peak-to-peak*) to draw a relation between the change in the reflection coefficient magnitude and the distance between the metallic object and the on-body antenna. Both features show a monotonic decrease in value as the metallic object distance increased beyond 10 cm from the antenna. Moreover, a principal component analysis classifier was used to classify the on-body measurements with and without metallic objects, and the results showed the superiority of the antenna design with a reflector over the design without a reflector.

In conclusion, the results prove the ability of the WBAN UWB antenna to detect nearby objects with the suggested features. Also, the reflector not only reduced the antenna's sensitivity to humans, but enhanced its ability to detect the objects.

Chapter 6 CONCLUSIONS AND FUTURE WORK

6.1 Conclusions

The near-field interaction between wearable devices and the surrounding objects, especially indoor environments, is an inevitable challenge and drastically affects the network function. The changes in the antenna impedance due to coupling with a nearby object is significant within the antenna near field, and these changes can be used as indicators for passive objects presence. Through an analysis of the changes in the antenna reflection coefficient, these objects can be detected and their distance to the antenna can be estimated within the near field. This thesis proposed and described techniques to sense passive objects nearby WBAN node to improve the interaction between WBAN and its surrounding environment, through the analysis of node's antenna measurements and proposed an antenna design for this purpose.

6.1.1 Near Field Sensing and WBAN State of the Art

The review of recent literature in WBAN showed the importance of nearfield sensing based on antenna measurements and its role in many applications. The literature review showed an increase interest in using the antennas as sensors in several applications, e.g. gesture recognition and localization. Although the channel modelling of a wireless body area network has been an active topic for researchers in recent years, the effects of near-field interaction of WBAN with passive objects are not fully addressed. Many applications use physical-level measurements, such as received signal strength and link quality indicator, to gain knowledge about changes in the surrounding environment, yet these measurements become totally distorted in the case of near-field interferer. On the other hand, adding sensors, such as cameras or a proximity sensor, are a straightforward solutions to enhance the interaction between WBAN with its surrounding, yet these solutions complicate the WBAN node design and increases its cost. On the other hand the review showed lack in the studies of interaction between WBAN and surrounding passive object. This leaves a gap for research in the area of antenna design and near field interaction with passive object as well as the inherit interaction with the human body.

6.1.2 Off-Body Near Field Sensing Using Low Profile Antenna

The focus of this stage was to study and analyse the changes in the reflection coefficient of a low profile antenna due to the existence of a metallic, passive object within the antenna near field. For this purpose, tests were conducted inside an anechoic chamber

using a low profile, narrow band, dipole antenna. During the tests, a metallic plate was placed within the antenna near the field at several distances, whereas the antenna itself was connected to a network analyser, which captured the antenna's reflection and transmission coefficients. By analysing the data from the reflection coefficients with a metallic object at several distances from the antenna, the change in antenna return loss value and frequency were found to be related to the distance to the metallic object. Then, a direct relation between the distances to the antenna return loss was concluded. Furthermore, the object's location, relative to two communicating low profile antennas, was detected, using both reflection and transmission coefficients. The magnitude and phase values of both coefficients for different setups were fed to a PCA classifier. Results showed the classifier's ability to classify the object's location into roughly three groups relative to the line of sight. Although the experiments were done in free space, without human interference, they signifies the low profile antenna capabilities in sensing and detecting nearby objects.

6.1.3 Antenna Design and On-Body Near Field Sensing

Following to the two previous steps, a design for a WBAN antenna was proposed, with the purpose of achieving low back radiation while maintaining a low profile. The antenna was based on the widely used Vivaldi antenna, and it was modified to achieve the radiation pattern that matches WBAN requirements. The modification involves adding a reflector to both reduce the antenna sensitivity and enhance the radiation pattern. However, adding a reflector also reduces the antenna's total efficiency at higher frequencies. The antenna was optimized in simulation, then it was implemented and tested inside and anechoic chamber. When the antenna is then tested on several body parts, the results show very slight changes in the antenna reflection and transmission coefficient values, compared to the initial test values in free space. More interestingly, the reflector not only reduced the antenna coupling with the human body, but also enhanced its sensitivity to the nearby object. This was shown through a set of experiments inside an anechoic chamber; the proposed antenna was fixed on several body parts, with and without a reflector, while a metallic object was placed near the antenna. Two indicators were proposed to detect the object distance to the antenna, based on the root mean square and the peak to peak difference of the changes in the reflection coefficient. The results show that the proposed antenna with the reflector is more sensitive to change in nearby object distances within the near field, compared with the design without a reflector.

Finally, when the classifier was applied, it showed the ability of the design to detect nearby objects, even when it was fixed on the human body. Both the antenna design and the proposed features showed the feasibility of using low profile antenna to clearly sense the passive object presence within the antenna near field and estimate its distance to the antenna in WBAN.

6.2 Future Work

The results of this research project are promising towards using the low profile antenna's measurements to enhance the interaction between a WBAN node and its surroundings. As stated above, near-field sensing in WBAN is very important, yet it is a niche research area, except for a few recent attempts. Hence, it is difficult to cover all the aspects of this system in order to address all of its challenges in one thesis. For future work, there are several directions for further development and improvement of the current work, as listed below.

1. In the current study, only two types of antenna were used: a commercial, narrow band, dipole antenna and the proposed wideband antenna. Analysis of the changes in antenna measurements is still required for other types of antenna, e.g. textile antenna [144, 145] and fractal antenna [146, 147]. This is necessary to obtain a wider view of the relation between near field sensing and the antenna type and generalizing the concept of near field sensing in WBAN applications.
2. Although the effects of the object shape on the results were discussed in the thesis, only metallic material (perfect electric conductor) was considered. Moreover, the tests only focused on detecting the object existence and distance to the antenna but not detecting its material. Future work based on this thesis should pay attention to the object material and its effects on the near field sensing process. Objects that are typically exist in indoor environments and interact with WBAN are expected to be made of a mix of several materials e.g. metallic and dielectric. By examining different types of object material, the proposed methods can be applied for not only wearable body sensor networks, but also robot-based sensors networks [87] for harsh environments where a lot of metallic and non-metallic objects e.g. pipes and containers are presented.
3. The signals used in this thesis experiments were applied by the network analyser as a continuous Gaussian sinusoidal wave for the specified frequency range. Future

work for the near field sensing should consider using a modulated signal that carries actual data as it normally transmitted in typical WBAN communication. This step will assure the agility of near field sensing concept as the WBAN node will sense its surrounding while having an ongoing transmission with other nodes. It also guarantee the compatibility with the current communication protocols since it doesn't require a special transmission mode for sensing. Commercially, several types of advanced network analysers are available, which can provide S-parameter measurements, using a modulated signal.

4. During the analysis of the reflection coefficient of the proposed antenna, the measured changes in frequency domain were less than the changes in the case of the narrow band antenna. This is due to the resolution of the recorded data, since the proposed antenna's response was recorded over a wider frequency band. Finer measurements of the UWB will give more useful features to sense nearby objects, e.g. monitoring single resonant frequency within the UWB. This can be achieved by select and analyse specific parts of the frequency response of the UWB measurements instead of processing the whole range.
5. In this work, the proposed features and data analysis were based on antenna measurements obtained only in the frequency domain. Many current WBAN applications depend on impulse radio transmission for various purposes. Examination of the effects of passive objects on the WBAN antenna in time domain, is necessary to extend the near field sensing concept to those types of applications [148].

References

[1] K. M. S. Thotahewa, J.-M. Redouté, and M. R. Yuce, *Ultra Wideband Wireless Body Area Networks*: Springer, 2014.

[2] K. Nikita, "Antennas and RF Communication," in *Handbook of Biomedical Telemetry*, ed: Wiley-IEEE Press, 2014, pp. 1-736.

[3] G. Yang, *Body sensor networks*: Second Edition, Springer-Verlag London, 2014.

[4] M. Ilyas and I. Mahgoub, *Handbook of sensor networks: compact wireless and wired sensing systems*: CRC press, 2004.

[5] K. Cheng-Hung, W. Sung-Jung, and T. Jenn-Hwan, "A Novel Folded UWB Antenna for Wireless Body Area Network," *IEEE Trans. Antennas and Propag.*, vol. 60, pp. 1139-1142, 2012.

[6] M. Koohestani, J. F. Zurcher, A. A. Moreira, and A. K. Skrivervik, "A Novel, Low-Profile, Vertically-Polarized UWB Antenna for WBAN," *IEEE Trans. Antennas and Propag.*, vol. 62, pp. 1888-1894, 2014.

[7] E. E. Lopez Canelon, A. Garcia Loapez, R. Chandra, and A. J. Johansson, "3D printed miniaturized UWB antenna for wireless body area network," in *Antennas and Propagation (EuCAP), 2014 8th European Conference on*, 2014, pp. 3090-3093.

[8] N. Chahat, M. Zhadobov, R. Sauleau, and K. Ito, "A Compact UWB Antenna for On-Body Applications," *IEEE Trans. Antennas and Propag.*, vol. 59, pp. 1123-1131, 2011.

[9] D. L. Paul, H. Giddens, M. G. Paterson, G. S. Hilton, and J. P. McGeehan, "Impact of Body and Clothing on a Wearable Textile Dual Band Antenna at Digital Television and Wireless Communications Bands," *Antennas and Propagation, IEEE Transactions on*, vol. 61, pp. 2188-2194, 2013.

[10] H. Baldus, S. Corroy, A. Fazzi, K. Klabunde, and T. Schenk, "Human-centric connectivity enabled by body-coupled communications," *Communications Magazine, IEEE*, vol. 47, pp. 172-178, 2009.

[11] G. Koutitas, "Multiple Human Effects in Body Area Networks," *Antennas and Wireless Propagation Letters, IEEE*, vol. 9, pp. 938-941, 2010.

[12] M. Koohestani, N. Pires, A. K. Skrivervik, and A. A. Moreira, "Performance Study of a UWB Antenna in Proximity to a Human Arm," *Antennas and Wireless Propagation Letters, IEEE*, vol. 12, pp. 555-558, 2013.

[13] A. M. Eid and J. W. Wallace, "Accurate Modeling of Body Area Network Channels Using Surface-Based Method of Moments," *Antennas and Propagation, IEEE Transactions on,* vol. 59, pp. 3022-3030, 2011.

[14] S. H. Kvist, J. Thaysen, and K. B. Jakobsen, "Ear-to-Ear On-Body Channel Model for Hearing Aid Applications," *Antennas and Propagation, IEEE Transactions on,* vol. 63, pp. 344-352, 2015.

[15] W. Qiong, T. Tayamachi, I. Kimura, and W. Jianqing, "An On-Body Channel Model for UWB Body Area Communications for Various Postures," *Antennas and Propagation, IEEE Transactions on,* vol. 57, pp. 991-998, 2009.

[16] H. Sang-Hun and P. Sang Kyu, "Performance analysis of wireless body area network in indoor off-body communication," *Consumer Electronics, IEEE Transactions on,* vol. 57, pp. 335-338, 2011.

[17] A. Chunsu, A. Byoungjik, K. Sunwoo, and C. Jaehoon, "Experimental outage capacity analysis for off-body wireless body area network channel with transmit diversity," *Consumer Electronics, IEEE Transactions on,* vol. 58, pp. 274-277, 2012.

[18] X. Wu, Y. I. Nechayev, C. C. Constantinou, and P. S. Hall, "Interuser Interference in Adjacent Wireless Body Area Networks," *Antennas and Propagation, IEEE Transactions on,* vol. 63, pp. 4496-4504, 2015.

[19] I. Khan, Y. I. Nechayev, K. Ghanem, and P. S. Hall, "BAN-BAN Interference Rejection With Multiple Antennas at the Receiver," *Antennas and Propagation, IEEE Transactions on,* vol. 58, pp. 927-934, 2010.

[20] K. Ghanem, "Effect of Channel Correlation and Path Loss on Average Channel Capacity of Body-to-Body Systems," *Antennas and Propagation, IEEE Transactions on,* vol. 61, pp. 6260-6265, 2013.

[21] B. Jung Nam, C. Young Hoon, K. Jin Young, K. Jang Woo, and K. Dong In, "Efficient interference cancellation scheme for wireless body area network," *Communications and Networks, Journal of,* vol. 13, pp. 167-174, 2011.

[22] A. L. Martens, P. Slottje, M. Y. Meima, J. Beekhuizen, D. Timmermans, H. Kromhout, *et al.*, "Residential exposure to RF-EMF from mobile phone base stations: Model predictions versus personal and home measurements," *Science of The Total Environment,* vol. 550, pp. 987-993, 4/15/ 2016.

[23] N. Decarli, F. Guidi, and D. Dardari, "A Novel Joint RFID and Radar Sensor Network for Passive Localization: Design and Performance Bounds," *Selected*

Topics in Signal Processing, IEEE Journal of, vol. 8, pp. 80-95, 2014.

[24] A. Argyriou, A. Caballero Breva, and M. Aoun, "Optimizing Data Forwarding from Body Area Networks in the Presence of Body Shadowing with Dual Wireless Technology Nodes," *Mobile Computing, IEEE Transactions on,* vol. 14, pp. 632-645, 2015.

[25] M. Kim and J. I. Takada, "Characterization of Wireless On-Body Channel Under Specific Action Scenarios at Sub-GHz Bands," *Antennas and Propagation, IEEE Transactions on,* vol. 60, pp. 5364-5372, 2012.

[26] S. Swaisaenyakorn, S. W. Kelly, and J. C. Batchelor, "A Study of Factors Affecting Wrist Channel Characteristics for Walking Postures Using Motion Capture," *Antennas and Propagation, IEEE Transactions on,* vol. 62, pp. 2231-2237, 2014.

[27] A. Hyo-Sung and Y. Wonpil, "Environmental-Adaptive RSSI-Based Indoor Localization," *Automation Science and Engineering, IEEE Transactions on,* vol. 6, pp. 626-633, 2009.

[28] T. Sheng-Yuan, C. Kwang-Cheng, and R. Prasad, "Spectrum Sensing of OFDMA Systems for Cognitive Radio Networks," *Vehicular Technology, IEEE Transactions on,* vol. 58, pp. 3410-3425, 2009.

[29] F. Guidi, A. Sibille, and C. Roblin, "Interaction of UWB Tag Backscattering With Close Metallic Reflectors," *Antennas and Wireless Propagation Letters, IEEE,* vol. 13, pp. 245-248, 2014.

[30] L. Xiao zheng, X. Zeming, and C. Xuanliang, "A Compact RFID Reader Antenna for UHF Near-Field and Far-Field Operations," *International Journal of Antennas and Propagation,* vol. 2013, p. 5, 2013.

[31] Q. Xianming and C. Zhi Ning, "Proximity Effects of Metallic Environments on High Frequency RFID Reader Antenna: Study and Applications," *Antennas and Propagation, IEEE Transactions on,* vol. 55, pp. 3105-3111, 2007.

[32] Q. H. Abbasi, M. M. Khan, S. Liaqat, M. Kamran, A. Alomainy, and Y. Hao, "Experimental investigation of ultra wideband diversity techniques for on-body radio communications," *Progress In Electromagnetics Research C,* vol. 34, pp. 165-181, 2013.

[33] Q. H. Abbasi, M. U. Rehman, H. T. Chattha, K. Qaraqe, A. Alomainy, H. Yang, *et al.*, "Ultra wideband antenna diversity characterisation for off-body communications in an indoor environment," *Microwaves, Antennas &*

Propagation, IET, vol. 8, pp. 1161-1169, 2014.

[34] K. Li, N. Ahmed, S. S. Kanhere, and S. Jha, "Reliable transmissions in AWSNs by using O-BESPAR hybrid antenna," *Pervasive and Mobile Computing*.

[35] W. Wei and Z. Qian, "Toward long-term quality of protection in mobile networks: a context-aware perspective," *Wireless Communications, IEEE,* vol. 22, pp. 34-40, 2015.

[36] L. Bin, Y. Zhisheng, and C. Chang Wen, "MAC protocol in wireless body area networks for E-health: challenges and a context-aware design," *Wireless Communications, IEEE,* vol. 20, pp. 64-72, 2013.

[37] Tobo, x, D. P. n, T. H. Falk, and M. Maier, "Context awareness in WBANs: a survey on medical and non-medical applications," *Wireless Communications, IEEE,* vol. 20, pp. 30-37, 2013.

[38] R. M. Vaghefi, M. R. Gholami, R. M. Buehrer, and E. G. Strom, "Cooperative Received Signal Strength-Based Sensor Localization With Unknown Transmit Powers," *Signal Processing, IEEE Transactions on,* vol. 61, pp. 1389-1403, 2013.

[39] M. R. Gholami, R. M. Vaghefi, and E. G. Strom, "RSS-Based Sensor Localization in the Presence of Unknown Channel Parameters," *Signal Processing, IEEE Transactions on,* vol. 61, pp. 3752-3759, 2013.

[40] C. A. Balanis, *Antenna Theory: Analysis and Design*: John Wiley & Sons, 2005.

[41] T. S. Rappaport, *Wireless Communications: Principles and Practice*: Prentice Hall PTR, 2002.

[42] W. L. Stutzman and G. A. Thiele, *Antenna Theory and Design*: Wiley, 2012.

[43] T. Prakoso, R. Ngah, Z. Ghassemlooy, and T. A. Rahman, "Antenna representation in two-port network scattering parameter," *Microwave and Optical Technology Letters,* vol. 53, pp. 1404-1409, 2011.

[44] M. I. Sobhy, B. Sanz-Izquierdo, and J. C. Batchelor, "System and Circuit Models for Microwave Antennas," *Microwave Theory and Techniques, IEEE Transactions on,* vol. 55, pp. 729-735, 2007.

[45] J. T. Aberle, "Two-Port Representation of an Antenna With Application to Non-Foster Matching Networks," *Antennas and Propagation, IEEE Transactions on,* vol. 56, pp. 1218-1222, 2008.

[46] C. C. Y. Poon, B. P. L. Lo, M. R. Yuce, A. Alomainy, and H. Yang, "Body Sensor Networks: In the Era of Big Data and Beyond," *Biomedical Engineering, IEEE Reviews in,* vol. 8, pp. 4-16, 2015.

[47] K. Nikita, "Intrabody Communication," in *Handbook of Biomedical Telemetry*, ed: Wiley-IEEE Press, 2014, pp. 1-736.

[48] "IEEE Standard for Information technology--Telecommunications and information exchange between systems Local and metropolitan area networks--Specific requirements Part 11: Wireless LAN Medium Access Control (MAC) and Physical Layer (PHY) Specifications," *IEEE Std 802.11-2012 (Revision of IEEE Std 802.11-2007)*, pp. 1-2793, 2012.

[49] "IEEE Standard for Telecommunications and Information Exchange Between Systems - LAN/MAN Specific Requirements - Part 11: Wireless Medium Access Control (MAC) and physical layer (PHY) specifications: High Speed Physical Layer in the 5 GHz band," *IEEE Std 802.11a-1999*, pp. 1-102, 1999.

[50] "IEEE Standard for Local and metropolitan area networks--Part 15.4: Low-Rate Wireless Personal Area Networks (LR-WPANs)," *IEEE Std 802.15.4-2011 (Revision of IEEE Std 802.15.4-2006)*, pp. 1-314, 2011.

[51] *ZigBee Alliance*. Available: www.zigbee.org (Last accessed: January 2016)

[52] W. Yuan, X. Wang, J.-P. G. Linnartz, and I. M. M. Niemegeers, "Coexistence Performance of IEEE 802.15.4 Wireless Sensor Networks Under IEEE 802.11b/g Interference," *Wireless Personal Communications*, vol. 68, pp. 281-302, 2013/01/01 2013.

[53] G. Wenqi, W. M. Healy, and Z. MengChu, "Impacts of 2.4-GHz ISM Band Interference on IEEE 802.15.4 Wireless Sensor Network Reliability in Buildings," *Instrumentation and Measurement, IEEE Transactions on*, vol. 61, pp. 2533-2544, 2012.

[54] E. Sarra, H. Moungla, S. Benayoune, and A. Mehaoua, "Coexistence improvement of wearable body area network (WBAN) in medical environment," in *Communications (ICC), 2014 IEEE International Conference on*, 2014, pp. 5694-5699.

[55] Y. Kim, S. Lee, and S. Lee, "Coexistence of ZigBee-Based WBAN and WiFi for Health Telemonitoring Systems," *Biomedical and Health Informatics, IEEE Journal of*, vol. 20, pp. 222-230, 2016.

[56] "IEEE Standard for Local and metropolitan area networks - Part 15.6: Wireless Body Area Networks," *IEEE Std 802.15.6-2012*, pp. 1-271, 2012.

[57] Z. Ya-Li, D. Xiao-Rong, C. C. Y. Poon, B. P. L. Lo, Z. Heye, Z. Xiao-Lin, *et al.*, "Unobtrusive Sensing and Wearable Devices for Health Informatics," *Biomedical*

Engineering, IEEE Transactions on, vol. 61, pp. 1538-1554, 2014.

[58] M. Klemm, I. Z. Kovcs, G. F. Pedersen, and G. Troster, "Novel small-size directional antenna for UWB WBAN/WPAN applications," *Antennas and Propagation, IEEE Transactions on,* vol. 53, pp. 3884-3896, 2005.

[59] G. Quintero, J. F. Zurcher, and A. K. Skrivervik, "System Fidelity Factor: A New Method for Comparing UWB Antennas," *Antennas and Propagation, IEEE Transactions on,* vol. 59, pp. 2502-2512, 2011.

[60] K. Do-Hoon, "Effect of antenna gain and group delay variations on pulse-preserving capabilities of ultrawideband antennas," *Antennas and Propagation, IEEE Transactions on,* vol. 54, pp. 2208-2215, 2006.

[61] M. J. Kuhn, Z. Cemin, L. Song, M. R. Mahfouz, and A. E. Fathy, "A system level design approach to UWB localization," in *Microwave Symposium Digest, 2009. MTT '09. IEEE MTT-S International*, 2009, pp. 1409-1412.

[62] G. A. Conway, W. G. Scanlon, C. Orlenius, and C. Walker, "In Situ Measurement of UHF Wearable Antenna Radiation Efficiency Using a Reverberation Chamber," *Antennas and Wireless Propagation Letters, IEEE,* vol. 7, pp. 271-274, 2008.

[63] T. Alves, B. Poussot, and J. M. Laheurte, "PIFA-Top-Loaded-Monopole Antenna With Diversity Features for WBAN Applications," *Antennas and Wireless Propagation Letters, IEEE,* vol. 10, pp. 693-696, 2011.

[64] P. J. Soh, G. A. E. Vandenbosch, O. Soo Liam, and N. H. M. Rais, "Design of a Broadband All-Textile Slotted PIFA," *Antennas and Propagation, IEEE Transactions on,* vol. 60, pp. 379-384, 2012.

[65] T. Tuovinen, M. Berg, K. Y. Yazdandoost, and J. Iinatti, "Ultra wideband loop antenna on contact with human body tissues," *Microwaves, Antennas & Propagation, IET,* vol. 7, pp. 588-596, 2013.

[66] Z. Shiyu, R. Seager, A. Chauraya, W. Whittow, and Y. Vardaxoglou, "Textile manufacturing techniques in RF devices," in *Antennas and Propagation Conference (LAPC), 2014 Loughborough*, 2014, pp. 182-186.

[67] N. P. I. Kammersgaard, S. H. Kvist, J. Thaysen, and K. B. Jakobsen, "In-the-ear spiral monopole antenna for hearing instruments," *Electronics Letters,* vol. 50, pp. 1509-1511, 2014.

[68] R. Chandra and A. J. Johansson, "Antennas and Propagation for In-Mouth Tongue-Controlled Devices in Wireless Body Area Networks," *Antennas and*

Wireless Propagation Letters, IEEE, vol. 14, pp. 1518-1521, 2015.

[69] D. Gaetano, P. McEvoy, M. J. Ammann, M. John, C. Brannigan, L. Keating, *et al.*, "Insole Antenna for On-Body Telemetry," *Antennas and Propagation, IEEE Transactions on,* vol. 63, pp. 3354-3361, 2015.

[70] A. Hassanien and S. A. Vorobyov, "Transmit Energy Focusing for DOA Estimation in MIMO Radar With Colocated Antennas," *Signal Processing, IEEE Transactions on,* vol. 59, pp. 2669-2682, 2011.

[71] A. Moreira, P. Prats-Iraola, M. Younis, G. Krieger, I. Hajnsek, and K. P. Papathanassiou, "A tutorial on synthetic aperture radar," *Geoscience and Remote Sensing Magazine, IEEE,* vol. 1, pp. 6-43, 2013.

[72] F. Rodriguez-Morales, S. Gogineni, C. J. Leuschen, J. D. Paden, L. Jilu, C. C. Lewis, *et al.*, "Advanced Multifrequency Radar Instrumentation for Polar Research," *Geoscience and Remote Sensing, IEEE Transactions on,* vol. 52, pp. 2824-2842, 2014.

[73] O. Malyuskin and V. F. Fusco, "High-Resolution Microwave Near-Field Surface Imaging Using Resonance Probes," *Instrumentation and Measurement, IEEE Transactions on,* vol. 65, pp. 189-200, 2016.

[74] K. B. Cooper, R. J. Dengler, N. Llombart, B. Thomas, G. Chattopadhyay, and P. H. Siegel, "THz Imaging Radar for Standoff Personnel Screening," *Terahertz Science and Technology, IEEE Transactions on,* vol. 1, pp. 169-182, 2011.

[75] S. Lambot and F. Andre, "Full-Wave Modeling of Near-Field Radar Data for Planar Layered Media Reconstruction," *Geoscience and Remote Sensing, IEEE Transactions on,* vol. 52, pp. 2295-2303, 2014.

[76] J. Wilson and N. Patwari, "Radio Tomographic Imaging with Wireless Networks," *Mobile Computing, IEEE Transactions on,* vol. 9, pp. 621-632, 2010.

[77] N. Patwari and J. Wilson, "RF Sensor Networks for Device-Free Localization: Measurements, Models, and Algorithms," *Proceedings of the IEEE,* vol. 98, pp. 1961-1973, 2010.

[78] J. Wilson and N. Patwari, "See-Through Walls: Motion Tracking Using Variance-Based Radio Tomography Networks," *Mobile Computing, IEEE Transactions on,* vol. 10, pp. 612-621, 2011.

[79] N. Patwari, J. Wilson, S. Ananthanarayanan, S. K. Kasera, and D. R. Westenskow, "Monitoring Breathing via Signal Strength in Wireless Networks," *Mobile Computing, IEEE Transactions on,* vol. 13, pp. 1774-1786, 2014.

[80] K. Woyach, D. Puccinelli, and M. Haenggi, "Sensorless Sensing in Wireless Networks: Implementation and Measurements," in *Modeling and Optimization in Mobile, Ad Hoc and Wireless Networks, 2006 4th International Symposium on*, 2006, pp. 1-8.

[81] M. B. Cover, K. S. Kanukurthy, and D. R. Andersen, "Microwave tomography using dynamic 802.15.4 wireless networks," in *Electro/Information Technology, 2007 IEEE International Conference on*, 2007, pp. 251-256.

[82] M. Xufei, T. Shaojie, and L. Xiang-Yang, "Multiple Objects Device-Free Passive Tracking Using Wireless Sensor Networks," in *Communications (ICC), 2011 IEEE International Conference on*, 2011, pp. 1-5.

[83] M. Seifeldin, A. Saeed, A. E. Kosba, A. El-Keyi, and M. Youssef, "Nuzzer: A Large-Scale Device-Free Passive Localization System for Wireless Environments," *Mobile Computing, IEEE Transactions on*, vol. 12, pp. 1321-1334, 2013.

[84] R. C. Qiu, M. C. Wicks, L. Li, Z. Hu, S. J. Hou, P. Chen, *et al.*, "Wireless tomography, Part I: A novel approach to remote sensing," in *Waveform Diversity and Design Conference (WDD), 2010 International*, 2010, pp. 000244-000256.

[85] R. C. Qiu, Z. Hu, M. C. Wicks, S. J. Hou, L. Li, and J. L. Gary, "Wireless tomography, Part II: A system engineering approach," in *Waveform Diversity and Design Conference (WDD), 2010 International*, 2010, pp. 277-282.

[86] Z. Peng and R. C. Qiu, "Wireless tomography, Part III: Compressed sensing for ultra-wideband signals," in *Waveform Diversity and Design Conference (WDD), 2010 International*, 2010, pp. 35-39.

[87] V. Rampa, F. Vicentini, S. Savazzi, N. Pedrocchi, M. Ioppolo, and M. Giussani, "Safe human-robot cooperation through sensor-less radio localization," in *Industrial Informatics (INDIN), 2014 12th IEEE International Conference on*, 2014, pp. 683-689.

[88] P. Qifan, G. Sidhant, G. Shyamnath, and P. Shwetak, "Whole-home gesture recognition using wireless signals," presented at the Proceedings of the 19th annual international conference on Mobile computing and networking, Miami, Florida, USA, 2013.

[89] *Microsoft Inc. Kinect for Xbox One*. Available: http://www.xbox.com/en-GB/xbox-one/accessories/kinect-for-xbox-one#fbid=ZOcL-NlxldP (Last accessed January 2016)

[90] *Whole-Home Gesture Recognition Using Wireless, Computer Science & Engineering, University of Washington*. Available: http://wisee.cs.washington.edu (Last accessed: January 2016)

[91] G. Cohn, D. Morris, S. Petal, and D. Tan. *Humantenna: Sensing Gestures Using the Body as an Antenna*. Available: http://research.microsoft.com/en-us/um/redmond/groups/cue/humantenna/ (Last accessed: January 2016)

[92] Y.-J. An, B.-J. Jang, and J.-G. Yook, "Detection of human vital signs and estimation of direction of arrival using multiple doppler radars," *Journal of Electromagnetic Engineering And Science*, vol. 10, pp. 250-255, 2010.

[93] D. Obeid, S. Sadek, G. Zaharia, and G. E. Zein, "Doppler radar for heartbeat rate and heart rate variability extraction," in *E-Health and Bioengineering Conference (EHB), 2011*, 2011, pp. 1-4.

[94] Y. J. An, G. H. Yun, and J. G. Yook, "Sensitivity Enhanced Vital Sign Detection Based on Antenna Reflection Coefficient Variation," *Biomedical Circuits and Systems, IEEE Transactions on*, vol. PP, pp. 1-1, 2015.

[95] A. A. Serra, P. Nepa, G. Manara, G. Corsini, and J. L. Volakis, "A Single On-Body Antenna as a Sensor for Cardiopulmonary Monitoring," *Antennas and Wireless Propagation Letters, IEEE*, vol. 9, pp. 930-933, 2010.

[96] R. Bhattacharyya, C. Floerkemeier, and S. Sarma, "Low-Cost, Ubiquitous RFID-Tag-Antenna-Based Sensing," *Proceedings of the IEEE*, vol. 98, pp. 1593-1600, 2010.

[97] C. Tsirmpas, A. Rompas, O. Fokou, and D. Koutsouris, "An indoor navigation system for visually impaired and elderly people based on Radio Frequency Identification (RFID)," *Information Sciences*, vol. 320, pp. 288-305, 11/1/ 2015.

[98] A. R. J. Ruiz, F. S. Granja, J. C. Prieto Honorato, and J. I. G. Rosas, "Accurate Pedestrian Indoor Navigation by Tightly Coupling Foot-Mounted IMU and RFID Measurements," *Instrumentation and Measurement, IEEE Transactions on*, vol. 61, pp. 178-189, 2012.

[99] I. Mohammad and H. Huang, "Monitoring fatigue crack growth and opening using antenna sensors," *Smart Materials and Structures*, vol. 19, p. 055023, 2010.

[100] C. Occhiuzzi, C. Paggi, and G. Marrocco, "Passive RFID Strain-Sensor Based on Meander-Line Antennas," *Antennas and Propagation, IEEE Transactions on*, vol. 59, pp. 4836-4840, 2011.

[101] M. J. Cazeca, J. Mead, J. Chen, and R. Nagarajan, "Passive wireless displacement

sensor based on RFID technology," *Sensors and Actuators A: Physical*, vol. 190, pp. 197-202, 2/1/ 2013.

[102] *Project Soli, Google Inc.* Available: www.google.com/atap/project-soli (Last accessed: January 2016)

[103] A. Yong-Jun, Y. Gi-Ho, K. Sung Woo, and Y. Jong-Gwan, "Wrist Pulse Detection System Based on Changes in the Near-Field Reflection Coefficient of a Resonator," *Microwave and Wireless Components Letters, IEEE*, vol. 24, pp. 719-721, 2014.

[104] B. Pottier and L. Rasolofondraibe, "Capacitive Sensor Dedicated to Pedestrians Protection," *Sensors Journal, IEEE*, vol. 15, pp. 5886-5892, 2015.

[105] *CST Microwave Studio, CST Computer Simulation Technology AG.* Available: www.cst.com/Products/CSTMWS (Last accessed: January 2016)

[106] J. Shlens. *A Tutorial on Principal Component Analysis: Derivation, Discussion and Singular Value Decomposition (2003).* Available: https://www.cs.princeton.edu/picasso/mats/PCA-Tutorial-Intuition_jp.pdf (Last accessed: January 2016)

[107] I. T. Jolliffe, *Principal Component Analysis*: Springer, 2002.

[108] M. Linting, "Nonparametric inference in nonlinear principal components analysis: exploration and beyond," Data Theory Group, Department of Education, Faculty of Social and Behavioural Sciences, Leiden University, 2007.

[109] A. Buja and N. Eyuboglu, "Remarks on Parallel Analysis," *Multivariate Behavioral Research*, vol. 27, p. 509, 1992.

[110] J. J. Martinez, M. A. Campbell, M. S. Warden, E. B. Hughes, N. J. Copner, and A. J. Lewis, "Dual-Sweep Frequency Scanning Interferometry Using Four Wave Mixing," *Photonics Technology Letters, IEEE*, vol. 27, pp. 733-736, 2015.

[111] A. Anghel, G. Vasile, R. Cacoveanu, C. Ioana, and S. Ciochina, "Short-Range Wideband FMCW Radar for Millimetric Displacement Measurements," *Geoscience and Remote Sensing, IEEE Transactions on*, vol. 52, pp. 5633-5642, 2014.

[112] M. Elhoushi, J. Georgy, A. Noureldin, and M. J. Korenberg, "Motion Mode Recognition for Indoor Pedestrian Navigation Using Portable Devices," *Instrumentation and Measurement, IEEE Transactions on*, vol. 65, pp. 208-221, 2016.

[113] Y. Jun, "Toward physical activity diary: motion recognition using simple

acceleration features with mobile phones," presented at the Proceedings of the 1st international workshop on Interactive multimedia for consumer electronics, Beijing, China, 2009.

[114] R. Cavallari, F. Martelli, R. Rosini, C. Buratti, and R. Verdone, "A Survey on Wireless Body Area Networks: Technologies and Design Challenges," *IEEE Comm. Surveys & Tutorials, ,* vol. 16, pp. 1635-1657, 2014.

[115] Y.-f. Wei and C. Roblin, "Multislot Antenna with a Screening Backplane for UWB WBAN Applications," *International Journal of Antennas and Propagation,* vol. 2012, p. 12, 2012.

[116] T. Castel, P. Van Torre, E. Tanghe, S. Agneessens, G. Vermeeren, xfc, *et al.*, "Improved Reception of In-Body Signals by Means of a Wearable Multi-Antenna System," *International Journal of Antennas and Propagation,* vol. 2013, p. 9, 2013.

[117] W. Amer, G. Y. Tian, and C. Tsimenidis, "Sensing passive object existence within an antenna near field based on return loss," in *Antennas and Propagation Conference (LAPC), 2014 Loughborough*, 2014, pp. 400-404.

[118] S. Wen-Tron, J. Shiou-Chiau, and T. Jenn-Hwan, "A Reduced-Size Wide Slot Antenna for Enhancing Along-Body Radio Propagation in UWB On-Body Communications," *IEEE Trans. Antennas and Propag.,* vol. 62, pp. 1194-1203, 2014.

[119] P. J. Gibson, "The Vivaldi Aerial," in *Microwave Conference, 1979. 9th European*, 1979, pp. 101-105.

[120] W. Sung-Jung and M. Tzyh-Ghuang, "A Wideband Slotted Bow-Tie Antenna With Reconfigurable CPW-to-Slotline Transition for Pattern Diversity," *Antennas and Propagation, IEEE Transactions on,* vol. 56, pp. 327-334, 2008.

[121] W. Ya-Wei, W. Guang-Ming, and Z. Bin-Feng, "Directivity Improvement of Vivaldi Antenna Using Double-Slot Structure," *Antennas and Wireless Propagation Letters, IEEE,* vol. 12, pp. 1380-1383, 2013.

[122] K. Ebnabbasi, D. Busuioc, R. Birken, and W. Ming, "Taper Design of Vivaldi and Co-Planar Tapered Slot Antenna (TSA) by Chebyshev Transformer," *Antennas and Propagation, IEEE Transactions on,* vol. 60, pp. 2252-2259, 2012.

[123] B. Jian, S. Shouyuan, and D. W. Prather, "Modified Compact Antipodal Vivaldi Antenna for 4-50-GHz UWB Application," *IEEE Trans. Microwave Theory and Techniques,* vol. 59, pp. 1051-1057, 2011.

[124] F. Peng, J. Yong-Chang, H. Wei, and Z. Fu-Shun, "A Miniaturized Antipodal Vivaldi Antenna With Improved Radiation Characteristics," *IEEE Trans. Antennas and Propag.*, vol. 10, pp. 127-130, 2011.

[125] W. Jiangniu, Z. Zhiqin, N. Zaiping, and L. Qing-Huo, "A Printed UWB Vivaldi Antenna Using Stepped Connection Structure Between Slotline and Tapered Patches," *IEEE Antennas Wireless Propag. Lett.*, vol. 13, pp. 698-701, 2014.

[126] W. Qiong, R. Hahnel, Z. Hui, and D. Plettemeier, "On-body directional antenna design for in-body UWB wireless communication," in *Antennas and Propagation (EUCAP), 2012 6th European Conference on*, 2012, pp. 1011-1015.

[127] W. Amer, T. Gui Yun, and C. Tsimenidis, "A novel, low-profile, directional UWB antenna for WBAN," in *Antennas and Propagation Conference (LAPC), 2014 Loughborough*, 2014, pp. 708-710.

[128] H. G. Schantz, *The Art and Science of Ultra-Wideband Antennas*, 1St Edition ed.: Artech House Print on Demand, 2005.

[129] A. G. Yarovoy, R. Pugliese, J. H. Zijderveld, and L. P. Ligthart, "Antenna development for UWB impulse radio," in *Microwave Conference, 2004. 34th European*, 2004, pp. 1257-1260.

[130] W. S. T. Rowe and R. B. Waterhouse, "Reduction of backward radiation for CPW fed aperture stacked patch antennas on small ground planes," *Antennas and Propagation, IEEE Transactions on*, vol. 51, pp. 1411-1413, 2003.

[131] S. D. Targonski, D. M. Pozar, and R. B. Waterhouse, "Aperture-coupled microstrip antennas using reflector elements for wireless communications," in *Antennas and Propagation for Wireless Communications, 1998. 1998 IEEE-APS Conference on*, 1998, pp. 163-166.

[132] W. Wiesbeck, G. Adamiuk, and C. Sturm, "Basic Properties and Design Principles of UWB Antennas," *Proceedings of the IEEE*, vol. 97, pp. 372-385, 2009.

[133] C. M. Kruesi, R. J. Vyas, and M. M. Tentzeris, "Design and Development of a Novel 3-D Cubic Antenna for Wireless Sensor Networks (WSNs) and RFID Applications," *IEEE Trans. Antennas and Propag.*, vol. 57, pp. 3293-3299, 2009.

[134] M. M. Khan, Q. H. Abbasi, A. Alomainy, H. Yang, and C. Parini, "Experimental characterisation of ultra-wideband off-body radio channels considering antenna effects," *Microwaves, Antennas & Propagation, IET*, vol. 7, pp. 370-380, 2013.

[135] D. B. Smith, D. Miniutti, T. A. Lamahewa, and L. W. Hanlen, "Propagation Models for Body-Area Networks: A Survey and New Outlook," *Antennas and*

Propagation Magazine, IEEE, vol. 55, pp. 97-117, 2013.

[136] S. L. Cotton, "A Statistical Model for Shadowed Body-Centric Communications Channels: Theory and Validation," *Antennas and Propagation, IEEE Transactions on,* vol. 62, pp. 1416-1424, 2014.

[137] R. Di Bari, Q. H. Abbasi, A. Alomainy, and Y. Hao, "An advanced UWB channel model for body-centric wireless networks," *progress in electromagnetics research,* vol. 136, pp. 79-99, 2013.

[138] R. G. Garcia-Serna, C. Garcia-Pardo, and J. M. Molina-Garcia-Pardo, "Effect of the Receiver Attachment Position on Ultrawideband Off-Body Channels," *Antennas and Wireless Propagation Letters, IEEE,* vol. 14, pp. 1101-1104, 2015.

[139] N. Yamamoto, N. Shirakata, D. Kobayashi, K. Honda, and K. Ogawa, "BAN Radio Link Characterization Using an Arm-Swinging Dynamic Phantom Replicating Human Walking Motion," *Antennas and Propagation, IEEE Transactions on,* vol. 61, pp. 4315-4326, 2013.

[140] Q. H. Abbasi, A. Sani, A. Alomainy, and H. Yang, "Experimental Characterization and Statistical Analysis of the Pseudo-Dynamic Ultrawideband On-Body Radio Channel," *Antennas and Wireless Propagation Letters, IEEE,* vol. 10, pp. 748-751, 2011.

[141] S. Manzari, C. Occhiuzzi, and G. Marrocco, "Feasibility of Body-Centric Systems Using Passive Textile RFID Tags," *Antennas and Propagation Magazine, IEEE,* vol. 54, pp. 49-62, 2012.

[142] P. A. Catherwood and W. G. Scanlon, "Body-centric ultra-wideband multi-channel characterisation and spatial diversity in the indoor environment," *Microwaves, Antennas & Propagation, IET,* vol. 7, pp. 61-70, 2013.

[143] M. Bosiljevac, Z. Sipus, and A. K. Skrivervik, "Propagation in Finite Lossy Media: An Application to WBAN," *Antennas and Wireless Propagation Letters, IEEE,* vol. 14, pp. 1546-1549, 2015.

[144] R. Moro, S. Agneessens, H. Rogier, A. Dierck, and M. Bozzi, "Textile Microwave Components in Substrate Integrated Waveguide Technology," *Microwave Theory and Techniques, IEEE Transactions on,* vol. 63, pp. 422-432, 2015.

[145] Z. Wang, J. L. Volakis, and A. Kiourti, "10 - Embroidered antennas for communication systems A2 - Dias, Tilak," in *Electronic Textiles*, ed Oxford: Woodhead Publishing, 2015, pp. 201-237.

[146] A. Farswan, A. K. Gautam, B. K. Kanaujia, and K. Rambabu, "Design of Koch

Fractal Circularly Polarized Antenna for Handheld UHF RFID Reader Applications," *Antennas and Propagation, IEEE Transactions on,* vol. 64, pp. 771-775, 2016.

[147] H. Orazi and H. Soleimani, "Miniaturisation of the triangular patch antenna by the novel dual-reverse-arrow fractal," *Microwaves, Antennas & Propagation, IET,* vol. 9, pp. 627-633, 2015.

[148] A. T. Mobashsher and A. M. Abbosh, "Near-field time-domain characterisation of wideband antennas," *Electronics Letters,* vol. 51, pp. 2076-2078, 2015.

APPENDIX A: PRINCIPAL COMPONENT ANALYSIS

This appendix present background of PCA method and how to calculate its statistical significance. Section A.1 shows the step by step calculations of the PCA results presented earlier in this thesis, while Section A.2 lists MATLAB code used for PCA calculation. Finally, Section A.3 lists MATLAB code for the permutation test used in the statistical significance study.

A.1 Data Preparation and Classification Algorithm

PCA is a multivariate statistical analysis method which transforms the magnitude and phase responses of the S-parameters into uncorrelated eigenvectors or principal components (PCs) corresponding to the maxi-mum variability within the data. The PCs are weighted sums of the original variables. The first PC accounts for the largest variation in the data. Subsequent PCs correspond to the remaining variability. PCA was used in this work to extract the most dominant trends in data and link these trends to the effects of nearby object at several locations around the antenna. The principal components was calculated using the following procedure [106, 107]:

1. Prepare the data:

The input data should be arranged in m×n matrix, where m is the number of observations and n is the number of variables. For example, in the first approach discussed in Section 3.4, the variables for each observation was formed as follow:

$$A_i = |S_{11}| \ ,$$
$$B_i = \angle S_{11} \ ,$$
$$C_i = |S_{12}| \ , \text{and}$$
$$D_i = \angle S_{12} \qquad \ldots(A.1)$$

where each one of these vectors contain 1×201elements, and

$$X_i = [A_i \ B_i \ C_i \ D_i] \qquad \ldots (A.2)$$

is 1×804 vector that represent the variables of the i^{th} observation .

Each observation correspond to results from one test. The test was repeated for three different location of the metallic object around the antenna, with 25 distance steps at each location, hence there are 75 observations. Four more tests were conducted without the presence of the metallic object. Therefore, the final data set X consist of 79×804 elements and calculated as follow:

$$X = \begin{bmatrix} X_1 \\ X_2 \\ \vdots \\ X_{79} \end{bmatrix} \quad \ldots \text{(A.3)}$$

2. Subtract off the mean variable-wise (row-wise):
3. Calculate the covariance matrix:

$$Cov_X = \begin{pmatrix} var(X_1) & cov(X_1, X_2) & \cdots & cov(X_1, X_{79}) \\ cov(X_2, X_1) & cov(X_2, X_2) & \cdots & cov(X_2, X_{79}) \\ \vdots & \vdots & \ddots & \vdots \\ cov(X_{79}, X_1) & cov(X_{79}, X_2) & \cdots & var(X_{79}) \end{pmatrix} \quad \ldots \text{(A.4)}$$

4. Find the eigenvectors E_X and eigenvalues from the symmetric matrix $X^T X$
5. Sort the eigenvectors matrix in decreasing order according to the Eigenvalues diagonal matrix.
6. Generate PCA component space (PCA scores) by multiplying eigenvectors matrix with the mean subtracted X:

$$PCA = E_X\, X \quad \ldots \text{(A.5)}$$

7. Since the PCA matrix is sorted in descending order, only the first component PC1 and PC2 were considered in the results discussion.
8. In the second approach of Section 3.4, the input data set was formed as follow:

$$X = \begin{bmatrix} X_1 \\ X_2 \\ \vdots \\ X_{79} \end{bmatrix} \quad \ldots \text{(A.6)}$$

where each observation X_i is 1×5 vector set that represent five features extracted from the i^{th} observation as follow:

$$X_i = [\,F1_i \;\; F2_i \;\; F3_i \;\; F4_i \;\; F5_i] \quad \ldots (A.7)$$

And the covariance matrix is calculated as follow:

$$Cov_X = \begin{pmatrix} var(X_1) & cov(X_1,X_2) & \cdots & cov(X_1,X_5) \\ cov(X_2,X_1) & cov(X_2,X_2) & \cdots & cov(X_2,X_5) \\ \vdots & \vdots & \ddots & \vdots \\ cov(X_5,X_1) & cov(X_5,X_2) & \cdots & var(X_5) \end{pmatrix} \quad \ldots (A.8)$$

A.2 MATLAB Code for PCA Calculation

```
%Prepare the data
data=[s11mag  s11phase  s12mag  s12phase];
[M,N] = size(data);

% subtract off the mean for each dimension
mn = mean(data,2);
data = data - repmat(mn,1,N);

% calculate the covariance matrix
covariance = 1 / (N-1) * data * data';

% find the eigenvectors and eigenvalues
[PC, V] = eig(covariance);

% extract diagonal of matrix as vector
V = diag(V);

% sort the variances in decreasing order
[junk, rindices] = sort(-1*V);
V = V(rindices);
PC = PC(:,rindices);

% project the original data set
signals = PC' * data;
```

A.3 MATLAB Code for Permutation Test

```
function [pvalue] = PermutationTest(data,groups,permutations,alpha)
control = ~isempty(data);
assert(control,'The user must introduce a matrix with the data (first
inpunt).');
control = ~isempty(groups);
assert(control,'The user must introduce a vetor for grouping the data
(second inpunt).');
control = ~isempty(permutations);
assert(control,'The user must indicate the number of permutations that
they want (third inpunt).');

pvalue = [];
if (nargin == 3)
    alpha = 0.05;
end

control = ~((1/permutations) > alpha);
assert(control,'The number of permutations is not valid for the
selected significance threshold.');

n = hist(groups); n = n(logical(n)); den = 1;
for i = 1:length(n)
    den = den*factorial(n(i));
end
max_permutations = factorial(sum(n))/den;
control = ~(permutations > max_permutations);
assert(control,'The number of permutations exceeds the maximum
possible value.'),

control = ~(size(data,1) ~= length(groups));
assert(control,'The number of observations differs from grouping
elements.'),

indexes_permuted = (1:size(data,1))';
num_indexes_permuted = size(indexes_permuted,2); % Initialization to 1
while (num_indexes_permuted < permutations)
    index = randperm(length(groups))';
    if ~any(all(indexes_permuted ==
repmat(index,1,size(indexes_permuted,2))))
        indexes_permuted = [indexes_permuted,index];
        num_indexes_permuted = num_indexes_permuted + 1;
    end
end

maximal_distribution = zeros(1,permutations);
for i = 1:permutations
    data_permuted = data(indexes_permuted(:,i),:);
    statistic = zeros(1,size(data,2));
    for sensor = 1:size(data,2)
        [p,table,~] = anova1(data_permuted(:,sensor),groups,'off');
        statistic(1,sensor) = table{2,5};
    end
    maximal_distribution(1,i) = max(statistic);
end
maximal_distribution = sort(maximal_distribution);
for sensor = 1:size(data,2)
    [p,table,~] = anova1(data(:,sensor), groups,'off');
    statistic = table{2,5};
```

```
    c = min(find(maximal_distribution > statistic));
    pvalue(sensor) = (permutations-c)/permutations;
end

end
```